UNIVERSIDADE DE
SANTIAGO DE COMPOSTELA

Departamento De Física Aplicada

Area de Óptica

Integer and Fractional Talbot Effect: Theoretical Study and Practical Considerations

Laura Chantada Santodomingo
Santiago de Compostela, Junio 2006

D. Carlos Gómez-Reino Carnota y D. Carlos Rodríguez Fernández-Pousa, Catedrático del Área de Óptica del Departamento de Física Aplicada de la Universidad de Santiago de Compostela y Contratado Doctor del Área de Teoría de la Señal y Comunicaciones del Departamento de Física y Arquitectura de Computadores de la Universidad Miguel Hernández de Elche,

CERTIFICAN

que la presente memoria, titulada *"Integer and Fractional Temporal Talbot Effect: Theoretical Study and Practical Considerations"* ha sido realizada por **Dña. Laura Chantada Santodomingo** bajo su dirección y constituye la Tesis que presenta para optar al Grado de Doctor en Ciencias Físicas.

Santiago de Compostela, 8 de Junio de 2006.

V°. B°. Director de la tesis

Carlos Gómez-Reino Carnota

V°. B°. Director de la tesis

Carlos Rodríguez Fernández-Pousa

La doctoranda

Laura Chantada Santodomingo

Este trabajo ha sido financiado por los proyectos TIC99-0489 y
TIC2003-03041 del ministerio de Educacíon y Ciencia y el proyecto
PGIDT04PXIC20605PN de la Xunta de Galicia
Gracias al ministerio de Educación y Ciencia por la ayuda económica
recibida a través de la beca FPU.

Resumen

Las técnicas y dispositivos que permiten la manipulación de las propiedades de las ondas guiadas, constituyen la base tecnológica de la espectroscopía de señales moduladas, del procesado fotónico, y de los métodos para el análisis temporal de fuentes pulsadas. Para implementar todas estas técnicas se pueden utilizar tanto procesos lineales como no lineales. Dentro del contexto de la óptica lineal, la llamada analogía espacio-temporal se ha convertido en los últimos años en la una guía muy fructífera para el diseño de nuevos dispositivos. La dualidad espacio-temporal permite trasladar conceptos e ideas bien conocidas en procesado de señales espaciales al dominio temporal, proporcionando de este modo nuevas formas para el procesado, manipulación y control de señales temporales. Dicha analogía está basada en la equivalencia matemática entre la ecuación que describe la difracción paraxial de haces y la ecuación de dispersión de primer orden que gobierna la evolución de pulsos ópticos cuando éstos se propagan en un medio dieléctrico o en una guía de onda. En ambos casos se trata de una ecuación diferencial parabólica con coeficientes imaginarios, y por tanto admite soluciones ondulatorias. Las ecuaciones que describen la evolución de envolventes ópticas lentamente variables, correspondientes a ondas planas o modos (en el caso de guías de onda) modulados temporalmente, son formalmente idénticas a las ecuaciones paraxiales que describen la propagación de ondas monocromáticas de extensión finita. Existe por tanto una correspondencia entre la variable temporal de los problemas dispersivos y la variable espacial transversal de los problemas difractivos. Asimismo, en el dominio de Fourier esta correspondencia se da entre los espectros de ambos problemas. Esta dualidad representa el marco conceptual de la compresión lineal de pulsos, así como de muchos otros dispositivos que han sido propuestos en los últimos años. Entre ellos podemos mencionar, sistemas de formación de imagenes temporales, filtrado temporal por medio de lentes temporales, redución de *jitter*, la transformada de Fourier temporal, la versión temporal del teorema de Van Cittert-Zernike, lentes

temporales de gradiente de índice, técnicas de trasformación tiempo-frecuencia y frecuencia-tiempo y el efecto Talbot temporal entre otros.

El efecto Talbot fue descubierto en 1836 por H.F. Talbot, cuando iluminaba una red de difracción rectangular de agujeros minúsculos con una fuente de luz blanca de pequeño tamaño. A ciertas distancias a lo largo de la dirección de propagación, podían observarse réplicas de las estructuras periódicas que había iluminado. Este efecto no fue satisfactoriamente explicado hasta que Lord Rayleigh, en 1881, lo atribuyó a la interferencia entre haces difractados por las estructuras periódicas. Mostró que, en el caso de una red lineal iluminada con un frente de onda plano, las imágenes de la red se repetían a lo largo de la dirección de iluminación, localizadas a distancias $z_\gamma = \gamma d^2/\lambda$, donde γ es un número entero, d el período de la red y λ la longitud de onda de la fuente. Sin embargo hubo que esperar largos años hasta que Cowley y Moodie (1957-1960), en sus estudios pioneros sobre las propiedades de la difracción de Fresnel de objetos periódicos, dieron una explicación del efecto Talbot en el contexto de la teoría difraccional de la formación de imágenes. Años más tarde, Montgomery (1967) en un trabajo fundamental, desarrolló las condiciones generales que debe satisfacer un objeto para obtener réplicas de su distribución de amplitud compleja a lo largo de la dirección de iluminación. Fue entonces cuando Montgomery introdujo el término autoimagen que a partir de ese momento se usó conjuntamente con el término efecto Talbot en los trabajos que sobre este tema se han publicado hasta la actualidad. Además de la reconstrucción de imagenes, se pueden observar patrones con estructuras mucho más ricas. Por ejemplo, en ciertos planos a lo largo de la direccíon de propagación, se poducen patrones cuya celda unidad está formada por la superposición coherente de las celdas originales desplazadas y con una diferencia de fase entre ellas. De este modo, si las celdas están suficientemente confinadas como para evitar la superposición, se obtienen réplicas del patrón original pero con una periodicidad que es un cierto de número de veces menor que la de la red ilumnada. Este efecto es conocido como efecto Talbot fraccionario.

La contrapartida temporal del efecto de autoimagen o efecto Talbot tiene lugar cuando una señal temporal periódica, como por ejemplo un tren de pulsos ópticos, se propaga a través de un medio dispersivo lineal bajo condiciones de primer orden de dispersión. Cuando la dispersión acumulada es un múltiplo de una cierta escala básica, el tren de pulsos se reproduce a sí mismo tras la propagación, en lo que se conoce como efecto Talbot entero. Por otra parte, cuando la dispersión acumulada es una fracción de dicha

escala básica, a la salida del medio dispersivo se obtiene un tren de pulsos con una frecuencia de repetición que es un número entero de veces la del tren original, siempre y cuando los pulsos sean suficientemente estrechos como para evitar la superposición. Este efecto es conocido como efecto Talbot fracionario. El efecto Talbot temporal entero fue descrito por primera vez por Jannson y Jannson quienes propusieron su uso para la transferencia de información contendia en una señal periódica a lo largo de una fibra óptica. Estos autores establecieron por vez primera las longitudes de la fibra óptica en las que tenía lugar la reconstrucción de la señal periódica. Posteriormente, Andrekson aportó la primera prueba experimental del efecto Talbot, al propagar un tren de pulsos generado por un láser de sincronización de modo (*mode-locking*) a través de una fibra óptica. A finales de los años noventa Shake y Arahira probaron experimentalmente el efecto Talbot fraccionario en fibras momomodo y posteriormente Azaña y Muriel hicieron lo propio en fibras de periodo progresivo (LCFG -*linearly chirped fiber grating*). El efecto Talbot temporal continúa atrayendo el interés de los investigadores, en especial el efecto Talbot fracionario, ya que puede utilizarse para el incremento de la frecuencia de repetición de una secuencia de pulsos periódica como la generada por láseres de sincronización de modo. La generación de trenes de pulsos ópticos con frecuencia de repetición ultrarrápida es de vital importancia en campos como sistemas de computación óptica, porcesado de datos ultrarrápido o sistemas de comunciaciones ópticas entre otras áreas científicas. A pesar de que se ha progresado mucho en la generación directa de trenes de pulsos con altas frecuencias de repetición a partir de láseres de semiconductores o de fibra, resulta ventajoso tener técnicas sencillas que permitan incrementar aún más la frecuencia de repetición fuera de la cavidad del láser. Por otra parte, el efecto Talbot es un fenómeno lineal y por tanto permite su integración con otras técnicas de procesado lineal tales como compresión o reconstrucción (*reshaping*) de pulsos. El efecto Talbot también ha sido usado junto con fenómenos no lineales, así como con sistemas de imagen temporal.

Aunque el análisis experimental de la formación de réplicas Talbot de trenes de pulses se centra típicamente en el dominio temporal, se puede extraer mucha más información mediante el análisis espectral de la intensidad del tren de pulsos. En los filtros convencionales diseñados para aumentar la frecuencia de repetición mediante filtrado óptico, un filtro lineal suprime los armónicos ópticos del tren de entrada que no pertenecen al tren de salida de alta frecuencia. Por lo tanto, el funcionamiento de estos sitemas se puede analizar por medio de la función de transferencia óptica

del filtro lineal. Por el contrario, y debido al hecho de que la dispersión es un filtro de fase puro en el dominio óptico, el análisis espectral de filtros Talbot ha de realizarse en términos de intensidades, lo que da lugar a un análisis espectral no lineal.

En este trabajo se presenta un estudio del efecto Talbot temporal entero y fracionario, teniendo en cuenta consideraciones prácticas tanto a nivel del tren de pulsos como del medio dispersivo utilizado. La memoria consta de tres capítulos. En el primero de ellos, introducimos de forma breve la dualiad espacio temporal que radica en la equivalencia matemática entre las ecuaciones que describen la difración paraxial unidimensional y la propagación de pulsos en un medio dispersivo de primer order con atenuación despreciable. Dentro del contexto de esta analogía presentamos la contrapartida temporal del efecto Talbot. La mayor parte del análisis se realiza en el dominio espectral y se basa en el cálculo exacto de la densidad espectral de potencia de un tren de pulsos coherentes tras su propagación en un medio dispersivo con coeficientes de dispersión de primer y segundo order arbitrarios. Hemos considerado que la señal temporal está formada por un tren de pulsos gaussianos con modulación lineal de fase (*linear chirp*). Estos resultados analíticos permiten identificar las componenetes espectrales que representan la dispersión individual de los pulsos, así como los términos que corresponden la interferencia entre pulsos. Desde el punto de vista espectral las lineas Talbot se pueden interpretar como un filtro pasabanda múltiple, donde cada pasabanda corresponde a la interferencia entre pulsos separados un cierto número de períodos. El filtro elimina los armónicos de intensidad del tren de entrada que no pertenecen a la salida. La supresión de los armónicos sólo es exacta para filtros Talbot semi-enteros, con coeficientes de dispersión de segundo orden y mayores despreciables, y pulsos en el límite de transformada, ya que en este caso las distancias Talbot coinciden con las distancias de supresión de portadora. Los filtros Talbot no son estáticos sino que dependen de la anchura espectral de la señal de entrada y de las caracterísiticas dispersivas de la línea. En particular, hemos deducido las condiciones que garantizan que el filtro Talbot proporciona un tren cuyas fluctuaciones en intensiad son despreciables incluso cuando el medio de propagación presenta coeficiente de dispersión de segundo orden. Finalmente, hemos analizado la estabilidad de las líneas Talbot frente a variaciones de frecuencia o de la longitud de la fibra. Cuando la anchura espectral del tren es grande, la inestabilidad de la dispersión tiende a ensanchar los pulsos empeorando el funcionamento del filtro debido a la interferencia entre pulsos. Por el contrario, cuando

la anchura espectral es moderada, variaciones en la dispersión debilitan la supresión de armónicos. La estabilidad óptima se alcanza cuando la anchura espectral de el tren, medida como FWHM (full width half maximum), es el doble de la frecuencia de repetición del tren de salida.

El objetivo general del segundo capítulo es la descripción espectral de las propiedades de autoregeneración del efecto Talbot temporal. Consideramos que los pulsos tiene forma Gaussiana y están linealmente modulados en fase. Además suponemos que el dispositivo Talbot es ideal, es decir, es un medio dispersivo lineal de primer orden sin atenuación, y con un ancho de banda superior al del tren de pulsos de entrada.

En la primera sección analizamos la densidad de potencia espectral de un tren cuyos pulsos están aleatoriamente distribuidos antes y después de un filtro Talbot. Hemos considerado que las variables que describen la presencia o ausencia de los pulsos en el tren no están correladas. Como consecuencia de la interferencia coherente entre los pulsos dispersados, la envolvente del ruido de banda ancha del espectro de radiofrecuencia después de la detección del tren se ensancha por causa de la modulación de fase de los pulsos. La principal característica del espectro es la presencia de bandas pasantes que filtran el ruido de banda ancha, y cuyos centros aparecen desplazados respecto a los armónicos debido a la modulación de fase. Por tanto, midiendo la desviación relativa de estos centros con respecto a la anchura de las bandas pasantes es posible determinar el signo y la magnitud de la modulación de fase de los pulsos del tren de entrada. Las bandas pasantes son tanto más estrechas cuanto mayor es la dispersión del dispositivo, menor es la anchura temporal de los pulsos y mayor es la modulación de fase. El máximo valor de estas bandas pasantes depende de la cantidad relativa de pulsos presentes en el tren. Para dispositivos de baja dispersión y pulsos anchos las bandas pasantes aparecen moduladas por una función coseno cuadrado. La anchura de esta modulación es una fracción del valor del armónico fundamental de la entrada, y es independiente de la cantidad relativa de pulsos en el tren y de sus propiedades.

En la segunda sección se analiza la influencia del *timing jitter* de un tren de pulsos gaussianos con modulación de fase lineal en un dispositivo Talbot. A pesar de que en nuestro estudio no hemos tenido en cuenta posible fluctuaciones de amplitud (*amplitude jitter*) del tren de pulses, el analisis del *timing jitter* puede generalizarse a problemas con *amplitude jitter* o una combinación de ambos. El análisis se lleva a cabo tanto en el domino temporal como en el espectral. En el análisis temporal consideramos que las variables que describen el *timing jitter* de los pulsos

no están correladas. El estudio presentado muestra como los valores de la varianza del tren se homogeneizan tras su paso por el dispositivo Talbot, ya que tanto los pulsos individuales como su varianza se ensanchan debido a la dispersión, extendiendose por los intevalos temporales de los pulsos vecinos. Presentamos además expresiones analíticas aproximadas para la varianza de la entrada y de la salida, analizando la validez de dichas aproximaciones. Para dispositivos Talbot enteros, el valor de la varianza es constante e independiente del valor de la dispersión. Sin embargo para dispositivos Talbot fraccionarios, la varianza a la salida podría presentar una modulación, dependiendo del cociente entre la anchura temporal del pulso y el período del tren original. En cualquier caso, para los dispositivos Talbot diseñados para aumentar la frecuencia de repetición de un tren de pulsos, la aproximación de la varianza a una constante continúa siendo válida.

El problema del *timing jitter* se analiza también desde el punto de vista espectral. Ahora, y a diferencia del anterior análisis en términos de varianza, consideramos que las variables aleatorias que describen el *jitter* de cada pulso están en general correladas. La principal cararterística del espectro resultante es, como ocurría en el caso de trenes de pulsos aleatoriamente distribuidos, la presencia de un mecanismo de filtrado del ruido de banda ancha, dando lugar a una reducción de la potencia de ruido integrado alrededor de los armónicos en el dominio de radiofrecuencia. También se analiza la influencia de la modulación de fase y de la anchura de línea óptica de los pulsos individuales. Estos resultados se utilizan para analizar la reducción de ruido de las réplicas Talbot bajo diferentes condiciones de propagación. La reducción del ruido causado por el *timing jitter* depende principalmente de la modulación de fase de los pulsos del tren, de la correlación entre pulsos adyacentes y de la dispersión acumulada de la línea, pero sin embargo no depende del valor de la desviación estándar del *timing jitter*. La modulación de fase es la principal causa de deterioro de la reducción de ruido, ya que provoca el desplazamiento de las bandas pasantes con respecto a la posición de los armónicos. Sin embargo, un diseño adecuado de la línea dispersiva permite de un modo sencillo compensar dicha modulación de fase y al mismo tiempo reducir la anchura temporal de los pulsos.

Debido a que la correlación controla el ancho de banda del ruido antes de que el tren de pulsos entre en la línea dispersiva y debido también a que el suavizado del *timing jitter* es más pronunciado a escalas del orden de la frecuencia de repetición, el ruido inicial ha de ser de banda ancha para

que la reducción del *jitter* sea significativa. Este hecho limita la posible aplicación de este método a trenes formados por pulsos cuyas variaciones de periodo están poco correladas. En última instancia, esta aplicación depende del mecanismo de formación de los pulsos. Por ejemplo, la reducción del *jitter* mediante líneas Talbot no se puede aplicar a láseres de sincronización fundamental de modo (*fundamentally mode-locked lasers*) que presenten un ruido offset de hasta 100 MHz. En este caso la cavidad del láser da lugar a pulsos muy correlados. Sin embargo, incluso en esos casos las réplicas Talbot de un láser de sincronización de modo pueden en principio reducir otros tipos de ruido de banda ancha, como por ejemplo el ruido de supermodo en láseres de sincronización armónica de modo (*harmonically mode-locked lasers*).

La reducción del ruido depende de la dispersión acumulada de la línea a través del orden de la réplica Talbot. Básicamente, altos órdenes Talbot implican la aparición de nuevas bandas pasantes entre armónicos y la reducción de la anchura de las mismas. Excepto para el primer armónico, la presencia de nuevas bandas pasantes es un efecto secundario cuando el objetivo es la reducción del ruido. El factor Q que representa el ancho de los pulsos dispersados con respecto a la frecuencia de repetición del tren, controla el estrechamiento de las bandas pasantes. Altos valores de Q implican que los pulsos resultantes de la réplica Talbot están formados por contribuciones de un número elevado de pulsos dispersados, proporcionando así una salida coherentemente mediada.

El capítulo 3 está dedicado a la descripción del efecto Talbot temporal bajo condiciones de cohernecia parcial. Al inicio del capítulo presentamos las fórmulas generales que describen la intensidad promedio de la propagación de una onda guiada modulada parcialmente coherente. Si el medio de propagación es un medio dispersivo de primer orden la intensidad promedio puede expresarse como una convolución. La coherencia parcial de la portadora de la onda modulada se manifiesta, por tanto, como un filtro pasa baja, que actúa sobre la intesidad promedio asociada a una portadora monocromática. Nosotros hemos aplicado este punto de visa a la caracterización del efecto Talbot temporal parcialmente coherente, en cuyo caso la modulación es un tren de pulsos. Este análisis muestra que las limitaciones debidas a la coherencia son más restictivas para dispositivos Talbot de alta dispersión (mayor índice Talbot), ya que es necesario un mayor tiempo de coherencia de la portadora para que se produzca la interferencia ente pulsos. Un aumento de la dispersión, o una disminución del tiempo de coherencia, conlleva la reducción del ancho de banda del filtro

y por tanto, la pérdida de los detalles a baja escala de tiempos, comparado con la intensidad obtenida con una portadora monocromática.

En este capítulo también se presenta un análisis matricial del efecto Talbot temporal bajo condiciones de coherencia parcial. El fenómeno de autoimagen conlleva la discretización del grado complejo de coherencia asociado a las variaciones de amplitud y fase de la onda modulada. El problema matricial que representa la intensidad promedio a distancias Talbot, puede diagonalizarse, lo que da lugar a una interpretación de la intensidad promedio como la suma incoherente de patrones de intensidad. En este contexto presentamos la entropía informacional y el número de fuentes efectivas, como una medida del grado total de coherencia del dispositivo Talbot.

Contents

Introduction

The techniques and devices that permit the manipulation of temporal properties of guided waves constitute the technological basis of photonic signal processing, spectroscopy of modulated waves, and the methods for the temporal analysis of pulsed sources. Both linear and nonlinear effects can help in the implementation of these techniques. In the linear domain the so-called space-time analogy [1–3] has been one of the more fruitful guiding rules in the design of new devices. The space-time duality theory allows the transference of well-known concepts and ideas of spatial signal processing to the temporal domain, thereby providing new ways for processing, manipulating and controlling temporal signals. It is based on the mathematical analogy between the equations that describe the paraxial diffraction of beams in space and the first-order temporal dispersion of optical pulses in a dielectric or waveguide. Both problems are described by parabolic differential equation with imaginary coefficients and therefore admit wave solutions [2]. The slowly varying envelope equations corresponding to modulated plane waves in dispersive media (or modes in the case of waveguides) have the same form that the paraxial equations describing the propagation of monochromatic waves of finite spatial extent [3]. There is a correspondence between the time variable in the dispersion problem and the transverse space variable in the diffraction problem. This also leads to a similar correspondence between the temporal and spatial Fourier spectra of the two problems. This analogy represents the conceptual framework of the well-known linear pulse-compression technique [4, 5], and of many other devices and systems proposed in the last years. We can mention temporal imaging systems [6, 7], temporal filtering using time lenses [8], the temporal Fourier transform [9–11], the temporal van Cittert-Zernike theorem [12], the temporal Collett-Wolf theorem [13, 14], the graded-index time-lens [15], timing jitter reduction systems [16], the frequency-to-time [17] and time-to-frequency [18] techniques and the temporal Talbot effect [19, 20].

The Talbot or self-imaging effect was firstly observed by Talbot in 1836 when he illuminated a diffraction grating and a rectangular array of tiny holes with a very small white light source. Behind the structure he observed colorful intensity patterns resembling the periodic objects themselves. This phenomenon was called Talbot effect [21] and it was not satisfactorily explained until 1881 when Rayleigh attributed its origin to the interference of diffracted beams. However it was necessary to wait for many years until Cowley and Moodie in 1960 explained the problem in terms of diffraction theory of imaging formation. Some years later Montgomery developed in a fundamental work [21], general conditions that need to be satisfied by an object to obtain repetition of its complex amplitude transmittance along the illumination direction. In addition to the reconstruction images, many more interesting patters have been observed. For instance, at other positions along the direction of light propagation, we find patterns whose cells are composed of the coherent superposition of several shifted cells with phase difference among them. These patterns constitute the essence of the so-called fractional Talbot effect [21, 22]. When cells are sufficiently confined to avoid superposition a replica of the grating but with a periodicity lower than that of the original one is achieved.

The temporal counterpart of the Talbot effect appears when a coherent train of pulses is propagated through a dispersive medium under first-order dispersion conditions [20]. The temporal integer self-imaging effect was first described by Jannson and Jannson [19] who proposed to use it for the transference of information contained in periodic signals along an optical fiber. For the first time the authors established the fiber distances where an input periodic signal is exactly replicated. Subsequently, Andrekson [23] showed it experimentally by propagating a train of pulses from a mode-locked laser along a ultra-long fiber transmission system. The author suggested the use of mode-locked lasers owing to the fact that each of the modes that take part in producing the mode-locked pulse is highly coherent. This means that a launched pulse, the different modes of which experience slightly different group velocities as a result of a fiber dispersion, will involve through differently superpositioned intensity profiles periodically as the pulse propagates through a fiber. The distance over which such periodic recreation of a mode-locked pulse can be maintained is essentially limited by the temporal coherence of each of the modes, and this distance can be extremely long. In 1998, Arahira *et al.* [24,25] and Shake *et al.* [26] reported separately on experimental demonstration of the fractional Talbot effect in standard monomode fiber, achieving a sequence of pulse with a repetition

rate of 196 GHz (four times the original one) and 400 GHz (eight times the original one) respectively. Integer and fractional Talbot effect have been also demonstrated in linearly chirped fiber gratings (LCFG) [27, 28] and multimode fibers [29]. The temporal Talbot effect is still attracting the interest of researches [30–33], especially the fractional Talbot effect, due to the fact that it can be applied for multiplying the repetition rate of periodic pulse sequences. This property has also been demonstrated for multiwavelength optical pulse trains [34,35]. The generation of optical pulse trains with ultrahigh repetition rates is of vital importance in fields such as ultrafast data processing optical computing systems or ultra-high-bit-rate optical communications among others. Despite it has been much progress on direct generation of high-repetition rate pulse trains from semiconductor or fiber lasers, it is always advantageous to have simpler methods for further increasing the pulse rate [36–39]. To day the highest repetition rate reached by means of Talbot devices is 2.5 THz, which was achieved by multiplying 250× a 10 GHz train of pulses which had been previously compressed [40].

Talbot effect has also been applied to demostrate new types of mode-locked lasers [41, 42]. Moreover and since Talbot effect is a linear phenomenon, it allows integration with other linear processing techniques, such as compression [43, 44] or reshaping [28, 45]. Its tunability has also been demonstrated by the use of tunable dispersive lines [46, 47], and by switching to soliton regimen [48]. Talbot dispersive lines have also been used together with nonlinear phenomena [42, 47, 49] and temporal imaging systems [32].

Although the experimental analysis of the Talbot-imagined trains usually focuses on the time domain, much information ca be inferred from a spectral analysis of the intensity of the train [24, 25]. In conventional filters designed to increase the repetition rate based on optical spectral filtering, a linear filter suppresses the optical harmonics of the input train that do not belong to the high-frequency output train [47]. Therefore the performance of these systems can be analyzed from the optical transfer function of the linear filter. In contrast, and because dispersion is a phase-only filter in the optical domain, Talbot dispersion filtering is nonlinear and requires a spectral analysis in the intensity domain.

Here we present a theoretical study of Talbot devices, taking into account practical considerations regarding both the incoming sequence of pulses and the dispersive medium. The study is mostly carried out in spectral domain by means of intensity spectrum, which leads to present Talbot lines as a nonlinear filter. The work is divided in tree chapters. In

the first one the basis of space-time duality and the temporal Talbot effect are briefly reviewed. Likewise we analyze in terms of intensity spectrum how dispersive lines with arbitrary first and second order dispersion act on a sequence pulses. Subsequently, these results are particularized to a Talbot line, thus showing the mechanism of image formation depending on Talbot index. The deterioration due to second-order dispersion as well as the stability and tolerance of Talbot devices against timing and frequency variations are also tackled.

In the second chapter we investigate the restoration capability of Talbot effect. This property is well-known in diffractive optics and has been exploited to smooth imperfections of a grating. Here we study non-ideal trains after its propagation in a Talbot line. In particular we analyze first trains of on-off-keyed pulses and later trains of pulses suffering from timing jitter. In both cases the imperfections of the pulse sequence are random and therefore the presented analysis of Talbot lines is not deterministic but stochastic.

Chapter 3 deals with the influence of the coherence of the wave on Talbot devices. We first study the behavior of an arbitrary signal in a linear time-invariant system under partially coherence conditions. When the linear system is a lowest-order dispersive line the effect of the coherence on the temporal signal can be expressed as a low pass filter. These results are particularized for Talbot devices. A matrix analysis of Talbot lines is also reported, presenting the information entropy of the system as a measured of the overall degree of coherence of the system.

Chapter 1

Temporal Talbot effect

1.1 Introduction

The Talbot effect is widely known as a coherent phenomenon, which takes place in the paraxial diffraction region when a periodic object is illuminated by a coherent source [21, 22]. It consists in the formation of self-images or replicas of the object at certain distances along the propagation direction, and has its origin in the interference among diffraction orders of the grating. At certain distances from the object exact replicas are found, which are called integer Talbot images. Between two integer Talbot planes, patterns whose unit cells are formed by the coherent superposition between shifted cells. These patterns are called fractional Talbot images. If cells are confined enough to avoid overlapping between neighboring cells, replicas of the grating but with a periodicity lower than that of the original pattern are achieved, which is known as fractional Talbot effect. Both integer and fractional Talbot effects have been proved and applied not only in free space but in inhomogeneous [50, 51] and waveguide media [52], where the propagating modes play the role of the diffracted orders in free space.

The same phenomenon is found in the time domain when a periodic signal propagates in a dispersive medium [19, 27, 28, 53]. This fact, is a consequence of the well-known mathematical analogy between the equations governing one-dimensional paraxial diffraction and lowest-order dispersion for narrowband signals [1, 2]. In this context, the pulse envelope is equivalent to the complex amplitude distribution, dispersion is equivalent to diffraction and the periodicity of the grating corresponds to the periodicity of the temporal sequence. Thus, when the accumulated dispersion of the medium is a multiple of a basic scale replicas of the input

train of pulse are achieved [20]. Furthermore if accumulated dispersion is a fraction of the mentioned basic scale, a sequence of pulses with a repetition rate higher than that of the original train is obtained, as long as pulse are narrow enough to avoid overlapping [1]. This property has been widely exploited and nowadays Talbot devices constitute a well a well-established all-optical technique to increase the repetition rate of a train of pulses [20, 25–28, 54–56].

This chapter deals with the analysis of the temporal Talbot effect, and is organized as follows. In section 1.2, we present the basis of the space-time duality. The integer and fractional Talbot conditions in both space and time domain are established in section 1.3. The analytical study of the intensity of an arbitrary train of pulses after integer and fractional Talbot device is also reported. Section 1.4 is devoted to the analysis of a train of linearly chirped Gaussian pulses which propagates through an arbitrary second-order dispersion medium. This analysis is carried out in the Fourier domain by means of the intensity spectrum. These results are particularized for a dispersive line satisfying Talbot condition in section 1.5. Some examples are presented to show how the reconstruction of the train takes place, as well as the deleterious of the resulting train due to the presence of second order dispersion. Sections 1.6 and 1.7 are respectively devoted to the analysis of the rejection capability and stability of Talbot lines under fiber length and timing variations. Finally we end the chapter presenting our conclusions.

1.2 Space-Time Duality

The so-called space-time duality involves the equivalent behavior of space-limited beams propagating in free space and narrow band signals in a first-order dispersion medium. This analogy is based on the mathematical equivalence between the equations describing one-dimensional paraxial diffraction and narrow-band dispersion [1]. Both equations are derived from the wave equation by assuming two straightforward approximations. They are: monochromatic waves and paraxial rays for the spatial case; and narrowband fields for the temporal case [2].

In a linear non-magnetic medium with dielectric constant ϵ the space-time evolution of the electric field, $\mathbf{e}$, is governed by the wave equation,

$$\nabla^2 \mathbf{e} = \mu_0 \epsilon \frac{\partial^2 \mathbf{e}}{\partial t^2}, \tag{1.1}$$

∇^2 and μ_0 being the Laplacian operator and the magnetic permeability, respectively. Since the field components in Eq. (1.1) are uncoupled, the wave equation can be expressed without loss of generality in scalar form. From the wave equation we will derive the paraxial diffraction and first-order dispersion equations by setting the above mentioned approximations.

1.2.1 Paraxial diffraction equation

In order to achieve the paraxial equation, the electric field is assumed to be a monochromatic wave with frequency ω_0, $e(x, y, z, t) = e_0(x, y, z) \exp(i\omega_0 t)$. The time derivations are now multiplicative factors ($\partial/\partial t \rightarrow i\omega_0$), converting the wave equation (1.1) into the Helmholtz equation,

$$(\nabla^2 + k^2)e_0 = 0, \tag{1.2}$$

where $k = \mu_0 \epsilon {\omega_0}^2$ is the wave number. We are interested in the study of paraxial rays, i. e., rays confined mostly along the propagation direction z. Therefore, the most rapid spatial phase variations take place in z direction, and the electric field can be rewritten as

$$e_0(x, y, z) = \psi(x, y, z) \exp(-ikz). \tag{1.3}$$

$\psi(x, y, z)$ is the complex amplitude distribution and varies slowly compared with the wavenumber k. The paraxial approximation implies that the curvature of the electric field in propagation direction is much less than the curvature of the transversal profile,

$$\left|\partial^2/\partial z^2\right| \ll \left|\partial^2/\partial x^2\right|, \ \left|\partial^2/\partial y^2\right| \ \text{and} \ \ 2k\left|\partial/\partial z\right|. \tag{1.4}$$

Under this conditions the Helmholtz equation results in

$$\frac{\partial \psi}{\partial z} + \frac{i}{2k}\nabla_t^2 \psi = 0, \tag{1.5}$$

∇_t^2 being the transversal Laplacian operator. Eq. (1.5) is known as parabolic or paraxial equation and governs the evolution of the electric field of a monochromatic beam propagating down z-axis.

1.2.2 Dispersion Equation

The temporal analogy for the paraxial equation appears by considering narrowband waves propagating through a first-order dispersive medium. In order to derive the narrowband dispersion equation we suppose the electric field to be narrowband centered at ω_0. Then, it can be conveniently rewritten as

$$e(x, y, z; t) = e_0(x, y, z; t) \exp(i\omega_0 t) \tag{1.6}$$

By using expression (1.6), the wave equation, Eq. (1.1), in scalar way is expressed in the Fourier domain as

$$\nabla^2 E_0(x, y, z; \omega - \omega_0) + \mu_0 \epsilon \omega^2 E_0(x, y, z; \omega - \omega_0) = 0, \tag{1.7}$$

where $E_0(x, y, z; \omega - \omega_0)$ is the Fourier transform of $e_0(x, y, z; t)$ evaluated at $\omega - \omega_0$, that is, the frequency measured with respect to the central frequency ω_0. Thus, $E_0(x, y, z; \omega - \omega_0)$ represents the electric field at baseband. Equation (1.7) can be solved by using the method of separation of variables [5]. If we assume a solution of the form

$$E_0(x, y, z; \omega - \omega_0) = F(x, y) A(z, \omega - \omega_0) \exp(-i\beta_0 z), \tag{1.8}$$

where $A(z, \omega - \omega_0)$ is a slowly varying function of z and β_0 is the wave number at the carrier frequency to be determined later. Equation (1.7) leads to the following two equations for $F(x, y)$ and $A(z, \omega - \omega_0)$:

$$\frac{\partial^2 F(x, y)}{\partial x^2} + \frac{\partial^2 F(x, y)}{\partial y^2} + \left[\mu_0 \epsilon \omega^2 - \beta(\omega)^2\right] F(x, y) = 0, \tag{1.9}$$

$$2i\beta_0 \frac{\partial A(z, \omega - \omega_0)}{\partial z} - \left[\beta(\omega)^2 - \beta_0^2\right] A(z, \omega - \omega_0) = 0. \tag{1.10}$$

In obtaining Eq. (1.10), the second derivative $\partial^2 A(z, \omega - \omega_0)/\partial z^2$ was neglected since $A(z, \omega - \omega_0)$ is assumed to be a slowly varying function of z. The wave number $\beta(\omega)$ as well as the transversal profile of the electric field, $F(x, y)$, are determined by solving the eigenvalue equation (1.9). $F(x, y)$ represents the the modal distribution, and for single-mode fibers, corresponds to the modal distribution of the fundamental fiber mode given by equations (1.8), and (1.9). We are interested in the second equation (1.10) which governs the time profile evolution of the electric field. It can be written as

$$\frac{\partial A(z,\omega-\omega_0)}{\partial z} = -i\left[\beta(\omega)-\beta_0\right]A(z,\omega-\omega_0) \tag{1.11}$$

where we have approximated $\beta(\omega)^2-\beta_0^2$ by $2\beta_0(\beta(\omega)-\beta_0)$. This equation represents a linear time-invariant system with transfer function [3]

$$H(z,\omega) = \exp[-i(\beta(\omega)-\beta_0)z]. \tag{1.12}$$

The interpretation of equation (1.11) is clear. Each spectral component within the pulse envelope acquires, as it propagates, a phase shift whose magnitude is frequency dependent. Assuming a narrowband signal centered at ω_0, the propagation constant, $\beta(\omega)$, can be expanded in Taylor series around the central frequency ω_0, as follows

$$\beta(\omega) \cong \beta_0 + \beta_1(\omega-\omega_0) + \frac{\beta_2}{2}(\omega-\omega_0)^2 + \frac{\beta_3}{6}(\omega-\omega_0)^3, \tag{1.13}$$

where $\beta_0 = \beta(\omega_0)$ is the propagation constant at the central frequency, $\beta_1 = d\beta(\omega)/d\omega|_{\omega=\omega_0}$ is the inverse of the group velocity and $\beta_2 = d^2\beta(\omega)/d\omega^2|_{\omega=\omega_0}$ and $\beta_3 = d^3\beta(\omega)/d\omega^3|_{\omega=\omega_0}$ are the first and second-order dispersion coefficient respectively. By using Eq. (1.13), Eq.(1.11) is given, in the temporal domain, by

$$\left(\frac{\partial}{\partial z} + \beta_1\frac{\partial}{\partial t} - i\frac{\beta_2}{2}\frac{\partial^2}{\partial t^2} - \frac{\beta_3}{6}\frac{\partial^3}{\partial t^3}\right)a(z,t) = 0. \tag{1.14}$$

where $a(z,t)$ is the optical slowly varying pulse envelope. It corresponds to the Fourier transform of $A(z,\omega-\omega_0)$, so that the optical envelope $a(z,t)$ is expressed in baseband. By introducing a change of variables to traveling-wave coordinate system, $\tau = t-\beta_1 z$, Eq. (1.14) results in

$$\left(\frac{\partial}{\partial z} - i\frac{\beta_2}{2}\frac{\partial^2}{\partial t^2} - \frac{\beta_3}{6}\frac{\partial^3}{\partial t^3}\right)a(z,t) = 0. \tag{1.15}$$

This is the narrowband dispersion equation expressed in the proper reference frame. If the propagation medium is pure first-order dispersion ($\beta_3 = 0$), Eq. (1.15) is written:

$$\frac{\partial a(z,\tau)}{\partial z} = i\frac{\beta_2}{2}\frac{\partial a(z,\tau)}{\partial \tau^2}. \tag{1.16}$$

It is apparent now the mathematical equivalence between first-order dispersion equation (1.16) and the paraxial diffraction equation (1.5) when only one transversal dimension is relevant. They are parabolic equations

Space domain	Time domain
z	z
x	τ
k	$-1/\beta_2$
$\psi(x,z)$	$a(\tau,z)$

Table 1.1: Conversion table between space and time domain

which describe the evolution of the envelope field in space and time domain respectively. The comparison between dispersion and one dimension paraxial equation leads to the conversion table 1.1. Therefore, any medium enable to provide flat amplitude and linear group delay over the bandwidth of the signal, is adequate to reproduce the time-domain equivalent to paraxial diffraction effects. The most common mediums used are: single mode fiber (SMF) and linearly chirped fiber grating (LCFG) [57]. SMF is a good first-order dispersion medium as long as the the required fiber length is not too long and the bandwidth of the signal is narrow. Otherwise the second-order dispersion coefficient becomes relevant and must be taken into account [25]. In these cases, LCFG are more adequate since they can be specifically designed for the system requirements in terms of bandwidth and group delay [58, 59]. Nowadays the fabrication techniques of Bragg gratings are well established [57] and the resulting device is compact (a few centimeters) compared with a single mode fiber (several kilometers of fiber). However, the Bragg gratings could also present some disadvantages respect to SMF, such as deviations in the average dispersion as well as high frequency ripples in the group delay response [60].

1.3 Temporal Self-Imaging Effect

The spacial Talbot effect entails the formation of self-images of a periodic object along the propagation direction [21, 22]. The self-images or Talbot images are the result of the coherent interference between all diffraction orders. For uniform illumination the Talbot planes are those satisfying the condition,

$$z_{\gamma/\alpha} = \frac{\gamma}{\alpha}\frac{d^2}{\lambda_0}, \tag{1.17}$$

where d is the period of the object, $\lambda_0 = 2\pi/k_0$ the wavelength of the illuminating source and γ and α are coprime and integer numbers. For $\alpha = 1$, exact images of the periodic object are found shifted by half a period when γ is odd. These planes are called integer Talbot planes. For $\alpha \neq 1$ periodic patterns with a richer structure are found. In these cases, each cell in the pattern is composed of the coherent superposition of α replicas of the original one mutually shifted by d/α, with a phase difference between them and with power reduced by $1/\alpha$. These are called fractional Talbot images. In case of the structure of cells is sufficiently confined to avoid superposition between neighboring cells, the pattern results in a replica of the original one but with a period α times smaller, shifted again by half a period if $\alpha\gamma$ is odd.

According to the space-time duality the temporal analogy of the self-imaging effect appears when a coherent periodic temporal signal is propagated through a dispersive line, under first-order conditions. Here we will centered our attention on the temporal Talbot effect applied to the increasing of the repetition rate. We will describe it in terms of intensity since it is in this domain where the multiplication of the repetition rate of the train takes place. We consider an input signal with a repetition period t_0. Notice that this periodic signal is the temporal equivalent of the periodic complex amplitude distribution, in such a way that the repetition time t_0 corresponds to the spatial period d. Mathematically, the optical envelope of the input periodic signal can be expressed as

$$a(t,0) = f(t) \otimes \sum_{m=-\infty}^{+\infty} \delta(t - mt_0) = \sum_{m=-\infty}^{+\infty} a_m \exp(i2\pi mt/t_0), \qquad (1.18)$$

where $\otimes$ denotes the convolution operation. $f(t)$ represents an arbitrary pulse shape confined within $|t| < t_0/2$, so that the incoming optical intensity is $I(t,0) = |f(t)|^2 \otimes \sum_k \delta(t - kt_0)$. The set of variables a_m represents the harmonics of the signal, $a_m t_0 = F(\omega = m2\pi/t_0)$, $F(\omega)$ being the Fourier transform of the pulse profile $f(t)$.

As has been shown in previous section a linear first-order dispersion medium is a linear time-invariant system, so that it is completely characterized by its transfer function, $H(\omega, z)$ [3]

$$H(\omega, L) = \exp\left(-i\beta_2 z\omega^2/2\right), \qquad (1.19)$$

or equivalently by its impulse response, $h(t,z)$ which is the inverse Fourier transform of the transfer function

$$h(t,z) = \mathrm{FT}^{-1}[H(\omega,z)] = (i2\pi\beta_2 z)^{-1/2}\exp(it^2/2\beta_2 z). \tag{1.20}$$

t represents the proper time, that is, the time expressed in the reference frame moving with the pulse, $t = t_{phy} - \beta_1 z$, t_{phy} being the physic time. After traveling a distance z in a dispersive medium described by Eq. (1.19)-(1.20), the resulting optical envelope, $a(t,z)$ can be expressed as the convolution of the complex envelope of the input pulse with the impulse response, $a(t,z) = a(t,0)\otimes h(t,z)$. According with the convolution theorem, the optical signal can be equivalently computed in the Fourier domain by directly multiplication of the spectrum of the incoming signal, $A(\omega,0)$ with the transfer function, $A(\omega,z) = H(\omega,z)A(\omega,0)$. Thus, the dispersed optical envelope results in:

$$a(t,z) = \sum_{m=-\infty}^{+\infty} a_m \exp(i2\pi mt/t_0)\exp(-i2\pi^2 m^2\beta_2 z/t_0^2) \tag{1.21}$$

We now proceed to the analysis of the optical intensity for dispersive lines satisfying Talbot condition. We firstly derive the resulting optical intensity under integer Talbot conditions, and subsequently in subsection 1.3.2 fractional Talbot lines are analyzed.

1.3.1 Integer Talbot effect

The integer Talbot condition, in time domain, is directly derived by setting $\alpha = 1$ in Eq. (1.17) and making use of the conversion table 1.1:

$$|\beta_2| z_\gamma = \gamma\frac{t_0^2}{2\pi}, \tag{1.22}$$

where γ is an integer number. Under this condition the optical envelope, Eq. (1.21) is expressed as

$$a(t,z_\gamma) = \sum_{m=-\infty}^{+\infty} a_m\ e^{i2\pi mt/t_0}\ e^{-i\pi m^2\gamma} \tag{1.23}$$

The second phase element in Eq. (1.23), $e^{-i\pi m^2\gamma}$ can be reexpressed as a linear phase in the index m, $e^{-i\pi m\gamma}$. It means that integer Talbot lines with odd values of γ introduce a phase difference of π between consecutive harmonics which is translated into a shifting of half a period in the time domain. The output optical intensity, $I(t,z_{\gamma/\alpha}) = |a(t,z_{\gamma/\alpha})|^2$, results in

$$
\begin{aligned}
I(t, z_\gamma) &= \sum_{m=-\infty}^{m=+\infty} \sum_{k=-\infty}^{+\infty} a_k \; a_{k-m}^{*} \exp(i2\pi m(t-\overline{\tau})/t_0) \\
&= \sum_{m=-\infty}^{+\infty} C_k \exp(i2\pi m(t-\overline{\tau})/t_0)
\end{aligned}
\tag{1.24}
$$

where $\overline{\tau}$ is equal to $t_0/2$ when γ is odd and is null if γ is even, and the set of variables C_k account for the harmonics of the optical intensity. Since the single pulse profile $f(t)$ is contained in $[-t_0/2, t_0/2]$, Eq. (1.24) can also be written as

$$
I(t, z_\gamma) = |f(t)|^2 \otimes \sum_{m=-\infty}^{+\infty} \delta(t - \overline{\tau} - mt_0) \tag{1.25}
$$

Then, if condition (1.22) is verified, the dispersed signal intensity reproduces exactly the original sequence of pulses, for even values of γ. When γ is odd, the only difference is that the obtained intensity train undergoes a delay of half a period with respect to the original one.

1.3.2 Fractional Talbot effect

Let us assume now that the accumulated dispersion of the medium verifies the temporal fractional Talbot condition,

$$
|\beta_2| z_{\gamma/\alpha} = \frac{\gamma}{\alpha} \frac{t_0^2}{2\pi}, \tag{1.26}
$$

where γ/α is a non-integer and irreducible rational number. Under this condition, the optical envelope is given by

$$
a(t, z_{\gamma/\alpha}) = \sum_m a_m \; e^{i2\pi m t/t_0} \; e^{-i\pi m^2 \gamma/\alpha} \tag{1.27}
$$

which leads the output intensity to a more complex form than that in integer Talbot device. It can be written as

$$
I(t, z_{\gamma/\alpha}) = \sum_{m=-\infty}^{+\infty} I_m \exp(i2\pi m t/t_0) \tag{1.28}
$$

where

$$I_m = \exp(i\pi m^2\gamma/\alpha) \sum_{k=-\infty}^{+\infty} a_k a_{k-m}^* \exp(-i2\pi mk\gamma/\alpha) \tag{1.29}$$

By introducing the changes of variables $m = \alpha p + q$ and $k = \alpha r + s$, Eq. (1.29) is written as

$$\begin{aligned} I_{\alpha p+q} =& \exp(i\pi\gamma\alpha p^2) \exp(i\pi q^2\gamma/\alpha) \sum_{s=0}^{\alpha-1} \exp(-i2\pi qs\gamma/\alpha) \\ & \times \sum_{r=-\infty}^{+\infty} a_{\alpha r+s} a_{\alpha r+s-\alpha p-q}^* \end{aligned} \tag{1.30}$$

It can be shown that the second sum in Eq. (1.30) does not depend on s as long as the input pulse form, $f(t)$ is confined in the interval $[-t_0/2\alpha, -t_0/2\alpha]$ (the demonstration is sketched in Appendix A). Then, making use of the equality, $\sum_{s=0}^{\alpha-1} \exp(-i2\pi sq\gamma/\alpha) = \alpha\ \delta_{q,0}$, the intensity after the fractional Talbot device, is notably simplified,

$$\begin{aligned} I(t, z_{\gamma/\alpha}) =& \alpha \sum_{m=-\infty}^{+\infty} \sum_{r=-\infty}^{+\infty} a_{\alpha r}\ a_{\alpha r-\alpha m}^* \exp(i2\pi\alpha m(t-\overline{\tau})/t_0) \\ =& \sum_{m=-\infty}^{+\infty} C_{\alpha m} \exp(i2\pi\alpha m(t-\overline{\tau})/t_0), \end{aligned} \tag{1.31}$$

where $\overline{\tau}$ stands for $t_0/2$ when the product $\alpha\gamma$ is odd and for zero otherwise, and $C_{\alpha m}$ are the α-harmonics of the input intensity train. Since pulses are confined in $|t| < t_0/2\alpha$, the output intensity can also be expressed as

$$\begin{aligned} I(t, z_{\gamma/\alpha}) =& \frac{1}{\alpha} \sum_{m=-\infty}^{+\infty} \delta(t - \overline{\tau} - mt_0/\alpha) \otimes |f(t)|^2 \\ =& \frac{1}{\alpha} \sum_{m=1}^{\alpha} \delta(t - \overline{\tau} - mt_0/\alpha) \otimes I(t, 0). \end{aligned} \tag{1.32}$$

Then, the output intensity replicates the input periodic sequences with a repetition rate α-times higher than that of the original train, shifted by half a period in case the product $\alpha\gamma$ is odd. The increase of the repetition rate is only limited by pulse overlap. Then, the maximum value of α is given

by t_0/S_f, S_f being the overall time duration of a single pulse $f(t)$. The repetition rate increase process does not affect the temporal waveform, that is, pulse shape and duration, of the original train within each individual pulse. The temporal waveform is only attenuated by a factor α, which guarantees energy conservation. It is owing to the fact that dispersive media, such Talbot devices, are pure phase filters, since they only alter the phase of the original spectrum.

1.4 Intensity Spectrum in Dispersive Lines

This section is devoted to the analysis of the intensity spectrum of a periodic train of pulses propagating in a dispersive line with arbitrary first and second-order dispersion coefficients (β_2 and β_3, respectively). Higher-order dispersion is considered negligible. We will analyze the effect of β_3 because it is the first aberration in fiber lines. Second-order dispersion is also present in LCFG but for these media distortions due to ripples are more important [61]. The equation governing the evolution of the optical envelope $a(t,z)$ will be given by equation (1.15):

$$\frac{\partial a}{\partial z} - \frac{i}{2}\beta_2 \frac{\partial^2 a}{\partial t^2} - \frac{1}{6}\beta_3 \frac{\partial^3 a}{\partial t^3} = 0 \tag{1.33}$$

Let us assume that such a dispersive line is fed with a periodic train of linearly chirped Gaussian pulses:

$$a(t,0) = \sum_{k=-\infty}^{+\infty} \exp[-(t-kt_0)^2(1-iC)/2t_p^2], \tag{1.34}$$

where C is the linear chirp or phase-modulation parameter of the pulses, t_p is their width, measured as the half-width at 1/e-decay in power, and t_0 is the period of the train. The repetition rate of the train will be described by its angular frequency, $\Omega_0 = 2\pi/t_0$. The propagation of the amplitude, Eq. (1.34), in a dispersive medium of length L can be solved in Fourier domain $A(\omega, L) = H(\omega, L)A(\omega, 0)$. In this formula, the input field is:

$$\begin{aligned} A(\omega,0) =& t_p[2\pi/(1-iC)]^{1/2} \exp[-(1+iC)\omega^2/2\sigma_\omega^2] \\ & \times \Omega_0 \sum_m \delta(\omega - \Omega_0 m), \end{aligned} \tag{1.35}$$

where the sum ranges from $-\infty$ to $+\infty$ and $\sigma_\omega = (1+C^2)^{1/2}/t_p$ is the optical spectral width of the individual pulses, measured as the half-width at 1/e decay in power; and $H(\omega, L)$ is the transfer function of linear propagation:

$$H(\omega, L) = \exp(-i\beta_2 L\omega^2/2 - i\beta_3 L\omega^3/6). \tag{1.36}$$

Due to the structure of quadratic phases in Eq. (1.35) and (1.36) we define, for future use, the equivalent dispersion of the line as:

$$D_{eq} = \left|\beta_2 L + C/\sigma_\omega^2\right|. \tag{1.37}$$

This is the relevant quantity when considering linear pulse compression in a dispersive line [5].

Since dispersion is an only phase filter, Eq. (1.36), the power spectrum of the optical envelope, $|A(\omega, L)|^2$, remains invariant along the medium. However, if detection occurs after the dispersion line, the generated photocurrent is proportional to the squared train envelope $i(t, L) = |a(t, L)|^2$. Detection is a nonlinear transformation of the optical envelope, $a(t, L)$ or $A(\omega, L)$, so that dispersion-induced phases causing pulse spreading can show now observable consequences. We will assume that the detection bandwidth is larger than the linewidth of intensity, so that the detection is able to follow the train envelope.

The detected signal after its propagation through the dispersive line, $i(t, L)$, is given in the spectral domain $I(\omega, L)$ by the auto-correlation of $A(\omega, L)$. The result is:

$$I(\omega, L) = \Omega_0 \zeta(\omega)^{-1/2} J(\omega) Z(\omega) \sum_k \delta(\omega - k\Omega_0), \tag{1.38}$$

where:

$$\zeta(\omega) = 1 + i\beta_3 L\sigma_\omega^2 \omega/2, \tag{1.39}$$

$$J(\omega) = t_p\sqrt{\pi}\exp\left(-\frac{\omega^2}{4\sigma_\omega^2} - \frac{i\omega^2 Im(\zeta(\omega))}{12\sigma_\omega^2}\right) \tag{1.40}$$

$$Z(\omega) = \sum_n g_n(\omega)\exp(\frac{-i\omega n t_0}{2}) \tag{1.41}$$

and

$$g_n(\omega) = \exp\left[-\frac{(\omega-\omega_n)^2 D_{eq}^2 \sigma_\omega^2}{4\zeta(\omega)}\right] \tag{1.42}$$

where $\omega_n = nt_0/D_{eq}$, and $Im(\zeta(\omega))$ is the imaginary part of $\zeta(\omega)$. From Eq. (1.38), the two-sided power spectrum density (PSD) of the train intensity can be computed:

$$S(\omega, L) = \Omega_0 \left|J(\omega)Z(\omega)\right|^2 \left|\zeta(\omega)\right|^{-1} \sum_k \delta(\omega - k\Omega_0). \tag{1.43}$$

The power carried by each harmonic is determined by the smooth functions $J(\omega)$ and $\zeta(\omega)$ and the peaked function $Z(\omega)$. The first function $J(\omega)$ is broadband and its modulus dispersion-independent. Its bandwidth, measured as the half-width of 30-dB decay in power, is $3.72\sigma_\omega$. This function determines the highest significant frequency of the RF spectrum, $\omega_{max} \cong 3.72\sigma_\omega$.

On the other hand $\zeta(\omega)$ contains the only dependence on β_3 in (1.43), and therefore this function determines the influence of second-order dispersion in the spectrum. It will be negligible, $\zeta(\omega) \cong 1$, when its value for the highest significant frequency is negligible. Therefore, we will describe the relative influence of β_3 by the following angular parameter:

$$\epsilon = 1.86\beta_3 L\sigma_\omega^2, \tag{1.44}$$

so that negligible β_3 is equivalent to $\epsilon \ll \pi$. Non-negligible values of ϵ account for a narrowing of the total bandwidth of the spectrum through the factor $|\zeta(\omega)|^{-1}$ in (1.43).

Finally, function $Z(\omega)$ is essentially a sum of dispersion-dependent peaked functions $g_n(\omega)$, indexed by an integer number n. These functions are centered at $\omega_n = nt_0/D_{eq}$ and, when β_3 is negligible, their functional form is Gaussian. In this limit, the spectral width of all functions $g_n(\omega)$ is proportional to $1/\sigma_\omega D_{eq}$. Then, these functions are narrower as the spectral width of the pulses is larger. Furthermore, they get broader as the equivalent dispersion D_{eq} reduces, and lie closer to each other as the dispersion increases. In other words, the structure of $g_n(\omega)$ depends on dispersion like an accordion that gets progressively closed as the dispersion increases. When β_3 is not negligible, the functional form of $g_n(\omega)$ becomes non-Gaussian. Their width is enlarged progressively along the RF spectrum through the factor $\zeta(\omega)$ in Eq. (1.42), although their global behavior is similar.

From the temporal point of view, interference patterns in the intensity profile arise due to the dispersion-induced spreading of coherent pulses [62]. In the classical analysis of pulse-sequence interference [63–67], the attention was paid on the limitations in binary transmission rates induced by

intersymbol interference. Some of these papers base their characterization on the comparison of the Fourier-domain intensity of the pulse sequence after dispersion with the spectrum of a single pulse after the same amount of dispersion [66, 67]. From this comparison it can be inferred the distortions induced in the intensity profile by multiple pulse interference. With our notation, the single pulse Fourier-domain intensity is:

$$I_{SP}(\omega, L) = \zeta(\omega)^{-1/2} J(\omega) g_0(\omega), \tag{1.45}$$

where SP stands for single pulse, and its associated intensity spectrum, $S_{SP}(\omega, L)$, is the squared modulus of (1.45). Then, Eq. (1.43) can be rewritten as:

$$S(\omega, L) = \Omega_0 S_{SP}(\omega, L) \left| Z(\omega)/g_0(\omega) \right|^2 \sum_k \delta(\omega - k\Omega_0). \tag{1.46}$$

With this notation, the influence of pulse interference is enclosed in the ratio $Z(\omega)/g_0(\omega)$. Due to the structure of function $Z(\omega)$, Eq. (1.41), this ratio can also be expressed as a sum of ratios $g_n(\omega)/g_0(\omega)$. These ratios are precisely the quantities $\exp(Q)$ defined in [67]. The important observation in this context is that the quantities $g_n(\omega)$, with $n \neq 0$, describe the spectral content of the interference pattern arising in the dispersion of a given pulse and its n-th neighbor, whereas $g_0(\omega)$ is associated to the single pulse spectrum. In low-dispersive lines, intersymbol interference can be analyzed from the neighboring-pulse interference ratio $g_1(\omega)/g_0(\omega)$ since next-to-neighboring pulse interference can be neglected. In fact, the basic spectral properties of the ratio $g_1(\omega)/g_0(\omega)$ have been described in Ref. [67]. However, the separation in terms of $g_n(\omega)$ used in Eq. (1.41) will be more appropriate for the analysis of Talbot dispersive lines, as we will analyze in the following sections.

We now illustrate spectrum (1.43) by means of simple examples describing pulse compression and pulse-to-pulse interference in low-dispersion fiber lines. In Figs. 1.1 and 1.2 we show the intensity PSD and the detected temporal signal of a 10-GHz train after its propagation through a standard single-mode fiber (SMF) carried by a monochromatic wave at $\lambda = 1550$ nm ($\beta_2 = -21$ ps^2/km$\cdot$rad and $\beta_3 = 0.13$ ps^3/km$\cdot$rad^2). In Figs. 1.1 and 1.2, the trains are composed of Gaussian pulses with chirp $C = 2$ rad and $t_p = 15$ ps, so that the significant portion of the spectrum extends from DC to 88 GHz. On the left hand side of both figures, we present the positive-frequency portion of the two-sided intensity PSD, Eq. (1.43), and

on the right, the corresponding intensity profiles. The broadband spectral envelope $|J(\omega)|^2/|\zeta(\omega)|$ is depicted with a thin continuous curve. The thick continuous curve represents the product $|J(\omega)Z(\omega)|^2/|\zeta(\omega)|$ that controls the power carried by each harmonic of the output intensity train. The power of the harmonics is the value of this thick line at the multiples of the fundamental frequency $\Omega_0 = 2\pi \times 10$ GHz, which are depicted with dots. On the right hand side, the thin continuous curve represents two periods of the intensity of the input train, and the thick curve two periods of the output intensity. The intensity PSD has been normalized to 0 dB at the carrier, whereas the temporal signals have been normalized to unity in the center of the period to help in visualizing the pulse interference patterns.

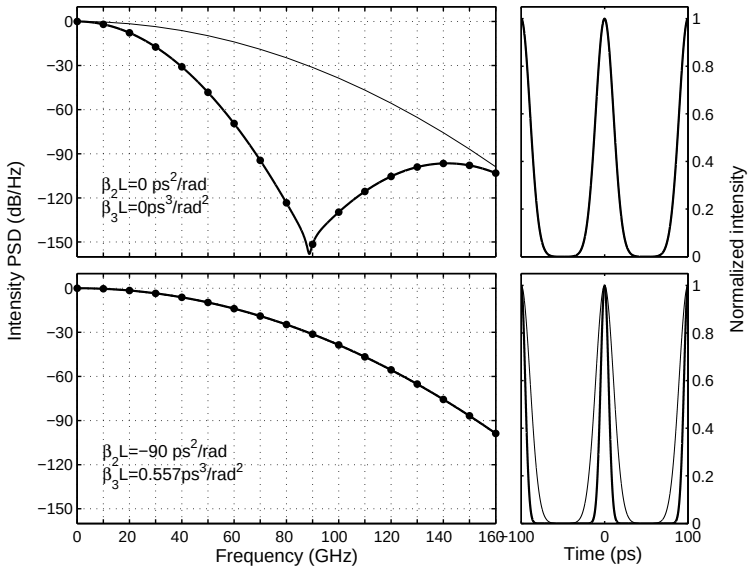

Figure 1.1: *Intensity PSD(left) and temporal intensity (right)of a 10-GHz train before(top) and after (bottom) its propagation in a standard SMF of length* $L = 4.29$ *km (compression length)*

In Fig. 1.1 the trains are propagated through a SMF with two lengths: $L = 0$ (initial train, top) and $L = 4.29$ km (bottom). β_3 is negligible in both examples ($\epsilon = 0$ and $\epsilon = 0.0034$ rad, respectively). The intensity PSD of the input train (top) has two lobes that group the harmonics of the intensity. They are centered at DC and 140 GHz, and are associated to the

first two contributions to the sum (1.41) in Eq. (1.43). Since their spectral overlapping is negligible, the sum can be approximated to $|g_0(\omega)|^2+|g_1(\omega)|^2$. The first lobe $|g_0(\omega)|^2$, together with the overall envelope, represents the intensity spectrum of a single pulse, see Eq. (1.45). The second lobe $|g_1(\omega)|^2$ centered at 140 GHz is due to the slight interference between neighboring Gaussian pulses in the input train. In practice no pulse-to-pulse interference is present in the input train, so that the intensity harmonics should be grouped in a single lobe centered at DC. Additional interference lobes only appear as dispersion causes pulse broadening and subsequent interference [68].

The existence of interference lobes is a limitation of the representation of the input train as a coherent sum of Gaussian pulses: their infinite temporal extension causes pulse-to-pulse overlapping and interference even in the input signal. However, the value of the power of the harmonics describing the neighboring-pulse interference term, more than 90 dB below the carrier, is sufficiently small to rely on the validity of the model.

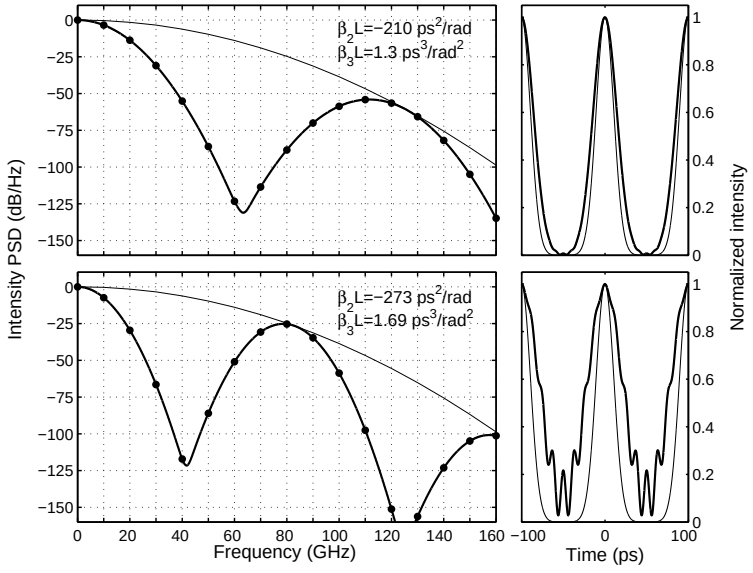

Figure 1.2: *Intensity PSD(left) and temporal intensity (right)of a 10-GHz train after its propagation in a standard SMF of length $L = 10$ km (top) and $L = 13$ km (bottom)*

The second example in Fig. 1.1 (bottom) shows the signal after the compression length $L_C = -C/\sigma_\omega^2\beta_2 = 4.29$ km, where pulses reach the minimum temporal width, $1/\sigma_\omega = 6.7$ ps. At this length the equivalent dispersion, D_{eq} defined in Eq. (1.37), vanishes. This means that $|Z(\omega)|^2 \cong |g_0(\omega)|^2 = 1$, see (1.42) and the definition of ω_n, so that the spectrum follows the envelope $|J(\omega)|^2/|\zeta(\omega)|$. In other words, this envelope is the single-pulse envelope of compressed pulses. This fact can also be derived by setting $D_{eq} = 0$ in Eq. (1.46). Therefore, the factor $g_0(\omega)$ in the single-pulse spectrum (1.46) accounts for the difference between compressed and non-compressed pulse spectra.

In figure 1.2 the fiber length is increased beyond the compression condition up to $L = 10$ km (top) and $L = 13$ km (bottom). The second order dispersion is still negligible ($\epsilon = 0.0080$ rad and 0.0104 rad, respectively). In first example (top figure) the interference between pulses yields an increase in power of the second lobe $|g_1(\omega)|^2$. In temporal domain pulses are broaden and the superposition between neighboring pulse is now apparent. In second example (bottom figure) the power spectrum is composed of tree lobes: $|g_0(\omega)|^2$, $|g_1(\omega)|^2$ and $|g_2(\omega)|^2$ which correspond to single pulse dispersion, interference between neighboring pulses, and interference between alternate pulses, respectively. The lobe $|g_1(\omega)|^2$ has raised in power and its peak is now centered at 80 GHz leading to an increase in power of the harmonics around that frequency. It can be observed in its temporal counterpart as an interference patter with eight maxima per period.

1.5 Intensity Spectrum in Talbot Lines

In section 1.3 we have shown that self-imaging effect can be achieved when a periodic train of pulses, such as (1.34), is propagated in a first-order dispersion medium, whose lowest-order accumulated dispersion is a multiple of the basic scale $t_0^2/2\pi$. This effect can be also achieved by matching the second-order accumulated dispersion or even higher order dispersion [19, 69, 70]. Here we are considering a dispersive line with first and second order dispersion. The Talbot condition will be defined by matching the accumulated first-order dispersion, whereas the second-order dispersion will be considered as a deviation from the ideal behavior. Then, according with Eq. (1.26), the self-images are achieved when the fiber length L satisfies the condition:

$$|\beta_2|L\Omega_0^2 = 2\pi\frac{\gamma}{\alpha}. \tag{1.47}$$

where γ and α are integer and coprime numbers. The quotient γ/α is called Talbot index.

Due to the structure of the quadratic phases in (1.35) and (1.36), another value of total dispersion is of interest:

$$D_{eq}\Omega_0^2 = |\beta_2 L + C/\sigma_\omega^2|\Omega_0^2 = 2\pi\frac{\gamma}{\alpha}. \tag{1.48}$$

We will refer to (1.48) as the compressing Talbot condition. To interpret this condition, let us first consider that the length of the dispersive medium is adjusted to verify (1.48), the output signal is a Talbot image (integer or fractional, depending on α) of a train of compressed pulses. Let us further suppose that phase modulation and dispersion have opposite sign, $C \cdot \beta_2 < 0$, so that the length of the medium can be split in two positive contributions, $L = L_C + L_T$, the first being the compression length and the second the Talbot distance. This first part of the line is used to compress individually the pulses in the train [5], and the remaining length of the fiber, L_T, produces the Talbot image of the train of compressed pulses. If both phase modulation and dispersion have the same sign, $C \cdot \beta_2 > 0$, the compression condition (1.48) produces the same overall result because the final structure of the spectral phases is equal to the previous case, $C \cdot \beta_2 < 0$. The only difference is that the distance of compressing Talbot condition when $C \cdot \beta_2 > 0$ is shorter than the distance when $C \cdot \beta_2 < 0$. Between Talbot and compressing Talbot conditions (1.47) and (1.48), a continuum of partial compression is obtained.

Now we analyze the intensity spectrum of the temporal Talbot effect by means of some representative examples. Let us first consider in Fig. 1.3 an integer self-imaging dispersive line with index $\gamma/\alpha = 1$. Pulses have a width of 15 ps and a chirp $C = 2$ rad, as in Figs. 1.1 and 1.2. The dispersive medium is a SMF at $\lambda = 1550$ nm, and compressing conditions ($L = 80.1$ km) are shown in the figures at the top, while non-compressing conditions ($L = 75.8$ km) are depicted at the bottom. In both examples second-order dispersion is negligible ($\epsilon = 0.064$ rad and 0.061 rad, respectively). The thick continuous curve represents again the function $|J(\omega) \cdot Z(\omega)|^2/|\zeta(\omega)|$ that accounts for the power carried by the output harmonics. At the output of the fiber we get a train of compressed pulses in the first example and a train of non-compressed pulses in the second one, both of them shifted by half a period because γ is odd ($\gamma = 1$). The intensity PSD follows two

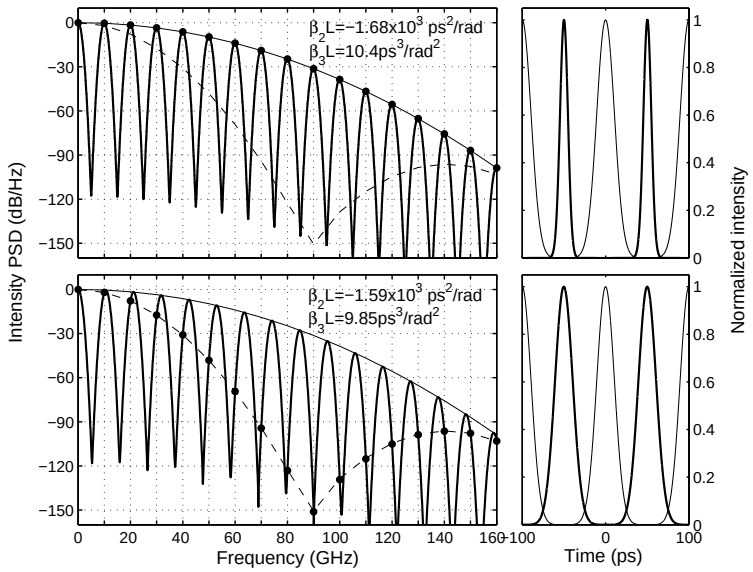

Figure 1.3: *Intensity PSD(left) and temporal intensity (right)of a 10-GHz train after its propagation in a standard SMF of length* $L = 80.1$ *km (top) and* $L = 75.8$ *km (bottom), which correspond to the compressing Talbot and standard Talbot conditions with index* $\gamma/\alpha = 1$*, respectively.*

different curves. The first one (thin continuous curve) corresponds to the intensity spectrum of a compressed pulse, while the second one (dashed curve) follows the spectrum of non-compressed pulses. From Fig. 1.3 we can interpret how Talbot effect creates the self-images of the train. Multiple pulse-to-pulse interference is reflected in the structure of dips and bumps of the function $|J(\omega) \cdot Z(\omega)|^2/|\zeta(\omega)|$. This structure is due to the sum over $g_n(\omega)$ in $Z(\omega)$, see Eq. (1.41). In the absence of second-order dispersion the spectral separation between consecutive functions $g_n(\omega)$ and $g_{n+1}(\omega)$ is t_0/D_{eq}, while their spectral width goes as $1/\sigma_\omega D_{eq}$. Then, for fiber lengths of the order of magnitude of the Talbot distances, $D_{eq} \sim 1/\Omega_0^2$, the spectral overlapping between functions $g_n(\omega)$ can be neglected if $\sigma_\omega \gg \Omega_0$, i.e., if the pulse width is smaller than the period of the input train. Then, $|Z(\omega)|^2$ can be approximated by $\sum_n |g_n(\omega)|^2$ and the intensity PSD can be rewritten as:

$$S(\omega, L) \cong \Omega_0 |J(\omega)|^2 |\zeta(\omega)|^{-1} \sum_s G_s(\omega) \sum_k \delta(\omega - k\Omega_0) \tag{1.49}$$

where $G_n(\omega) = |g_n(\omega)|^2$. Dispersion thus acts as a multiple bandpass filter, the positions and width of the passbands being determined by $G_n(\omega)$. Their centers are located at:

$$\omega_n = nt_0/D_{eq}, \tag{1.50}$$

and their 30-dB decay half width is, if second-order dispersion is negligible:

$$\Delta\omega = 3.72/\sigma_\omega D_{eq}. \tag{1.51}$$

Then, from Fig. 1.3 (top), it can be observed that the output harmonics of the compressing Talbot replica of the original train lie at the center of the n-th passband that describes the interference between pulses separated n time slots. In other words, the n-th harmonic of the intensity train is created by interference of pulses separated n time slots. Under non-compressing Talbot condition the behavior of the intensity PSD is similar, but the output harmonics do not lie on the passband's centers, see Fig. 1.3 (bottom). However, the overall picture is similar.

This point of view can be further explored by considering the examples presented in Fig. 1.4. The same train is propagated through a SMF to the compressing Talbot lengths with indices 1/2 and 3/2. The output train is similar, since in both examples the output is a 20-GHz train of transform-limited pulses. Again, second-order dispersion is negligible ($\epsilon = 0.034$ rad and 0.094 rad, respectively). In both examples, the increase of the repetition rate is manifested in the suppression of the odd harmonics of 10 GHz. However, the interference structures are different. In the first example, above, the h-th output harmonic is created by the interference of pulses separated by h time slots, while in the second example, below, it is created by the interference of pulses originally separated by $3h$ time slots.

In general, the passbands associated to compressing Talbot lines are centered at $\omega_n = n\alpha\Omega_0/\gamma$, n being the index determining the interference between pulses separated by n time slots. When n is a multiple of γ, $n = h\gamma$ for certain integer h, the passband is centered at the h-th output harmonic $h\alpha\Omega_0$. Then, if the compressing Talbot line is integer ($\alpha = 1$) the h-th harmonic lies in the center of the passband with index $n = h$, so that all the harmonics survive and between two consecutive harmonics there are $\gamma - 1$ passbands. Conversely, if the compressing dispersive line is fractional ($\alpha \neq 1$), only the frequencies multiples of the α-th input harmonic lie over

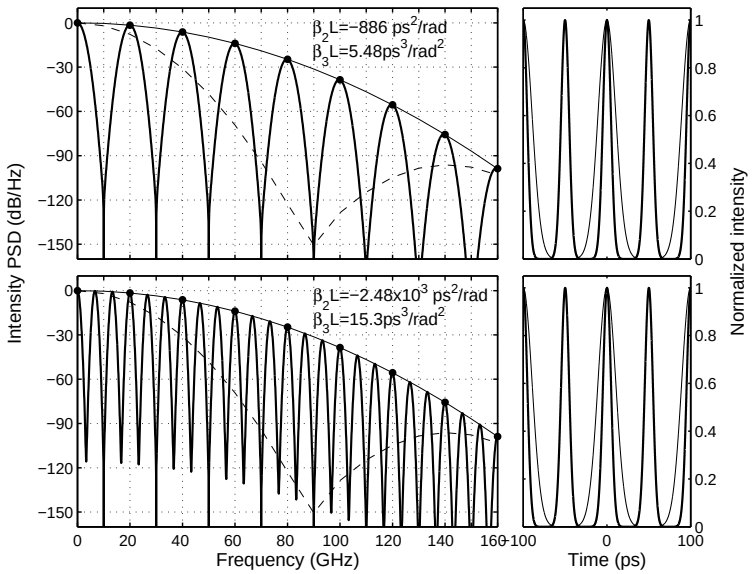

Figure 1.4: *Intensity PSD(left) and temporal intensity (right)of a 10-GHz train after its propagation in a standard SMF of length* $L = 42.2$ *km (top) and* $L = 118$ *km (bottom), which correspond to the compressing Talbot conditions with index* $\gamma/\alpha = 1$ *and* $3/2$*, respectively.*

the center of a passband. These surviving harmonics originate the spectral content of the output train, the remaining harmonics being filtered.

The next example in Fig. 1.5 explores the suppression of harmonics in Talbot devices with index 1/3 and its dependence on the optical linewidth. A 10-GHz train with pulses of width 15 ps is launched into a SMF compressing dispersive line with index 1/3. Above, the chirp parameter of the pulses is $C = 2$ rad, so that the width of the compressed pulses is 6.7 ps. The 1/3 compressing Talbot line has a length $L = 29.5$ km. Below, the chirp parameter of the pulses is $C = 1$ rad, the compressed pulses are 10.6 ps wide, and the corresponding length is 30.6 km. Second-order dispersion is still negligible ($\epsilon = 0.0237$ rad and 0.0062 rad, respectively). We observe that the suppression of harmonics that do not belong to the output 30-GHz train is not exact. These harmonics will be referred to as residual harmonics. The partial suppression of residual harmonics is due to the finite width of the bandpass $G_n(\omega)$, which are, according to (1.51), inversely proportional to the spectral width.

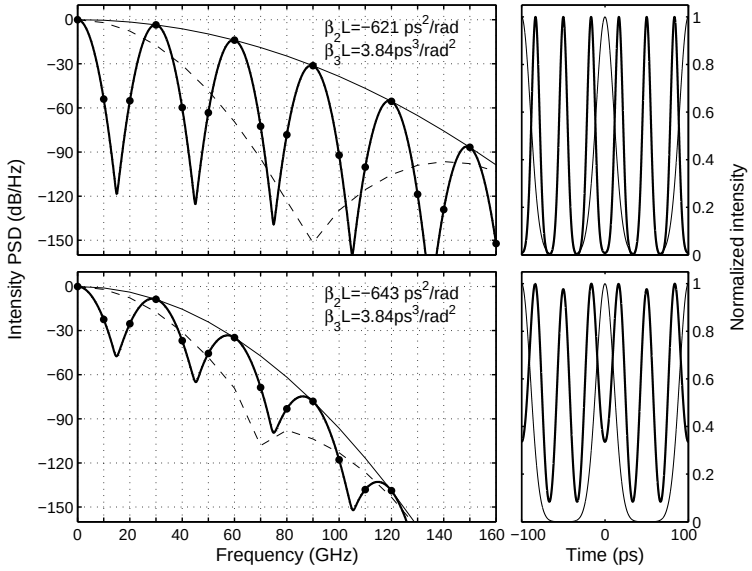

Figure 1.5: *Intensity PSD(left) and temporal intensity (right)of a 10-GHz train after its propagation in a standard SMF of length* $L = 29.5$ *km (top) and* $L = 30.6$ *km (bottom), which correspond to the compressing Talbot conditions with index* $\gamma/\alpha = 1/3$. *Pulses have a width of 15 ps and chirp C=2 rad (top) and C=1 rad (bottom) and* $3/2$.

In Fig. 1.5, below, we observe that a reduction of the spectral width implies, from the temporal point of view, that pulses overlap in the output train causing pulse pedestal and intensity fluctuation. As a result, the temporal profile shows a periodic structure with frequency Ω_0, reflecting the absence of exact repetition-rate multiplication. From the spectral point of view we notice, on one hand, the reduction of the spectral width, and, on the other, the increase of the power carried by residual harmonics, due to the broadening of the passbands $G_n(\omega)$. The inefficient filtering of residual harmonics is clearly shown at 10 and 20 GHz.

It is important to underline that the factional Talbot lines with indices $\gamma/\alpha = (2k+1)/2$ differ form any other fractional Talbot device. In Fig. 1.4 the odd residual harmonics are totally suppressed, independently of the value of the optical spectral width, but this fact is not general [25]. This exact cancelation occurs if the input pulses are transform-limited, i. e., if the input envelope is a real function so that its Fourier coefficients in (1.35)

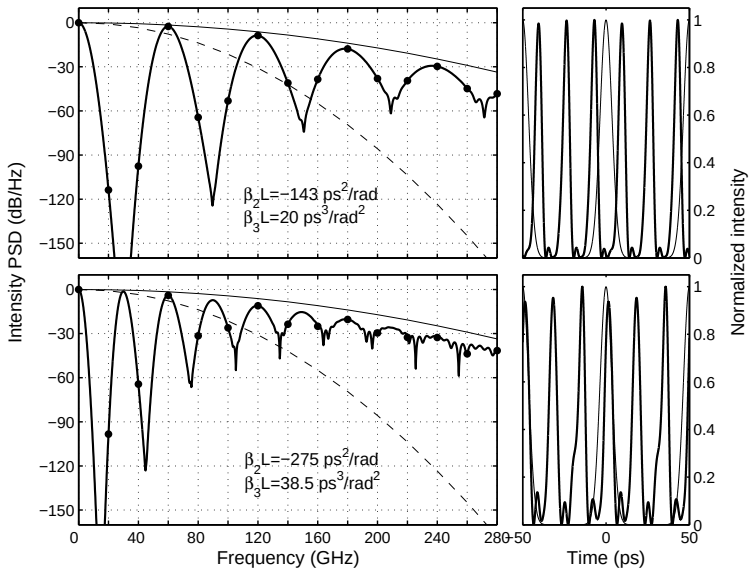

Figure 1.6: *Intensity PSD(left) and temporal intensity (right)of a 20-GHz train after its propagation in a standard DSF of length* $L = 285$ *km (top) and* $L = 551$ *km (bottom), which correspond to the compressing Talbot conditions with index* $\gamma/\alpha = 1/3$ *and* $2/3$*, respectively.*

verify that $\varphi_m = -\varphi_{-m}$. This, together with the spectral phases caused by dispersion, produces a relative phase shift of $\pm\pi$ between optical spectral lines with indices $\pm m$, which implies the total suppression of the residual harmonics. This observation is similar to the well-known carrier suppression effect in analog communications [71]. In fact, compressing Talbot distances with indices $\gamma/\alpha = (2k+1)/2$, and only these distances, coincide with the distances of carrier suppression.

To conclude this section we consider the last example in Fig. 1.6 where second-order dispersion is not negligible. A 20-GHz train of pulses with width 5-ps and chirp $C = 2$ rad is propagated through a dispersion shifted fiber (DSF; $\beta_2 = 0.5$ ps^2/km $\cdot$ rad and $\beta_3 = 0.07$ ps^3/km $\cdot$ rad^2 at $\lambda = 1550$ nm), whose length is adjusted to verify the compressing Talbot condition $\gamma/\alpha = 1/3$ (top) and $2/3$ (bottom). The thin continuous and dashed curves represent the envelope of the intensity PSD that would correspond to the compressing Talbot and non-compressing Talbot condition, respectively, if the second-order dispersion coefficient was zero.

The thick continuous and the thin dotted curves are the envelope $|f(\omega) \cdot J(\omega)|^2/|\zeta(\omega)|$. Finally, the dots represent the harmonic content of the output train.

The top figure 1.6 ($\epsilon = 3.32$ rad) shows a slight decrease of overall bandwidth, as compared with the case $\beta_3 = 0$, and a progressive broadening of the passbands' width along the RF spectrum. These widths can be approximated by

$$\Delta_n\omega \cong \frac{3.72|\zeta(\omega_n)|^{1/2}}{\sigma_\omega D_{eq}}. \tag{1.52}$$

The width enlargement is due to the factor $|\zeta(\omega)|^{1/2}$, and weakens the suppression or filtering of residual harmonics. Therefore, the output signal contains high frequencies that are manifested in the time domain as the oscillatory structure in the pulse's trailing edge. For future use, we compute here the maximum value of the 30-dB passband half width in the significant part of the spectrum, $\omega \sim 3.72\sigma_\omega$:

$$\Delta\omega_{max} \cong 3.72(1+\epsilon^2)^{1/4}/\sigma_\omega D_{eq}. \tag{1.53}$$

where Eq. (1.44) has been used. Notice that, despite the presence of significant β_3 dispersion, the train of Fig. 1.6 (top) has no intensity fluctuations, broadening or pedestal, the only impairment being the distortion induced by second-order dispersion. If the influence of β_3 is sufficiently large the passbands overlap, causing the fading of the multiple passband structure. The approximation assumed in Eq. (1.49) is no longer valid and it is required to resort to (1.43) for the correct description of the intensity PSD. This is shown at the bottom Fig. 1.6 where β_3 influence is now larger ($\epsilon = 6.41$ rad). Notice that in this regime the output signal shows periodic variations in pulse intensity in addition to pulse distortion. Pulse intensity fluctuations are periodic, and they are due to the underlying non-filtered input harmonics.

1.6 Rejection Properties of Talbot Filters

As has been illustrated in the previous section, the dispersive mechanism of Talbot effect is described in the spectral domain by the passbands $G_n(\omega)$. This filtering is exact only when the dispersion line is adjusted to half-integer compressing Talbot indices $\gamma/\alpha = (2k+1)/2$ and higher-order dispersion is negligible. In any other situation, Talbot filtering is not ideal.

In order to characterize the ability of Talbot filters as harmonic suppressors in the intensity domain, we will center our analysis on the compressing Talbot lines, since non-compressing Talbot lines can be regarded as small deviations from the compressing Talbot ones. This point of view will be explored in the following section.

From Figs. 1.5 or 1.6, the filter structure has $\alpha - 1$ residual frequencies between two output harmonics. These frequencies are filtered by $\gamma - 1$ passbands. In order to measure the rejection efficiency of these passbands, we introduce a dimensionless parameter W. Since the overall bandwidth of the intensity spectrum is of the order of $3.72\sigma_\omega$ and the output harmonics are multiples of $\alpha\Omega_0$, the ratio

$$W = 3.72\sigma_\omega/\alpha\Omega_0 = 2.23\sigma_{\omega\mathrm{FWHM}}/\alpha\Omega_0, \tag{1.54}$$

determines the number of significant harmonics in the output train. In the last part of the formula we have introduced the definition of W in terms of the spectral width measured as a full-width at half maximum (FWHM). If the pulses are gaussian, the relation of both spectral widths is $\sigma_{\omega\mathrm{FWHM}} = 1.665\sigma_\omega$.

Parameter W can also be interpreted as a normalized linewidth, since it is the overall spectral width of the train normalized by the fundamental output frequency. Since the temporal pulse duration goes as $1/\sigma_\omega$, W is also proportional to the number of pulses that can be contained in a period t_0/α of the output train. A parameter of this type, but normalized to the fundamental input harmonic, has been used to describe the harmonic suppression in Talbot dispersive filters [25].

Now, let us consider a general situation like those shown in Figs. 1.5 and 1.6. Let us assume that a given h-th input harmonic is residual, i.e., does not belong to the output train. Let us also consider that this harmonic will be filtered by a certain passband of index n, and set the criterion that residual harmonics with power below -30 dB do not significantly alter the output signal. Thus, condition

$$|\omega_n - h\Omega_0| > \Delta_n\omega, \tag{1.55}$$

guarantees the filtering of residual harmonics. Using Eq. (1.50) and this condition reads:

$$\Omega_0\,|n\alpha - h\gamma| > \gamma\Delta_n\omega, \tag{1.56}$$

the most unfavorable situation being determined by

$$|n\alpha - h\gamma| = 1 \tag{1.57}$$

and the maximum of the right hand side of Eq. (1.56), which is given by Eq. (1.53). Notice that, since γ and α are coprime integers, Eq. (1.57) has always solution for n and h integers according to a corollary of Euclid's first theorem [72]. For instance, in Talbot dispersive filters designed to increase the repetition rate of a pulse train ($\gamma = 1, \alpha > 1$), the general solution of (1.57) is $h = n\alpha \pm 1$ for arbitrary n. Therefore all rejected harmonics lying in the significant portion of the spectrum ($\omega < 3.72\sigma_\omega$) carry an amount of power below -30 dB, if and only if

$$\Omega_0 > \gamma \Delta\omega_{max}. \tag{1.58}$$

This condition can be rewritten as a lower bound K for the value of W:

$$W > K = 2.20(1 + \epsilon^2)^{1/4}. \tag{1.59}$$

Therefore, W controls the quality of the output train in any Talbot filter, which depends on the index through the definition of W, but it is independent of the index γ. Condition (1.59) can be interpreted in the time domain as the absence of overlapping of pulses in the repetition-rate multiplied train. If $W = 2.20$, and the pulses are transform-limited, 99% of the energy of the pulse is contained in the period t_0/α of the multiplied train.

The bound K depends slightly on second-order dispersion. For instance, if $\epsilon \sim \pi$, inequality (1.59) becomes $W > K = 3.99$. This means that at least four output harmonics have to be clearly observed in the intensity spectrum to obtain a satisfactory output train. On the contrary, if second-order dispersion is negligible, $K = 2.20$, and $W = 3$ is sufficient.

In the derivation of Eq. (1.59) either the overlapping between passbands or the influence of the envelope on the passbands' centers has not been taken into account. Hence, this condition does not exactly guarantee that all rejected harmonics carry a power below -30 dB. Despite of this fact, (1.59) works correctly as we will show by means of the examples presented in Figs. 1.5 and 1.6.

In Fig. 1.5, $\epsilon \ll \pi$ so that $K = 2.20$. At the top figure ($W = 2.94$), condition (1.59) is satisfied, and three harmonics can be clearly seen in the significant portion of the intensity spectrum, from DC to 88 GHz. As a result, a train with frequency $3 \times \Omega_0$ is obtained. In the example at the bottom, $W = 1.86$, and the output train suffers from the impairments

commented before.

Fig. 1.6 shows the influence of second-order dispersion. In both examples of this figure $W = 4.41$. At the top figure $K = 4.10$ ($\epsilon = 3.32$), so that condition (1.59) is satisfied. This implies that the output is a satisfactory $3 \times \Omega_0$ train, although the basic period shows pulse distortion induced by second-order dispersion. Notice that this example is in the limit of validity of criterion (1.55), since the fourth harmonic is precisely 30 dB below the carrier. In the example depicted at the bottom ($\epsilon = 6.41$, $K = 5.60$) condition (1.59) is not satisfied, and the temporal signal shows periodic intensity fluctuations.

It is also worth comparing formula (1.59) with the experimental data reported in [24]. There, a series of Talbot dispersive filters based on SMF were used to increase the repetition rate of a 49 GHz train of unchirped non-Gaussian pulses from a mode-locked semiconductor laser diode at 1565.7 nm. The optical spectrum had a FWHM of 379 GHz ($\sim$ 3 nm), which corresponds to $\sigma_\omega = 2\pi \times 228$ GHz in the Gaussian approximation. The Talbot filters had indices 1, 1/2, 1/3 and 1/4, so that $W = 17.28$, 8.64, 5.76 and 4.32, all these values being over the bound (1.59). Despite the non-Gaussian character of the spectrum, stable trains of pulses with low amplitude fluctuations and no pulse distortion were obtained, as was expected from the quoted values of W.

1.7 Stability of Talbot Filters

By stability of the Talbot filters we mean the ability of a dispersive line to create an intensity train with increased repetition-rate frequency under slight dispersion variations from compressing Talbot condition. Compressing conditions will be considered as the ideal operation of the filter, since the harmonics of the output train lie in the center of the passbands. Standard Talbot conditions, Eq. (1.47), can be considered as a length deviation $\delta L = C/\sigma_\omega^2 \beta_2$ from the compressing condition (1.48). We will analyze the performance of the filters under variations of the fiber length and the period of the input train.

First, timing variations can be reduced to length variations. Let us suppose that the frequency of the input train differs by a small quantity from the value used to determine the fiber length of the Talbot device. At first order it can be interpreted as a deviation of the fiber length, since from Eq. (1.48), $\delta L/L = 2\delta\Omega_0/\Omega_0$, so that a relative change in the frequency of the train is equivalent to a double relative change in fiber length. Therefore,

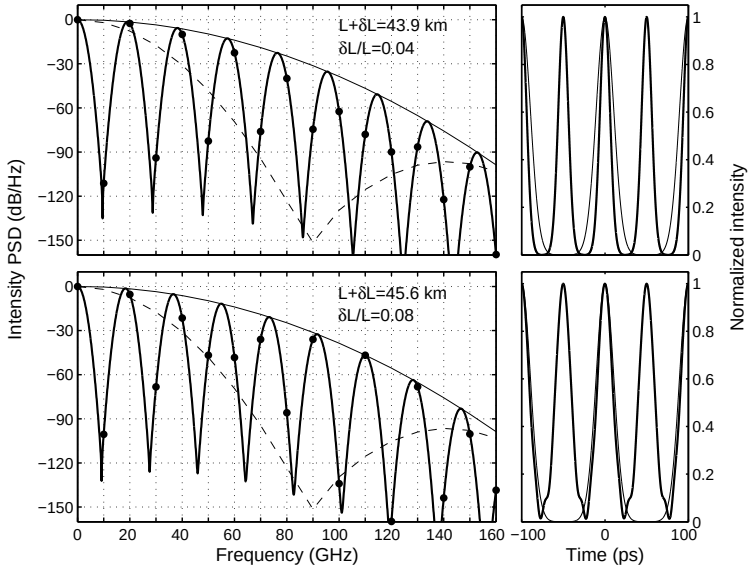

Figure 1.7: *Intensity PSD (left) and temporal intensity (right) of a 10-GHz train after its propagation in a standard SMF of length 43.9 km (top) and 45.6 km (bottom), which correspond to length deviations of the compressing Talbot condition with indices* $\gamma/\alpha = 1/2$. *The relative length deviations are 4% and 8%, respectively.*

Talbot filters are two times more sensitive to timing variations than to length variations.

Let us then consider arbitrary length variations δL. The result of this variation in the propagation of a train can be interpreted in two steps. The pulses of the input train are first dispersed individually under the accumulated dispersion $\beta_2 \delta L$, and then the filter acts ideally over the train of dispersed pulses. Therefore, the main spectral trace of a length variation of a compressing Talbot filter is the decrease of the RF bandwidth. However, length variations also affect the rejection properties of the dispersive filter.

These two features can be observed in the examples presented in Fig. 1.7, where the temporal signal and its intensity spectrum are depicted after the propagation along a standard SMF whose length has been enlarged 4% (top) and 8% (bottom) from the compressing condition with index $\gamma/\alpha = 1/2$. Pulses have a width of 15 ps and chirp $C = 2$ rad. The

second-order dispersion is negligible in both cases: $\epsilon = 0.035$ rad (top) and $\epsilon = 0.036$ rad (bottom). The significant spectrum ranges from DC to 88 GHz.

In the first example, above, the output signal can be entirely interpreted as a train of slightly dispersed pulses. In the second one, the additional broadening produces pulse-to-pulse interference and thus intensity fluctuations, observed as an increase in the power contained in the residual harmonics. Our tolerance analysis is precisely devoted to quantify the allowed changes in accumulated dispersion so that the interpretation of the output intensity as a train of non-overlapping but slightly dispersed pulses is not missed.

From the spectral point of view length or timing variations imply a deviation of the centers of the passbands $\delta\omega_n$ and a small change in their widths $\delta\Delta_n\omega$. These variations are, respectively,

$$\delta\omega_n/\omega_n = \delta\Delta_n\omega/\Delta_n\omega = -\delta L/L, \tag{1.60}$$

see (1.48), (1.50) and (1.51). First, let us consider the deviations in the spectral power of output harmonics, as shown in the first example of Fig. 1.7. The highest significant output harmonic ($\omega_n \cong 3.72\sigma_\omega$) suffers the most noticeable decrease in power due to pulse broadening. This harmonic has an index $n \cong \gamma W$, so that its power does not fade more than 30 dB if:

$$|\delta\omega_n| < \Delta\omega_n - |\delta\Delta_n\omega|. \tag{1.61}$$

This condition guarantees that the power of significant output harmonics follows a decreasing curve corresponding to a train of broader pulses. Using (1.48), (1.60), (1.51) and the definition of W, condition (1.61) can be rewritten as:

$$\frac{|\delta L|}{L} < \frac{K}{\alpha\gamma W^2 + K}. \tag{1.62}$$

This tolerance criterion essentially coincides with the bound (64) in Ref. [20], which was derived by considering the optical spectral phases induced by dispersion deviations.

On the other hand, it will be necessary to assure that the power of all residual harmonics remains below -30 dB with respect to the carrier. This guarantees that, in the significant portion of the spectrum, the power of output harmonics is always larger than that of residual harmonics. This condition reads:

$$|\omega_n - h\Omega_0| - |\delta\omega_n| > \Delta_n\omega + |\delta\Delta_n\omega|. \tag{1.63}$$

This equation is a generalization of formula (1.55). Following the same steps as in the previous section we obtain:

$$\frac{|\delta L|}{L} < \frac{W - K}{\alpha\gamma W^2 + K}. \tag{1.64}$$

Together, bounds (1.62) and (1.64) determine the tolerance region where length variations induce an intensity train that can be interpreted, on one hand, as a train composed of slightly broadened pulses and, on the other, without significant intensity fluctuations.

Bounds (1.62) and (1.64) decrease as the spectral width increases [20, 24, 25]. Since parameter W controls the spectral purity of the output train, quality of the output and stability of the filter play opposite roles. To reach a compromise between quality and stability, we depict in Fig. 1.8 these bounds as a function of W for $\gamma/\alpha = 1/2$. The dotted curve is bound (1.62), whereas the dashed curve is bound (1.64). The continuous curve represents the minimum of both curves. Below, the same minimum curves are depicted for different values of γ/α. Negligible second-order dispersion has been assumed ($K = 2.20$).

Bound (1.62) dominates at high W, so that the power of output harmonics is very sensitive to length deviations when the filter consists of narrow passbands, or operates with narrow pulses with high spectral width. This is because narrow pulses may disperse considerably under small dispersion deviations. For small values of W, bound (1.64) dominates. In this regime the efficiency of the filter is poor, since broad passbands or broad pulses allow residual harmonics to carry significant power. In other words, a certain amount of pulse interference is already present in the output in absence of length variations as a nearly significant residual spectral power. Broader pulses do not disperse considerably under dispersion deviations, but slight pulse interference augments the residual harmonic content. Therefore, the tolerance is dominated by the growth of residual harmonics.

Optimal tolerance is reached in the intersection point of both bounds:

$$W_{opt} = 2K. \tag{1.65}$$

This value verifies condition (1.59) and maximizes the stability of the Talbot line with a given index. Notice that the dependence on higher-order dispersion is implicit in K. This is the proposed design criterion of the

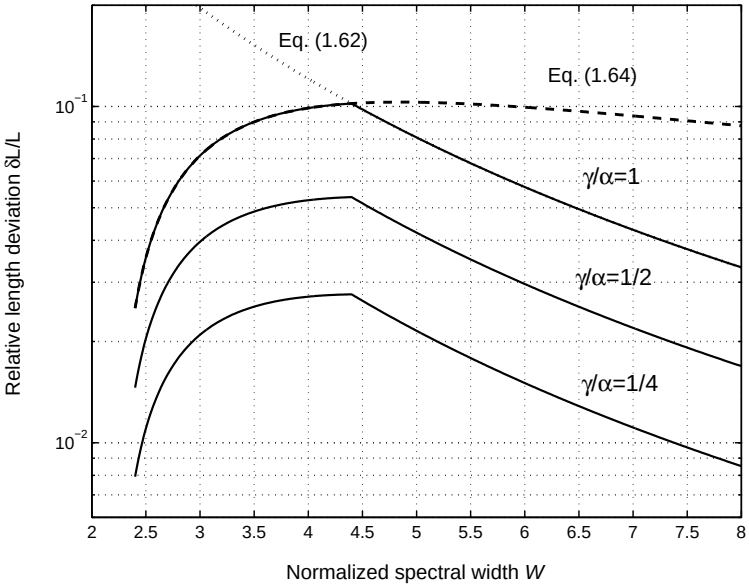

Figure 1.8: *Relative length deviation allowed by the bounds (1.62) and (1.64) with respect to the normalized spectral width W for different Talbot filters with negligible second-order dispersion.*

dispersive filter. Using the definition of W, and assuming negligible second-order dispersion, optimal tolerance condition (1.65) can be rephrased in terms of the spectral width of the input train. When it is measured as the FWHM, optimal conditions require that the FWHM is twice the repetition-rate frequency of the output train, $2\alpha\Omega_0$. From the temporal point of view, and assuming transform-limited pulses, this condition states that 99% of the energy of a pulse is contained in half a period of the multiplied train, $t_0/2\alpha$. The optimal value of tolerance is then:

$$\frac{|\delta L|}{L} < \frac{1}{K(4\alpha\gamma+1)} \cong \frac{0.10}{\alpha\gamma(1+\epsilon^2)^{1/4}}. \tag{1.66}$$

Notice that it is inversely proportional to the product $\gamma\alpha$ and, therefore, to the complexity of the filter. When we consider the usual fractional Talbot filters of the series $\gamma/\alpha = 1/\alpha$, Eq. (1.66) states that the expected optimal tolerance in length is about 10% divided by the repetition-rate factor α. For instance, in the examples in Fig. 1.8, $W = 4.4$, and the tolerance in length given by (1.66) is 5%. Notice finally from Fig. 1.8 that optimal tolerance

(1.66) is located at the edge of a plateau. Nearly optimal tolerances can be obtained in its neighborhood.

1.8 Conclusions

In this chapter we have briefly reviewed the well-known space-time duality which is based on the mathematical equivalence between equations describing one-dimensional paraxial diffraction and pulse propagation in a linear first-order dispersive medium with negligible attenuation. Under this analogy, the pulse envelope is equivalent to the complex amplitude distribution of light in diffractive optics. In this context, we have presented the temporal counterpart of the self-imaging or Talbot effect. We have analyzed, in terms of intensity, an arbitrary train of pulses after propagation through a dispersive medium under Talbot condition. For integer Talbot devices the output intensity is a replica of the input train, whereas for fractional Talbot lines an intensity train with higher repetition rate is obtained provided that input pulses are sufficiently narrow to avoid overlapping. In both cases the output intensity is shifted by half a period depending on the parity of Talbot index.

Talbot devices are also analyzed from the spectral point of view. This study is based on the computation of the exact intensity PSD of a coherent train of pulses after its propagation in a dispersive medium with arbitrary first and second order dispersion and negligible attenuation. We have considered trains composed with linearly chirped Gaussian pulses. These analytical results enable the identification of the spectral components that represent the dispersion of individual pulses, as well as the terms where the interference between pulses is enclosed. In this way we have made connection with the existing results in the literature [63, 65–67]. From the spectral point of view, Talbot dispersive lines can be interpreted as a multiple bandpass filter where each passband corresponds to the interference between pulses originally separated a number of times slots. The filter essentially rejects the intensity harmonics of the input train that do not belong to the output. The rejection is exact only in semi-integer Talbot filters, with negligible higher-order dispersion, and transform-limited pulses, since in this case the filter is adjusted to the dispersion of carrier suppression [71]. The filter is not static, but depends on the spectral width of the input train and the dispersive characteristics of the line. In particular, conditions have been derived that guarantee that the Talbot filter provides output intensity trains with negligible intensity fluctuations,

even in the presence of higher-order dispersion. In these cases, however, the pulses may present distortion. The derived condition, Eq. (1.59), essentially states that the pulses of the output train do not overlap. Finally, the stability under timing and length variations of the Talbot line has been analyzed. We have shown the properties of the two regimes of operation of Talbot filters, described by two bounds, Eqs. (1.62) and (1.64). When the spectral width of the train is large, dispersion instabilities tend to broaden the pulses and the filter's performance worsens by pulse-to-pulse interference. In contrast, when the spectral width is moderate, dispersion variations decrease the rejection ability of the filter. Optimal stability is reached when the spectral width of the input train, measured as FWHM, equals twice the repetition-rate frequency of the output train. The expected length tolerances are about 10% divided by the repetition-rate factor .

Chapter 2

Non-ideal coherent Temporal Talbot effect

2.1 Introduction

As has been shown in the previous chapter, the Talbot effect is caused by the interference between all diffracted orders of a grating in space domain and by the multiple interference among all pulses of a train in its temporal counterpart. It means that all diffraction orders or all dispersed pulses get involved in the reconstruction of each unit cell or pulse of the resulting Talbot image. In this sense, it is a collective phenomenon, since the pattern is a consequence of the whole periodic structure of the grating or of the train of pulses. It is expected from a collective phenomenon like this some kind of stability under small variation of the parameters defining the cells of the periodic structure. In diffractive optics, several works have reported on Talbot effect as a method to smooth imperfections of a grating, such as the absence of a unit cell, or localized modifications of the basic period [21, 73]. The degradation of the effect due to the finite orders from the optical axis is also known [22]. This walk-off effect progressively reduces the paraxial region where Talbot effect takes place. In the temporal domain the study of the degradation by the finite width of pulse trains has reported in ref [74]

The aim of this chapter is to describe the tolerance of Talbot devices against train imperfections. Unlike the works previously cited, our approach to the problem is not deterministic but stochastic. Although the presented analysis is valid in both diffractive and dispersive domain, we will describe it from the temporal point of view. Among all possible deviation of the ideal periodic signal, we will treat first the randomly on-

off keyed pulses in the train and later the jittery pulses in the train. In both cases Talbot devices are shown to have filtering properties around frequencies of the order of the repetition rate of the train. The use of this property is then limited to broadband noise reduction.

This chapter is split into two large sections. Section 2.2 is devoted to the analysis of a randomly distributed pulses after a Talbot device. This study is carried out in the Fourier domain by means of the power spectrum density, in the same way as the analysis of exact Talbot effect in the previous chapter. By assuming linearly chirped Gaussian pulses together with the independence of the variables which determine the presence or absence of a pulse in the train, an exact stochastic result of the RF-spectrum is achieved. The noise spectral after Talbot device consists of a set of passbands, each one being cosine-squared modulated. The centers of the passbands are shifted depending on the value of the chirp. This fact, allows an indirect characterization of the pulse in the train through the analysis of the spectrum. In particular, measurements of the positions and the width of the bandpass results in the determination of the chirp of the initial pulses. Moreover, the resulting noise spectral varies continuously with respect to the parameters that define the model. It means that, in order to observe the spectral features of noise, no fine tuning of the initial repetition rate of the train is necessary to match the Talbot conditions, in contrast with the temporal domain where the trace of the Talbot effect is the increase of the repetition rate of the train. However, for clarity, all results are derived under exact Talbot conditions.

Section 2.3 deals with the behavior of Talbot devices when they are fed with a train suffering from timing jitter. Despite the fact we have centered our study in timing jitter, the formalism we present can be easily expanded to amplitude jitter of a combination of them [78]. Firstly, we approach the problem in time domain by means of the variance, in subsection 2.3.1. Analytical expressions for the input and output variance are reported, showing that the variance of the original train is flatted after passing a Talbot device. The presence of pedestal in the output train is also studied. In subsection 2.3.2 we analyzed the intensity spectrum of the jittery trains before and after the propagation of the train through the Talbot filter. This spectral analysis is more general than the previous one in terms of variance, since correlations between variables describing timing jitter are now allowed. The results presented here are not exact but rely on a small-signal approximation of jitter source. This technique has been widely applied in the analysis of the RF intensity spectrum of timing jitter noise

in mode-locked lasers [75–78]. The results are exemplified for two models of jitter pulse correlation, one describing the noise of fundamentally mode-locked lasers and the other one describing harmonically mode-locked lasers. In subsection 2.3.3 we numerically investigate the conditions for a decrease in the noise power around the harmonics. Finally, we end the chapter presenting our conclusions.

2.2 Talbot imaging of On-Off-Keyed trains

In this section we analyze the behavior of Talbot filters when they are fed with a coherent train composed by randomly distributed pulses. The optical envelope which will be launched in the Talbot line can be expressed as,

$$a(t,0) = \sum_k b_k f(t - kt_0) \tag{2.1}$$

where $f(t)$ denotes the pulse form, t_0 is the unit interval of the train, and the symbols b_k are a set of random variables which will be assumed uncorrelated. These variables describe the presence ($b_k = 1$) or absence ($b_k = 0$) of pulses in the train with probability p and $1 - p$ respectively. Under ideal conditions all pulses are present ($p = 1$) so that the train is t_0-periodic. The average over all realizations will be denoted by brackets $\langle \cdots \rangle$, so $\langle b_k \rangle = p$ and its standard deviation $\langle b_k^2 \rangle = \sigma_b^2 = p\ (1 - p)$. Unless otherwise stated all sums and integrals runs from $-\infty$ to $+\infty$. For simplicity the pulse form is assumed to be linearly chirped Gaussian:

$$f(t) = \exp[-t^2(1 - iC)/2t_p^2] \tag{2.2}$$

The parameter t_p is the rms width of every pulse and C is the linear chirp or phase modulation. In order to avoid overlapping between incoming pulses and also to allow repetition rate multiplication at the output of the Talbot device, we assume that the pulse width is smaller than the unit interval $t_p < t_0$

If the randomly train of pulses, Eq. (2.1), is propagated along a fist-order guided dispersive medium with negligible attenuation, Eq. (1.16), the optical envelope results in a coherent superposition of dispersed pulses.

$$a(t,\xi) = \left[\frac{t_p^2}{\rho(1 - iC)}\right]^{1/2} \sum_k b_k \exp\left[\frac{-(t - kt_0)^2(1 - iC)}{2\rho}\right]. \tag{2.3}$$

where

$$\rho = 1/\sigma_\omega^2 + i\xi + iC/\sigma_\omega^2, \tag{2.4}$$

$\sigma_\omega = (1 + C^2)^{1/2}/t_p$ is the linewidth of the incoming pulses and the parameter ξ accounts for the accumulated dispersion in the medium. This is the relevant parameter of the propagation medium. If the guided medium is chosen a fiber, $\xi = \beta_2 L$, L being the fiber length; whereas for a linearly chirped fiber grating $\xi = \ddot{\Phi}$, $\ddot{\Phi}$ being the slope of the LCFG response in reflection mode around the carrier frequency ω_0. This slope is designed to be constant within the bandwidth of the input signal. In this way, the study will be presented here, is manifestly independent on the high dispersive medium used as Talbot device.

The dispersed train, Eq. (2.3), can equivalently be expressed in the Fourier domain, as follows

$$A(\omega, \xi) = t_p \left[\frac{2\pi}{1 - iC}\right]^{1/2} \exp(-\rho\omega^2/2) \sum_k b_k \exp(-i\omega k t_0), \tag{2.5}$$

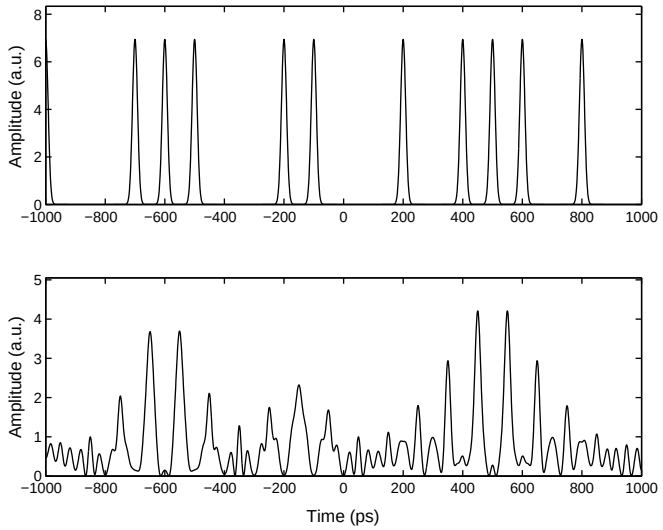

Figure 2.1: *Simulation of the form of the pulse envelope of 20-unit intervals of a 10-GHz, p=0.5 random train of unchirped, 12-ps rms Gaussian pulses before (above) and after (below) its pass through a Talbot device with* $\gamma/\alpha = 1$.

In Fig. 2.1, we present a simulation of the dispersion of a portion of a 10-GHz train ($t_0 = 100$ ps) randomly on-off keyed, after its pass through the first integer Talbot device, $\gamma/\alpha = 1$. The total dispersion of the device is $\xi = +1592$ ps^2/rad. The probability of appearance of pulses in the train is $p = 0.5$. Pulses are unchirped and have a rms width of 12 ps. The ideal Talbot would reproduce the incoming train shifted by half a unit interval. The temporal spreading of pulses due to dispersion creates Talbot images formed by interference of pulses. This phenomenon is local, depending on the number of neighboring pulses around a given time slot. This leads to an unsatisfactory temporal signal, since the temporal characteristics of the output train depend on the local behavior of the input. Nevertheless, wherever two pulses interfere in Fig. 2.1, they tend to form the desired ideal output train. Then, a spectral analysis of the signal can unveil the ability of the Talbot device to reconstruct output harmonics in a non-ideal situation.

2.2.1 Intensity Spectrum

As has been shown in previous chapter, dispersive lines leave the power spectrum of the optical envelope, $|A(\omega,\xi)|^2$, invariant. However, since detection is a non linear transformation of the stochastic variables, $a(t,\xi)$ or $A(\omega,\xi)$, the pulse spreading caused by the dispersion-induced phases, can be observed in the detected train.

The power spectrum of the detected train $i(t,\xi) = |a(t,\xi)|^2$, is computed by Fourier transforming the mean correlator, which is the temporal average of the correlator [79]:

$$S(\omega,\xi) = \int_{-\infty}^{+\infty} d\tau \ \exp(-i\omega\tau) \ \left[\lim_{T\to\infty} \frac{1}{2T} \int_{-T}^{T} dt \ \langle i(t+\tau,\xi) i(t,\xi)\rangle\right], \quad (2.6)$$

where the photocurrent correlator is

$$\begin{aligned}\langle i(t,\xi) i(t',\xi)\rangle = \int_{-\infty}^{+\infty}\int_{-\infty}^{+\infty} \frac{d\omega_1}{2\pi}\frac{d\omega_2}{2\pi} \exp[i(\omega_1 t - \omega_2 t')] \\ \times \langle I(\omega_1,\xi) I(\omega_2,\xi)^*\rangle.\end{aligned} \quad (2.7)$$

The Fourier form of the photocurrent $I(\omega,\xi)$, is related to the Fourier form of the optical envelope $A(\omega,\xi)$ by an autocorrelation,

$$\begin{aligned} I(\omega,\xi) = \int_{-\infty}^{+\infty} dt \exp(-i\omega t) i(t,\xi) = \\ \int_{-\infty}^{+\infty} \frac{d\omega'}{2\pi} A(\omega+\omega',\xi) A(\omega',\xi)^*. \end{aligned} \tag{2.8}$$

Then, using Eq. (2.5), the Fourier form of the photocurrent can be expressed as

$$I(\omega,\xi) = J(\omega) \sum_k B_k(\omega) \exp(-i\omega k t_0), \tag{2.9}$$

where

$$J(\omega) = t_p \sqrt{\pi} \exp(-\omega^2/4\sigma_\omega^2), \tag{2.10}$$

$$B_k(\omega) = b_k \sum_s b_{k+s}\ g_s(\omega) \exp(-i\omega s t_0/2) \tag{2.11}$$

and

$$g_s(\omega) = \exp\left[-\frac{\sigma_\omega^2}{4}\left(\xi\omega + C\omega/\sigma_\omega^2 - s t_0\right)^2\right]. \tag{2.12}$$

To compute the power spectral density, Eq. (2.6), let us suppose that the expected value at different frequencies of the correlator of functions $B_k(\omega)$ is of the form

$$\begin{aligned} \langle B_k(\omega_1) B_m(\omega_2)^* \rangle = & \langle B_k(\omega_1) \rangle \langle B_m(\omega_2)^* \rangle \\ & + \delta_{km} \Omega(\omega_1,\omega_2) + \Delta_{k-m}(\omega_1,\omega_2), \end{aligned} \tag{2.13}$$

where δ_{km} is the Kronecker delta, the asterisk denotes complex conjugation, and $\Omega(\omega_1,\omega_2)$ and $\Delta_{k-m}(\omega_1,\omega_2)$ are adimensional functions to be evaluated a posteriori. The first term in Eq. (2.13), $\langle B_k(\omega_1)\rangle\langle B_m(\omega_2)^*\rangle$ gives rise to the intensity spectrum of the signal which is composed of a set of harmonics multiples of the fundamental frequency Ω_0. The behavior of the signal power spectrum has already been analyzed in detail in the previous chapter, so here we will focus in the noise spectral density. The second and third terms in Eq. (2.13) originate the noise contribution to the microwave spectrum, resulting in

$$t_0 S^{(N)}(\omega,\xi) = |J(\omega)|^2 \left[\Omega(\omega,\omega) + \sum_s \Delta_s(\omega,\omega)\exp(i\omega s t_0)\right]. \qquad (2.14)$$

where Eqs. (2.6)-(2.12) have been used. Therefore only the diagonal values, $\omega_1 = \omega_2 = \omega$, of the functions Ω and Δ_s are relevant. These adimensional functions can be computed from Eq. (2.11), using the following identity for the expected value of four-bit variables:

$$\begin{aligned}\langle b_i b_j b_k b_l\rangle =& p^4 + p^2\sigma_b^2\left(\delta_{ij}+\delta_{ik}+\delta_{il}+\delta_{jk}+\delta_{jl}+\delta kl\right)\\ &+ \sigma_b^2 a(p)\left(\delta_{ij}\delta_{jk}+\delta_{ij}\delta_{jl}+\delta_{ik}\delta_{kl}+\delta_{jk}\delta_{kl}\right)\\ &+ \sigma_b^4\left(\delta_{ij}\delta_{kl}+\delta_{ik}\delta_{jl}+\delta_{il}\delta_{jk}\right)+\sigma_b^2 b(p)\delta_{ij}\delta_{jk}\delta_{kl},\end{aligned} \qquad (2.15)$$

with $a(p) = p(1-2p)$ and $b(p) = 1-6p+6p^2$. To check this formula, it suffices to consider all the different combinations of indices in both sides of the equality. Using Eq. (2.15), and after some algebra, the computation of the functions Ω and Δ_s yields

$$\Omega(\omega,\omega) = \sigma_b^2\left[p^2|Z|^2 + 2ag_0(\omega)Re(Z) + \sigma_b^2\sum_s g_s^2(\omega) + bg_0^2(\omega)\right] \qquad (2.16)$$

and

$$\sum_s \Delta_s(\omega,\omega)\exp(-i\omega s t_0) = \qquad (2.17)$$

$$\sigma_b^2\left[p^2(Z^2+|Z|^2+Z^{*2}) + 2ag_0(\omega)Re(Z) + \sigma_b^2\sum_s g_s(\omega)g_{-s}(\omega)\right]$$

where $Z(\omega) = \sum_s g_s(\omega)\exp(-i\omega s t_0/2)$, and Re stands for the real part. Finally, the power spectrum is

$$\begin{aligned}t_0 S^{(N)}(\omega,\xi) =& \sigma_b^2|J(\omega)|^2\Bigg\{\left[g_0(\omega) + 2p\sum_{s>0}\left(g_s(\omega)+g_{-s}(\omega)\right)\cos(\omega s t_0/2)\right]^2\\ &+ \sigma_b^2\sum_{s>0}\left[g_s(\omega)+g_{-s}(\omega)\right]^2\Bigg\}.\end{aligned} \qquad (2.18)$$

This formula contains the relevant filtering features of the random Talbot effect after detection. The intensity spectrum consists of a broadband function, $|J(\omega)|^2$ multiplied by the term in parenthesis, which is a cumbersome combination of narrower functions, $g_s(\omega)$. Then, $|J(\omega)|^2$ determines the bandwidth of the microwave spectrum, which measured as the half-width of 30-dB decay in power, is 3.72 σ_ω. Therefore, the maximum frequency involved in Eq. (2.18) will be $\omega_{\max} \sim 3.72\ \sigma_\omega$.

Before approaching the analysis of the intensity spectrum after a Talbot device we derive the power spectral density of the input train, $S^{(N)}(\omega, 0)$, by setting $\xi = 0$ in Eq. (2.18). The gaussian functions g_s have now the shape

$$g_s(\omega)|_{\xi=0} = \exp\left[-\frac{C^2}{4\sigma_\omega^2}\left(\omega - s\frac{\sigma_\omega^2 t_0}{C}\right)^2\right]. \tag{2.19}$$

They are centered at frequencies $\omega = s\sigma_\omega^2 t_0/C$. Since $\sigma_\omega t_0/|C| \sim t_0/t_p > 1$, and the maximum frequency involved in Eq. (2.18) is $\omega_{\max} \sim 3.72\ \sigma_\omega$, the functions g_s with index $s \neq 0$ lies out of the pulse spectrum. Therefore we neglect all the contributions g_s except that with index $s = 0$. In this conditions the noise power spectrum is given by

$$t_0 S(\omega, 0) \cong \sigma_b^2 |F(\omega)|^2 \tag{2.20}$$

where $|F(\omega)|^2 = t_p^2 \pi \exp(-t_p^2\omega^2/2)$ is the Fourier transform of a single detected pulse, $|f(t)|^2$. Notice that, Eq. (2.20) tallies with the noise spectrum of a train of independent random pulses of the form $\sum_k b_k |f(t - kt_0)|^2$. This means that neglecting the contribution of the functions $g_s(\omega)$ is equivalent to neglecting the overlapping between incoming pulses. This is a direct consequence of the analysis presented in chapter 1, where it has been shown that functions $g_s(\omega)$ represent the interference between pulses separated s time slots in the train.

Now we proceed to the analysis of the intensity spectrum after a Talbot device. From Eq. (2.12), the separation between maxima of two consecutive Gaussian functions g_s and g_{s+1} is approximately $t_0/|\xi|$, and their width is $t_p/|\xi|$. Under Talbot conditions the $|\xi| \approx t_0^2 \gg t_p^2$, so that the overlapping between these narrowband functions can be neglected, $g_s g_r = g_s^2 \delta_{sr}$. With this approximation the noise power spectrum is notably simplified:

$$t_0 S^{(N)}(\omega,\xi) \cong \sigma_b^2 |J(\omega)|^2 \left[G_0(\omega) + \sum_{s\neq 0} M_n(\omega) G_s(\omega) \right], \tag{2.21}$$

where

$$M_n(\omega) = 4p^2 \cos^2(\omega s t_0/2) + \sigma_b^2, \tag{2.22}$$

and $G_s(\omega) = g_s(\omega)^2$. The noise spectral density after a high dispersion line has a structure similar to that determining the value of the harmonics of the intensity of an ideal train (see Eq. (1.49) in chapter 1). The PSD is again determined by a broadband function $J(\omega)$ multiplied by the sum of narrowband functions, $G_n(\omega)$, but in this case the passbands appear modulated by $M(\omega)$. When the initial pulses are unchirped, this broadband output noise-envelope function $|J(\omega)|^2$ is just the power spectrum of a single detected pulse, $|F(\omega)|^2$, but for chirped pulses, the spectrum enhances its bandwidth. This enlargement is the same as the optical linewidth enhancement of the individual Gaussian pulses due to chirp, but here it appears as the noise envelope of the microwave power spectrum of the detected random train after the Talbot device.

The output noise spectral density, Eq. (2.18) or (2.21), depends therefore on all the parameters that describe the train: the probability of appearance of pulses (through p and σ_b^2), the parameters of the individual pulses (t_p and C), and the period of the train (t_0). On the contrary, the detection of the train before entering the dispersive device depends only on σ_b^2 and t_p . Notice that the dependence of the spectral content of $S^{(N)}(\omega,\xi)$ in Eqs. (2.18) and (2.21) with respect to the parameters that define the model varies continuously with the values of these parameters. In the next sections, we analyze the features of $S^{(N)}(\omega,\xi)$ in different regimes of the parameters.

2.2.2 Analysis of the Passbands

The first term of $S^{(N)}(\omega,\xi)$ in the sum in brackets in Eq. (2.21) is $G_0(\omega)$. This function is non-negligible only for frequencies around DC component in the microwave spectrum. The second term has a peaked structure due to the presence of a series of functions $G_s(\omega)$, each of them cosine-squared modulated by the factor $M_n(\omega) = 4p^2 \cos^2(\omega s t_0/2) + \sigma_b^2$. In this section, we consider a situation where variations in $G_s(\omega)$ dominate over the cosine modulation, so that this modulation can be approximated by a constant.

Conditions for this limit are derived below. In our analysis on this limit, both the broadband output noise-envelope function $|J(\omega)|^2$ and the cosine modulation are assumed constant in the vicinity of the maxima of $G_s(\omega)$, yielding a local white-noise background. The basic property of the resulting spectrum is the fact that the broadband noise envelope $\sigma_b^2|J(\omega)|^2$ is filtered around each of the maxima of the functions $G_s(\omega)$, which will be referred to as passband functions.

First we consider trains composed of unchirped pulses $C = 0$, so that the broadband input noise coincides with the broadband envelope in Eq. (2.21), $\sigma_b^2|J(\omega)|^2 = \sigma_b^2|F(\omega)|^2$. This broadband input noise is filtered by the set of the passbands $G_s(\omega)$, which are centered at $\omega = st_0/|\xi| = s\alpha\Omega_0/\gamma$, where the integer s is the passband index. Notice that these passbands functions tally with those shown in chapter 1, where the intensity spectrum of an ideal train of Gaussian pulses was analyzed. Again, when the passband index is a multiple of γ, $s = h\gamma$ for a certain integer h, the surviving frequency is a harmonic of the output train, h being the harmonic index. Between two consecutive output harmonics, there are $\gamma - 1$ different noise passbands. Thus noise becomes narrowband around the harmonics and in definite locations between them. The 10-dB decay full width of these passband functions can be computed from the expression of $G_i(\omega)$, yielding a constant value for all the passbands, $\Delta_W\omega = 4.3\ \alpha\Omega_0 t_p/\gamma t_0$. Thus the passbands are narrower as the pulses are shorter and the dispersion is larger. Moreover, since the separation between consecutive passbands is also proportional to $\alpha\Omega_0/\gamma$, the passband functions depend continuously on dispersion or Talbot index γ/α, much like the creases of an accordion. When dispersion is small, the accordion is open, so that passbands are wider and more distant, and when dispersion is large, the accordion is closed, so that the passbands are closer and their widths are smaller.

The peak value of noise in the top of these passband functions, $G_n(\omega)$, is determined by the input noise envelope, $\sigma_p^2|J(\omega)|^2 = \sigma_p^2|F(\omega)|^2$, and the modulation function, $M_n(\omega)$. Since passbands are centered at frequencies $\omega = n\alpha\Omega_0/\gamma$, the modulation of passbands achieves its maximum value $4p^2 + \sigma_b^2 = p(1 + 3p)$ only for those passbands following harmonics of the output train. Therefore, the peaks of passband functions with index $n = h\gamma$, are raised above or lower below the input noise envelope, depending on the pulse presence probability p. The transition occurs for $p = 0.434$. For instance, for $p = 0.5$, the peak noise level in the top of the passbands is raised 1 dB. Notice that both the passband location and its width depend only on the dispersion of the device and the properties of the basic pulses,

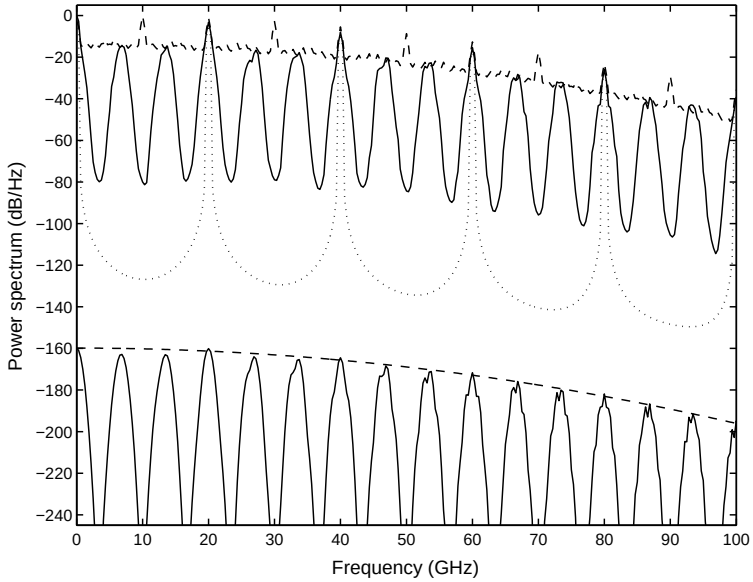

Figure 2.2: *Power spectrum of a detected 10-GHz, p=0.5 random train of unchirped pulses with 6.5-ps rms width after its pass through a Talbot filter width* $\gamma/\alpha = 3/2$. *The upper part of the plot shows (continuous curve) the power spectrum of the detected output train, (dashed curve) the power spectrum of the detected input train, and (dotted curve) the mean signal power spectrum of the output train. The lower part shows analytical approximations to the noise power spectrum: (continuous curve) output noise; (dashed curve) input noise*

but the peak noise raising or lowering depends only on the parameter p.

This situation is illustrated in Fig. 2.2. We simulate a train of 300 pulses randomly distributed with $p = 0.5$. The pulse width is $t_p = 6.5$ ps, its chirp $C = 0$, and the frequency of the train is 10 GHz. The Talbot index is chosen as $\gamma/\alpha = 3/2$, corresponding to a total dispersion of $+2387$ ps^2/rad. The exact Talbot replica would consist of a 20-GHz train. In the upper part of the plot, we present the input spectrum as a dashed curve and the output spectrum as a continuous curve. We also plot with dots the mean signal spectrum, consisting of a set of delta functions in the output harmonics. The finite width of these deltas is due to the finite dimensions of the simulated train. This part of the plot is normalized so that the peak value of the spectrum is 0 dB, and it allows visualization of the noise part

of the spectral density. Below −160 dB, we present our approximation for the noise spectrum density, again with a dashed curve for the input train and with a continuous curve for the output train.

In Fig. 2.2, we observe that all passbands have the same width, $\Delta_W(\omega) = 1.83$ GHz. Noise survives around output harmonics and around multiples of 6.6 and 13.3 GHz. The raising of the peak noise level of the passbands above the input noise level is, according to the above computation, 1 dB for $p = 0.5$. This value is imperceptible with the scales chosen in the figure. Finally, a certain small modulation can be observed in the higher passbands in the right part of the plot. The modulation is also present for low passbands not corresponding to output harmonics. For instance, the peak value in the 6.6-GHz passband is lowered with respect to the input noise due to nonmaximal modulation, i.e., the cosine-squared term maximum does not coincide with the top value of the passband. The analysis of the modulation is treated in the next section.

Now we analyze the chirped case. The first difference is a shift in the centers of the passbands. From Eq. (2.12), they are located at

$$\begin{aligned} \omega =& \frac{st_0}{|\xi + C/\sigma_\omega^2|} \cong \Omega_0 \frac{s\alpha}{\gamma} \left[1 - \frac{1}{2\pi} \mathrm{sign}(\xi) C \frac{\alpha}{\gamma} \frac{\Omega_0^2}{\sigma_\omega^2}\right] \\ &= \Omega_0 \frac{s\alpha}{\gamma} + \Delta_{\mathrm{peak}}^{(s)} \omega, \end{aligned} \tag{2.23}$$

where s in an arbitrary integer. Thus noise survives in the vicinity of multiples of a basic frequency. In the approximation of Eq. (2.23), we use again that the dispersion scale determined by $|\xi|$ is larger than $t_p^2 \sim 1/\sigma_\omega^2$, so that the denominator is $|\xi + C/\sigma_\omega^2| = \mathrm{sign}(\xi)[\xi + C/\sigma_\omega^2]$. The centers of the passbands are shifted depending on the relative sign of chirp and dispersion. For instance, in positive-dispersion devices ($\xi > 0$), the center is redshifted (blueshifted) if the chirp is positive (negative). This shift is maximum when $C = \pm 1$ and represents a relative deviation of $\pi\alpha t_p^2/\gamma t_0^2$ with respect to the center of the unchirped value. The chirp-induced shift is therefore proportional to the value of the frequency in the passband center. In the last part of formula (2.23), we introduce the shift of the s passband, $\Delta_{\mathrm{peak}}^{(s)}\omega$, used below.

The width of the passbands depends also on the chirp. From the form of the Gaussian functions $g_i(\omega)$, Eq. (2.12), it is easy to show that the 10-dB-decay full width decreases with the chirp parameter. The exact full width is

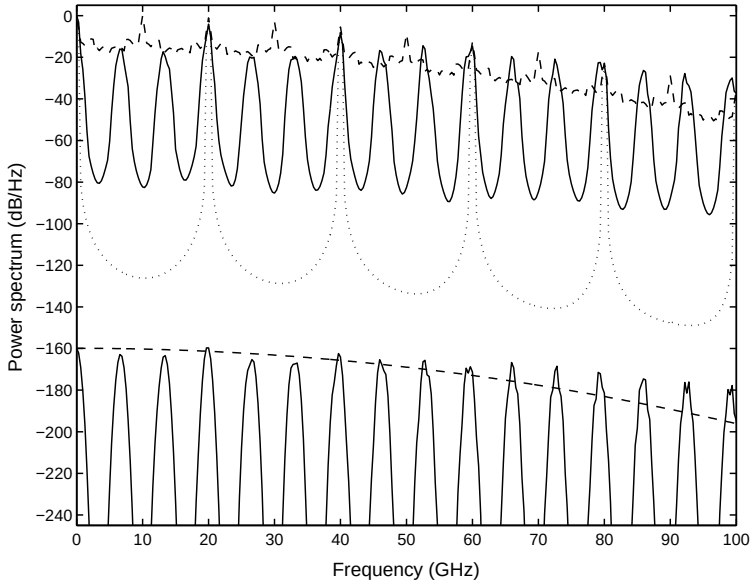

Figure 2.3: *The same as in Fig. 2.2, but with chirped pulses with* $C = 1$ *rad.*

$$\Delta_W\omega = \frac{4.3}{\sigma_\omega}\left|\xi + C/\sigma_\omega^2\right|^{-1} \cong 4.3\ \Omega_0 \frac{1}{t_0\sigma_\omega}\frac{\alpha}{\gamma}, \tag{2.24}$$

where, in the last approximation, we assume again that $|\xi| \gg \sigma_\omega^2$. Thus chirp reduces the width of the passbands irrespectively of its sign, through the factor σ_ω. Finally, the peak noise level in the top of the passbands of a train of chirped pulses can be raised or lowered depending on the value of p, as in the unchirped case. But this peak noise level also suffers the bandwidth enlargement of the wideband output noise envelope, $|J(\omega)|^2$, which always raises the peak noise level over the initial broadband noise.

In Fig. 2.3, we present a simulation of a train composed of chirped pulses. The chirp parameter is chosen as $C = 1$ rad. The remaining parameters are as in Fig. 2.2. The output noise envelope is broader than the input level owing to the existence of chirp. The passbands' width is $\Delta_W\omega = 2\pi\times 1.32$ GHz, and the relative redshift of the centers is 8.85×10^{-3}. For instance, the fourth output harmonic at 80 GHz is redshifted 708 MHz. We see a modulation of high-order harmonics, as in Fig. 2.2, and the lowering of the noise peak level of passbands, corresponding to nonoutput

harmonics in the left part of the plot, owing to nonmaximal modulation.

From relations (2.23) and (2.24), it is straightforward to realize that the magnitude and chirp of the individual pulses can be extracted from the values of the passband width and the passband shift. To be precise,

$$C = -2.9 \ \mathrm{sign}(\xi) \frac{\Omega_0}{s} \frac{\Delta^{(s)}_{\mathrm{peak}}\omega}{(\Delta_W \omega)^2}. \tag{2.25}$$

This measurement can be performed for any passband, not necessarily one of those surrounding the harmonics (s multiple of γ). Notice also that it is independent of the concrete Talbot device used, since it does not depend on the value of the Talbot index. This expression is also valid when modulation of the passband is present, although in those cases a fitting of the whole passband can be necessary to obtain precise values of width and shift.

2.2.3 Analysis of the Modulation

The passband functions $G_i(\omega)$ are modulated by a cosine-squared term both in the chirped and in the unchirped cases. Given a passband index s, the maximum value of the modulation factor $M_s(\omega) = 4p^2 \cos^2(\omega s t_0/2) + \sigma_b^2$ occurs for

$$\omega = m\Omega_0/s, \tag{2.26}$$

with m any integer. It is easy to show that in trains composed of unchirped pulses, the modulation and passband maxima coincide for the output harmonics, and only in these cases. Therefore nonoutput harmonic passbands ($s \neq h\gamma$) can show tips on top of the passbands, or lowering of the peak noise level if they are sufficiently narrow. When the pulses are chirped, the modulation maxima still remain over the harmonics, but the passbands are shifted.

The spectral modulation full width in the passband of index s is

$$\Delta_M \omega = \Omega_0/s. \tag{2.27}$$

In particular, the output harmonics correspond to indices $s = h\gamma$ so that $\Delta_M \omega = \Omega_0/h\gamma$. This width becomes smaller as the harmonic or passband index becomes larger, but it does not depend on the train characteristics, such as the temporal width, t_p , the value of the chirp, C, or the value of p. Then, modulation of the s passband appears when $\Delta_M \omega < \Delta_W \omega$, or equivalently when

$$4.3\ t_p > \frac{\gamma}{\alpha}\frac{t_0}{s}. \tag{2.28}$$

Then, modulation is present when the passband index s is high, the dispersion γ/α is small, or the relative width of the pulses t_p/t_0 is high.

The limit described in relation (2.28) is exemplified in Fig. 2.4, where we simulate a random 10-GHz train composed of 400 pulses with $t_p = 10$ ps, $\gamma/\alpha = 1$, $\xi = 1592$ ps^2/rad, and $p = 0.9$, so that the output train also has 10 GHz. The 10-dB passband full width is 4.3 GHz, while the modulation width in output harmonics is $10/h$ GHz, so that modulation is expected to be observable after the third output harmonic. The conventions in this plot are as in the previous figures. The peak noise level is raised 5.2 dB owing to the simulation of a nearly full train with $p = 0.9$. When

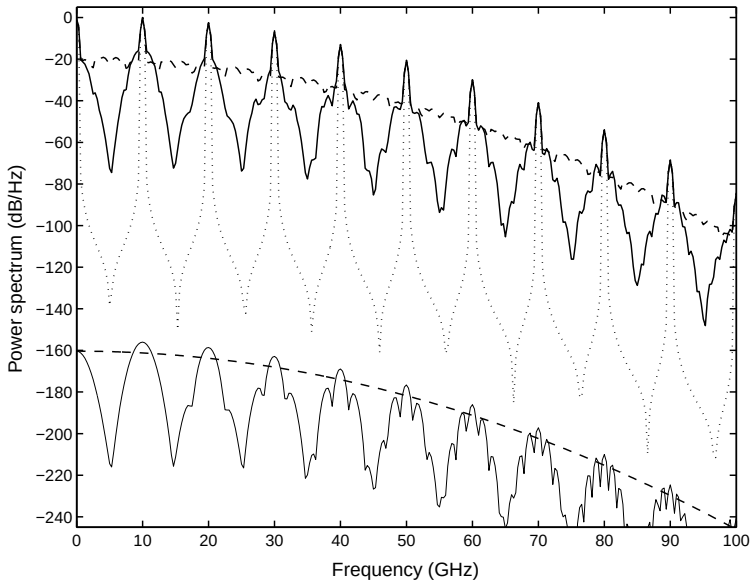

Figure 2.4: *Power spectrum of a detected 10-GHz, p=0.9 random train of unchirped pulses with 10-ps rms width after its pass through a Talbot filter width $\gamma/\alpha = 1$. The upper part of the plot shows (continuous curve) the power spectrum of the detected output train, (dashed curve) the power spectrum of the detected input train, and (dotted curve) the mean signal power spectrum of both input and output trains. The lower part shows analytical approximations to the noise power spectrum: (continuous curve) output noise; (dashed curve) input noise.*

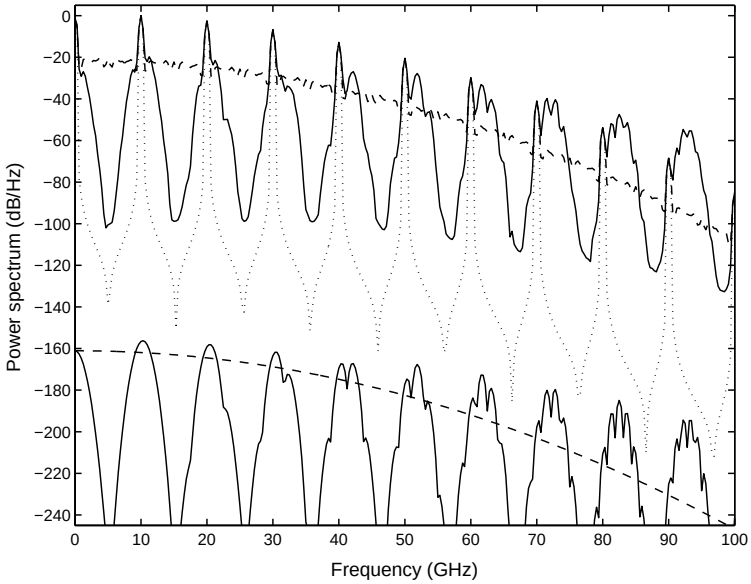

Figure 2.5: *Same as in Fig. 2.4, but with chirped pulses with* $C = -1$

modulation of a passband appears, the decay around the peak value has to consider both $\Delta_W\omega$ and $\Delta_M\omega$. However, since the modulation occurs for high harmonics, small dispersion, and broad pulses, the decay due to the structure of the passband is usually negligible, since $\Delta_W\omega$ is larger than $\Delta_M\omega$. Using relation (2.22), it is straightforward to compute the decay Γ between noise level in the harmonic and the first modulation zero due only to modulation, $\Gamma(\mathrm{dB}) = 10\log(1+3p)/(1-p)$.

In Fig. 2.4, the decay Γ is 16 dB. In the worst case ($p = 0.5$), Γ attains a minimum value of 7 dB. This is also the typical value of decay between consecutive maxima and minima of modulation in the same passband. When the approximation fails because $\Delta_W\omega$ and $\Delta_M\omega$ are of the same order, or when the center of the passband is shifted owing to the chirp of the basic pulses, the value of the decay Γ has to be reevaluated from relation (2.21).

To complete our examples, in Fig. 2.5 we plot our final simulation where chirp is taken into account. We choose the same parameters of simulation as in Fig. 2.4, except the value of the chirp, whose value is $C = -1$ rad. The chirped train blueshifts the center of the passbands, while the modulation does not change the position of its maxima. This results in asymmetric

patterns of modulation. The other features of the spectrum are as in Fig. 2.4.

2.3 Talbot imaging of mistimed pulses

This section deals with the study of a Talbot device, when it is fed with a jittery train of pulses. The analysis will be carried out in the temporal domain by means of the variance of the resulting train as well as in the Fourier domain by means of the power spectrum of the detected train.

Let us consider a train of pulses suffering from timing jitter, which can be represented by

$$a(t,0) = \sum_k f_0(t - kt_0 - a_k). \tag{2.29}$$

The function $f_0(t)$ denotes the pulse form and t_0 is the unit time of the train. The center of pulses in the train occurs at $t_k = kt_0 + a_k$ ($k = -\infty, \ldots, +\infty$). The set of variables a_k is an infinite collection of random numbers with dimensions of time representing the timing jitter of each pulse. If the random numbers are set to zero, the train of pulses has a period of t_0. Notice that we have considered that jitter shifts pulses from its ideal position but does not affect to their shape. The random variables are assumed to have a Gaussian probability density function with zero mean and standard deviation σ_j:

$$p(a_k) = \left(2\pi\sigma_j^2\right)^{-1/2} \exp\left(-a_k^2/2\sigma_j^2\right). \tag{2.30}$$

The average over all the realizations of each one of jitter parameters will be denoted by brackets, $\langle \cdots \rangle$. Therefore, $\langle a_k \rangle = 0$ and $\langle a_k^2 \rangle = \sigma_j^2$ for any pulse index k. As in the previous section, we will consider linearly chirped Gaussian pulses with rms width equal to t_p:

$$f_0(t) = \exp\left(-t^2(1 - iC)/2t_p^2\right), \tag{2.31}$$

C being the phase-modulation parameter or linear chirp. In order to avoid overlapping between incoming pulses we will assume that the pulse widths are smaller than the exact period, $t_p < t_0$, and the standard deviation of pulse center is smaller than pulse width $\sigma_j < t_p$.

If this jittery train, Eq. (2.29) is propagated through a dispersive line, the resulting optical envelope can be expressed as a coherent interference

of dispersed pulses:

$$\begin{aligned} a(t,\xi) &= \sum_k f_\xi(t - kt_0 - a_k) \\ &= \sum_k \int_{-\infty}^{+\infty} h(t-t',\xi) f_0(t' - kt_0 - a_k)\ dt', \end{aligned} \tag{2.32}$$

where ξ is the accumulated dispersion of the system, and $h(t,\xi)$ the impulse response or propagation kernel of a lowest-order dispersion medium with negligible attenuation. Using Eqs (1.20) and (2.31) the dispersed signal (2.32) results

$$a(t,\xi) = \left[\frac{t_p^2}{\rho(1-iC)}\right]^{1/2} \sum_k \exp\left[-\frac{(t-kt_0-a_k)^2}{2\rho}\right], \tag{2.33}$$

with

$$\rho = \frac{t_p^2}{(1-iC)} + i\xi. \tag{2.34}$$

We also compute for future use the dispersed signal in the Fourier domain, which can be written as

$$A(\omega,\xi) = t_p \left[\frac{2\pi}{1-iC}\right]^{1/2} \exp(-\rho\omega^2/2) \sum_k \exp(i\omega k t_0 + i\omega a_k). \tag{2.35}$$

Averaged fields can be computed in the time domain as follows. The mean value of the optical envelope is a sum of averaged individual pulses, or the result of the propagation through the linear system of the initial averaged field:

$$\langle a(t,\xi)\rangle = \sum_k \langle f_\xi(t - kt_0 - a_k)\rangle = \int_{-\infty}^{+\infty} h(t-t',\xi)\langle a(t',0)\rangle dt' \tag{2.36}$$

A simple computation of the dispersed field yields to:

$$\begin{aligned} \langle a(t,\xi)\rangle &= \sum_k \int_{-\infty}^{+\infty} f_\xi(t - kt_0 - a_k) p(a_k)\ da_k \\ &= \left[\frac{t_p^2}{\tilde\rho(1-iC)}\right]^{1/2} \sum_k \exp\left[-\frac{(t-kt_0-a_k)^2}{2\tilde\rho}\right], \end{aligned} \tag{2.37}$$

where we have introduced the notation $\tilde{\rho} = \rho + \sigma_j^2$. On the other hand, the initial averaged field is recovered by setting $\xi = 0$ in the value of $\tilde{\rho}$ in Eq. (2.37):

$$\begin{aligned}\langle a(t,0)\rangle = &\left[\frac{t_p^2}{t_p^2+\sigma_j^2(1+iC)}\right]^{1/2} \\ &\times \sum_k \exp\left[-(t-kt_0)^2\frac{1+iC}{2(t_p^2+\sigma_j^2(1+iC))}\right].\end{aligned} \tag{2.38}$$

Then, the pulse width of the average input pulses can be expressed as:

$$t_{\langle f_0\rangle} = t_p^2\left[1+\epsilon^2\frac{1+\epsilon^2(1+C^2)-C^2}{1+\epsilon^2(1+C^2)}\right], \tag{2.39}$$

where the parameter ϵ is the ratio between the standard deviation of the timing jitter and the original pulse width, $\epsilon = \sigma_j/t_p$. Thus, the averaged input field is affected by random jitter only as change in the pulse width. For unchirped trains, the incoming pulses are broaden by the factor $(t_p^2+\sigma_j^2)^{1/2}$. However, when input pulses are phase modulated, they may broaden or get narrow depending on chirp value. From Eq. (2.39) the transition occurs when

$$C = C_{\text{limit}} \equiv \left[\frac{1+\epsilon^2}{1-\epsilon^2}\right]^{1/2}. \tag{2.40}$$

Then, if $C < C_{\text{limit}}$ pulses are broaden by timing jitter while $C > C_{\text{limit}}$ yields to narrower pulses than the original ones. The computation and interpretation of the output field is similar to a deterministic signal, and the details of the computation are widely known [20–22] and are equivalent to those shown in chapter 1. In this section we will simply quote the results.

2.3.1 Variance

We are interested in the statistical variations of a concrete realization of a train of pulses affected by timing random jitter, rather than in mean values. To characterize them, it is necessary to calculate the corresponding variance. This quantity is defined as the averaged squared deviation of the field with respect to the mean for each temporal instant:

$$\begin{aligned} V(t,\xi) =& \langle\ |a(t,\xi) - \langle a(t,\xi)\rangle|^2\rangle \\ &= \langle a(t,\xi)\ a^*(t,\xi)\rangle - \langle a(t,\xi)\rangle\langle a^*(t,\xi)\rangle, \end{aligned} \tag{2.41}$$

and it has the usual interpretation as a measure of the variation of the output field at each sampling instant. Expressed as a coherent sum of dispersed pulses, Eq. (2.36), the variance is

$$\begin{aligned} V(t,\xi) =& \sum_k \sum_m \langle f_\xi(t - kt_0 - a_k)\ f_\xi(t - mt_0 - a_m)^*\rangle \\ &- \left| \sum_k \langle f_\xi(t - kt_0 - a_k)\rangle \right|^2 . \end{aligned} \tag{2.42}$$

Here we will assume that random variables a_k are mutually independent, which implies that $\langle g(a_k)h(a_p)\rangle = \langle g(a_k)\rangle\langle h(a_p)\rangle$ when $k \neq p$ for any functions g and h. Taking this into account, the variance can be easily cast as a sum over dispersed pulses:

$$V(t,\xi) = \sum_k \langle |f_\xi(t - kt_0 - a_k)|^2\rangle - |\langle f_\xi(t - kt_0 - a_k)\rangle|^2, \tag{2.43}$$

where the first part of the sum corresponds to the averaged square of each dispersed pulse and the second to the square of the average. It is a simple task to compute both contributions. The result is the difference of two trains of Gaussian functions:

$$\begin{aligned} V(t,\xi) =& \frac{t_p}{\sqrt{2}\eta_1(\xi)} \sum_k \exp\left[-\frac{(t - kt_0)^2}{2\eta_1(\xi)^2} \right] \\ &- \frac{t_p}{\sqrt{2}\eta_2(\xi)} \frac{t_p}{\overline{t}} \sum_k \exp\left[-\frac{(t - kt_0)^2}{2\eta_2(\xi)^2} \right], \end{aligned} \tag{2.44}$$

where we have introduced the following notations:

$$\eta_1(\xi)^2 = \frac{t_p^2\ \widehat{t}^{\,2} + \xi^2(1 + C^2)}{2t_p^2}, \tag{2.45}$$

$$\eta_2(\xi)^2 = \frac{\overline{t}^{\,4} + \left[\xi(1 + C^{\,2}) + Ct_p^2\ \right]^2}{2(1 + C^{\,2})\ \overline{t}^{\,2}}, \tag{2.46}$$

$\overline{t}^{\,2} = t_p^2 + \sigma_j^2(1+C^2)$ and $\widehat{t}^{\,2} = t_p^2 + 2\sigma_j^2$. Then the width $\eta_1(\xi)$ represents the rms widths of the averaged squared dispersed pulses, and $\eta_2(\xi)$ denotes the rms width of the square of the average dispersed pulse. Therefore, variance is composed of two contributions coming from individual dispersed pulses, which will be called of $\langle|f|^2\rangle$ and $|\langle f\rangle|^2$ type, respectively. Since $V(t,\xi)$ is a periodic series, it can also be expanded in a Fourier series of the form

$$V(t,\xi) = \sum_{k=-\infty}^{+\infty} g_k \exp(2\pi i k t/t_0) = g_0 + 2g_{\pm 1}\cos(2\pi t/t_0) + \dots \qquad (2.47)$$

with $g_k = g_{-k}$ and

$$\begin{aligned} g_k =& \sqrt{\pi}\,\frac{t_p}{t_0}\,\exp(-2\pi^2 k^2 \eta_1(\xi)^2/t_0^2) \\ &- \sqrt{\pi}\,\frac{t_p^2}{t_0\,\overline{t}}\,\exp(-2\pi^2 k^2 \eta_2(\xi)^2/t_0^2). \end{aligned} \qquad (2.48)$$

Both forms of the variance, Eqs. (2.44) and (2.47), will be used in what follows. From Eq. (2.47) it is worth noting that

$$\frac{1}{t_0}\int_{-t_0/2}^{t_0/2} V(t,\xi)\,dt = g_0 = \sqrt{\pi}\,\frac{t_p}{t_0}\left(1 - \frac{t_p}{\overline{t}}\right), \qquad (2.49)$$

that is, the mean value is constant and there is no dependence on the specific value of the dispersion parameter ξ.

The variance of the input field $V(t,0)$ can be recovered by setting $\xi = 0$ in Eq. (2.44) through the corresponding values of the widths, Eqs. (2.45) and (2.46). Since the jitter parameter is small compared with the width of the original pulses, $\sigma_j < t_p$, both widths become of the order of the original pulses, $\eta_1(0)$, $\eta_2(0) \approx t_p$. Moreover, since the pulses do not overlap, only two Gaussian functions contribute appreciably to $V(t,0)$ in the sum Eq. (2.44) for each unit interval. For instance, for the central period, $-t_0/2 < t < t_0/2$, the following approximations applies:

$$V(t,0) \cong \langle|f(t-a_0)|^2\rangle - |\langle f(t-a_0)\rangle|^2 \qquad (2.50)$$

$$= \frac{t_p}{\sqrt{2}\eta_1(0)}\sum_k \exp\left[-\frac{t^2}{2\eta_1(0)^2}\right] - \frac{t_p}{\sqrt{2}\eta_2(0)}\frac{t_p}{\overline{t}}\sum_k \exp\left[-\frac{t^2}{2\eta_2(0)^2}\right]$$

On the other hand, the variance of the output envelope cannot be approximated in this way: when ξ is different from zero, the dispersed widths [Eqs. (2.45) and (2.46)] are larger than t_0 , and then the Gaussian functions in Eq. (2.44) overlap between adjacent periods. Indeed, for a general Talbot condition, $\xi \approx t_0^2$, so that the order of the period of the pulses, $\eta_1(\xi)$, $\eta_2(\xi) \approx t_0$. In order to obtain a simpler expression for the variance $V(t,\xi)$ after the dispersive device, it is necessary to return to the Fourier expansion (2.47), whose coefficients are given in Eq. (2.48). Now, since $\eta_1(\xi)$, $\eta_2(\xi) \approx t_0$, all harmonics in this expansion are damped. The leading-order approximation is just the DC term:

$$V(t,\xi) \cong g_0. \tag{2.51}$$

This, together with Eq. (2.49), means that the output variance equals the mean value along the unit interval, and it is insensitive to ξ.

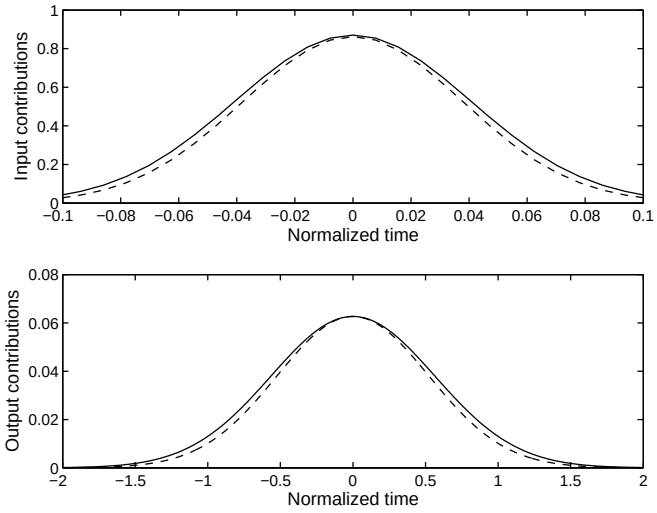

Figure 2.6: *Contributions of type* $\langle|f|^2\rangle$ *(solid curve) and* $|\langle f\rangle|^2$ *(dashed curve) to the input (top graph) and output (bottom graph) variances due to a signle pulse*

In fig. 2.6 we present the central pulse contributions $\langle|f|^2\rangle$ and $|\langle f\rangle|^2$ to input and output variances in an example. The period of the train has been chosen as $t_0 = 1$ in suitable units; then, the central unit interval is $-0.5 < t < 0.5$. Moreover, the $\gamma/\alpha = 1/4$, $t_p = 0.050$, $C = 0$ and

$\sigma_j = 0.020$. We have chosen a rather large jitter coefficient to emphasize the effect. Although a detailed analysis of this example is presented below, we show the result here to visualize the smoothing effect and discuss its physical basis. In the upper part of the plot, the initial contributions are contained in a single unit interval, so that they do not overlap with neighboring intervals. Moreover, their difference is large, so the variance $V(t,0)$ can be approximated to its difference, neglecting contributions from other pulses, as in Eq. (2.50). In the lower part we show these contributions after the dispersive device. Both have been broadened by dispersion, they overlap with other intervals, and their difference is smaller. Therefore, all the pulses in the output train of Eq. (2.44) must be added to give an approximation of the variance. The leading term in the approximation is the DC term, Eq. (2.51). Then, the dual behavior of the variance is a consequence of the dispersion of the individual pulses that smooth the difference between contributions $\langle |f|^2 \rangle$ and $|\langle f \rangle|^2$. In conclusion, the output variance is approximately constant. This conclusion remains valid as long as $\eta_1(\xi)$, $\eta_2(\xi) \approx t_0$ because of the truncation of the series of Eq. (2.47). However, for small-dispersion systems, or equivalently, for values of the Talbot index $\gamma/\alpha < 1$, the approximation may fail. This fact will be analyzed later.

2.3.1.1 Integer Talbot device

We start presenting an example of an integer Talbot device with index $\gamma/\alpha = 2$. The output train of pulses is an exact replica of the original one if jitter is absent. Our computations in the preceding paragraphs assume an infinite sequence of incoming pulses. To avoid the walk-off effect, a sufficiently long train of pulses has been considered in the simulations, and statistical analysis is carried out in the central region of the output trains.

A sequence of 200 Gaussian pulses was generated. The exact repetition period was normalized to unity, $t_0 = 1$. The pulses are unchirped Gaussian functions with a rms width of $t_p = 0.100$. The random jitter was added following a distribution with standard deviation of $\sigma_j = 0.015$. Each of the unit intervals was sampled with 128 points. The results of the simulation are represented in Figs. 2.7 and 2.8. In Fig. 2.7, the ten central unit intervals are shown for the input train of pulses (above) and for the output train (below). We observe the presence of signal in the space between pulses, an unusual feature compared with the exact Talbot effect. Moreover, differences between the heights of pulses are also clear. To show the smoothing effect, we superimposed ten unit intervals from the central

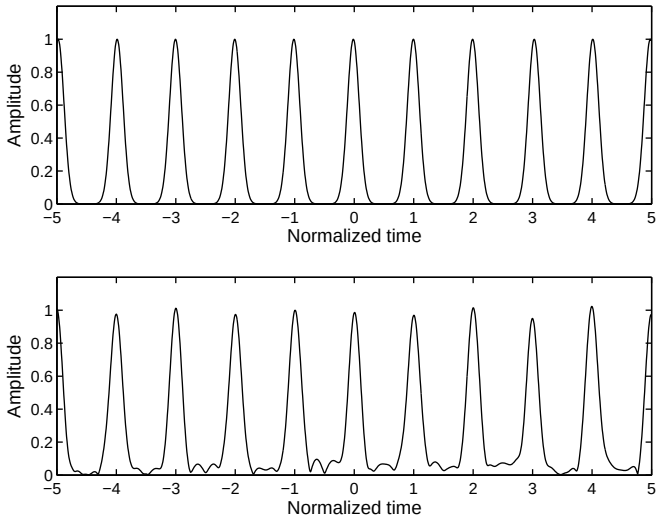

Figure 2.7: *Ten central unit intervals of the input (top) and output (bottom) trains of unchirped pulses in the integer Talbot device characterized by the index* $\gamma/\alpha = 2$. *The rms width of the input pulses is* $t_p = 0.100$ *and the standard deviation of random timing jitter is* $\sigma_j = 0.015$.

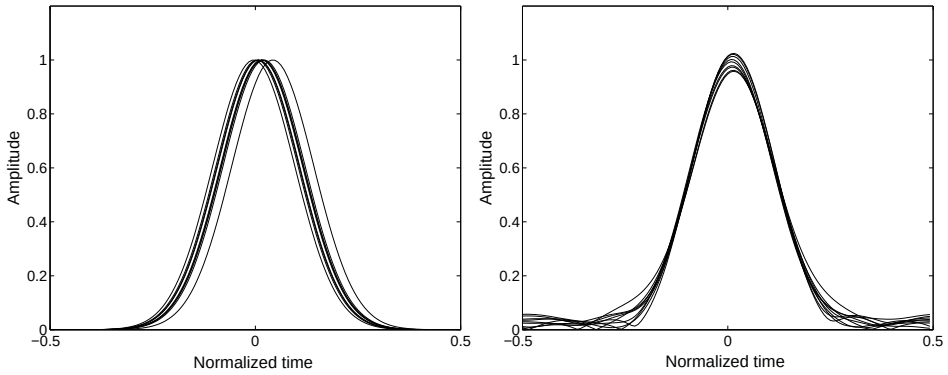

Figure 2.8: *Superposition of ten input (left side) and output (right side) in a unit interval in the integer Talbot device characterized by the index* $\gamma/\alpha = 2$. *Parameters as in Fig.2.8*

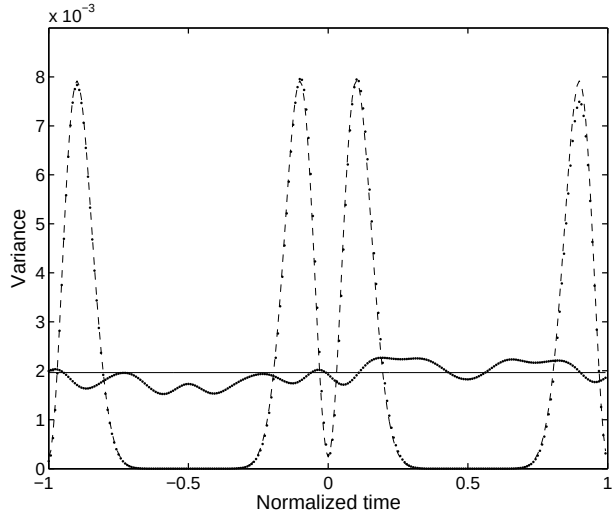

Figure 2.9: *Input variance in two unit intervals obtained from Eq. (2.50) (dashed curve) and through a numerical estimate over 100 sample trains (dots); output variance for $\gamma/\alpha = 2$ in two unit invervals obtained from Eq. (2.51) (solid line) and through a numerical estimation (dots). Parameters as in Fig 2.7.*

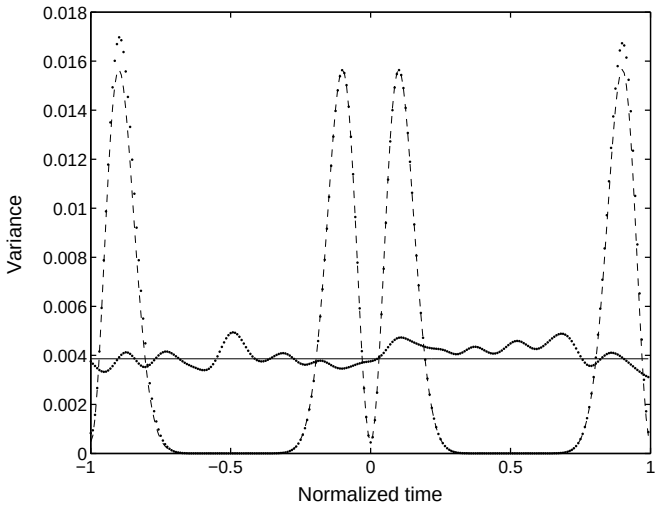

Figure 2.10: *The same as in Fig 2.7 but with chirped pulses with $C = -1$ rad.*

section of the pulse trains. In Fig. 2.8 we show the result for the input train on the left side and the output train, on the right side. In the first case, the edges of the pulses are displaced by random jitter. Assuming that statistical averages can be inferred from temporal averages, this means that for instants of time in the edges of the pulse, the variance of the process is high. In contrast, variations of the central peak and of the valleys between pulses are small, resulting in a small variance. The plot of the superposition of output pulses on the right side of Fig. 2.8 is different. Clearly, the edges present small variations, but the corresponding variations in valleys and peaks are increased. This behavior is in accordance with our observations concerning Fig. 2.7.

The time variations of the pulse envelopes are described by the input and output variances $V(t,0)$ and $V(t,\xi)$. To get a numerical estimate of these quantities, a set of 100 processes, each containing 200 pulses with different individual jitter parameters but with the same standard deviation $\sigma_j = 0.015$, was generated. Each of these experiments is described by the same set of parameters as before. We focused on the two central unit intervals, performing a point estimation of the variance for each of the 128 samples per period. The results are show in Fig. 2.9, where both the input and output variances are shown. The double-peaked function corresponds to the input train and the flat one to the output. The functions $V(t,0)$ and $V(t,\xi)$ have been evaluated from the exact expression of the variance as an infinite sum of pulses, Eq. (2.44). We note the good agreement between the estimate and the analytical formulas. The input and output approximations to the variance formula are not shown in this figure since they are indistinguishable from the result of Eq. (2.44). In particular, we note that the constant output variance given by Eq. (2.51) yields a value $V(t,\xi) = 0.0020$, in accordance with the results of this simulation. Note that we have evaluated the variance in Fig. 2.9 as an average over independent trains, not as temporal averages over the periods of a single train. This means that no ergodic assumptions have been made. However, we have verified that estimates from averages over periods yield results analogous to those in Fig. 2.9.

In fig. 2.10 we represent the input and output variances, for chirped Gaussian pulses with $C = -1$ rad. The remaining parameters are as in figure 2.9. By comparing both figures it is noticeable the increase of both input and output variance when input pulses are phase-modulated. This results can be inferred from the derived analytical expressions. The output variance, Eq. (2.51), is raised up to 0.0039 because of the increasing of

the parameter $\overline{t}$. The same happens in the input variance. In Eq. (2.50), the variance is obtained by the difference between the $\langle |f|^2 \rangle$ and $|\langle f \rangle|^2$. The chirp does not affect the first contribution, however the second one is increased in amplitude and reduced in width through the factor $\overline{t}$ in $\eta_2(0)$. Then, the difference between two contributions is raised leading to larger values of the variance.

2.3.1.2 $1/N$ Fractional Talbot Devices

In this section we will focus on the series of Talbot devices characterized by indices $\gamma/\alpha = 1/N$. They are known to provide a way to generate of trains of pulses with $N\times$ repetition rates with respect to the original train. Our first simulations deal with the Talbot dispersive device corresponding to $\gamma/\alpha = 1/4$. Again, a train of 200 unchirped Gaussian pulses was generated, in this case with $t_p = 0.050$ and $\sigma_j = 0.020$, the remaining parameters as before. The pulse width was reduced with respect to the value of the previous examples to show the $4\times$ repetition effect. In Fig. 2.11 we present the superposition in the same unit interval of ten sets of output unit intervals, each containing four slightly overlapped pulses. The variance of the pulses was also simulated with 100 trains of 200 pulses, and the estimates in the two central unit intervals are shown in Fig. 2.12. Again, we observe the initial double peak and the nearly flat output variance, with the same interpretation as in the previous example. The constant value of the output variance approximation of Eq. (2.51) is, in this case, 0.063, in accordance with the result of this simulation.

Although the constant value of the variance was a good approximation in this example, it was noted before that it may fail when the Talbot index γ/α is sufficiently small. We will show that for experiments designed to create high repetition rates, the output variance is still constant to a good approximation. The important observation is the following: Repetition rates of a given train are obtained if the individual pulses are narrow enough that they do not to overlap after the device. It is a simple task to quantify this observation for Gaussian pulses. We set as a criterion that overlapping is negligible when the midpoint between adjacent pulses has contributions in amplitude from both pulses that are not larger than 1/10 of the peak value. For Gaussian pulses this means that the pulse width for this limiting condition is

$$\frac{t_p}{t_0} = \frac{1}{2N\sqrt{2\ln 10}}. \tag{2.52}$$

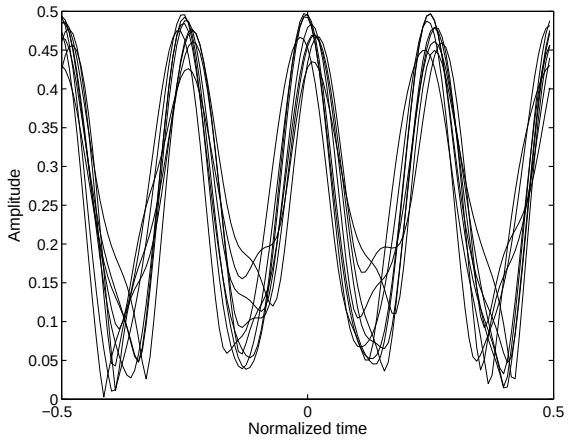

Figure 2.11: *Superposition of ten sequences of output pulses in a unit interval in the fractional Talbot device characterized by the index* $\gamma/\alpha = 1/4$*, leading to a* $4\times$ *repetition rate. The input pulses are unchirped and their rms width is* $t_p = 0.050$*. The standard deviation of random timing jitter is* $\sigma_j = 0.020$*.*

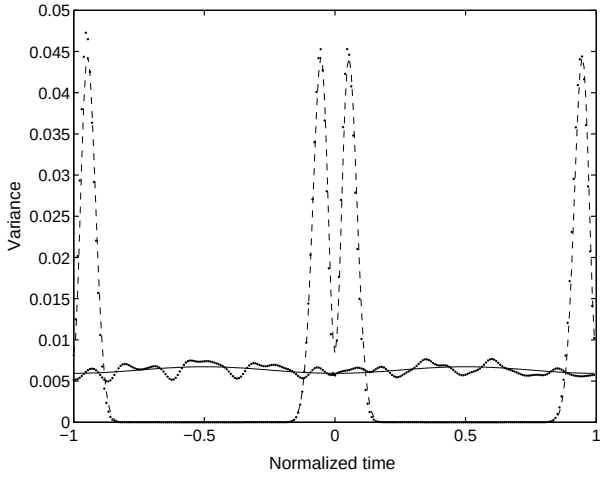

Figure 2.12: *Input variance in two unit intervals obtained from Eq. (2.50) (dashed curve) and through a numerical estimate over 100 sample trains (dots); output variance for* $\gamma/\alpha = 1/4$ *in two unit invervals obtained from Eq. (2.51) (solid line) and through a numerical estimation (dots). Parameters as in Fig 2.11.*

With this convention we can compute the damping coefficients $2\pi^2\eta_1^2(\xi)/t_0^2$ and $2\pi^2\eta_2^2(\xi)/t_0^2$ of the first harmonic in the expansion (2.47):

$$\begin{aligned} 2g_{\pm 1} =& 2\sqrt{\pi}\,\frac{t_p}{t_0}\,\exp(-2\pi^2\eta_1(\xi)^2/t_0^2) \\ & - 2\sqrt{\pi}\,\frac{t_p^2}{t_0\,\overline{t}}\,\exp(-2\pi^2\eta_2(\xi)^2/t_0^2). \end{aligned} \tag{2.53}$$

Here we will focus only on the second one, which in this example is smaller; see Fig. 2.6. Nevertheless, both have in general the same order of magnitude. This damping coefficient can be bounded for $\gamma/\alpha = 1/N$ as follows:

$$\begin{aligned} \frac{2\pi^2\eta_2(\xi)^2}{t_0^2} =& \frac{\pi^2\overline{t}^{\,2}}{(1+C^2)t_0^2} + \frac{t_0^2(1+C^2)}{4N\overline{t}^{\,2}} + \frac{t_p^4C^2\pi^2}{t_0^2\overline{t}^{\,2}(1+C^2)} + \pi C\frac{t_p^2}{\overline{t}^{\,2}} \\ & > \frac{t_0^2}{t_p^2}\frac{1+C^2}{8N^2} + C\frac{\pi}{2} = (1+C^2)\ln 10 + C\frac{\pi}{2} \geq \ln 10 \end{aligned} \tag{2.54}$$

where we have used the Talbot condition, Eq. (1.26), and notations (2.45) and (2.46), and, in the last inequality, that $\sigma_j < t_p$. Then, the value of $2\pi^2\eta_2(\xi)^2/t_0^2$ decreases as $1/N^2$, but since the ratio t_p/t_0 is also reduced by a factor N to avoid overlapping [see Eq. (2.52)], this damping coefficient is constant for any N. Moreover this coefficient is higher for phase modulated signals. In the most unfavorable case, $C = 0$, the value in Eq. (2.54) corresponds to a conservative damping factor of $\exp(-2\pi^2\eta_2(\xi)^2/t_0^2) < 0.10$. This results in a maximum modulation of the constant variance of 20%. The actual value of modulation is typically lower, especially if jitter is negligible. For the parameters presented here, with σ_j and t_p of the same order, the modulation is of 6%. Numerical results in Fig. 2.12 illustrate these values. Thus, we conclude that when the sequence of pulses is sufficiently narrow to avoid overlapping in the fractional Talbot series, the contribution of higher-order harmonics to expression (2.51) is to a good approximation negligible. If overlapping is allowed such that the ratio t_p/t_0 is kept constant, the constant approximation fails as γ/α decreases.

A new feature appearing in this last simulation is the increase of pulse pedestal in fractional Talbot devices. This fact is obscured in Fig. 2.11 because of the overlapping between adjacent pulses. In Fig. 2.13 we present a new simulation for the fractional device corresponding to $\gamma/\alpha = 1/2$, with $t_p = 0.040$, $C = 0$ and $\sigma_j = 0.007$. The presence of pedestal here is clear. To

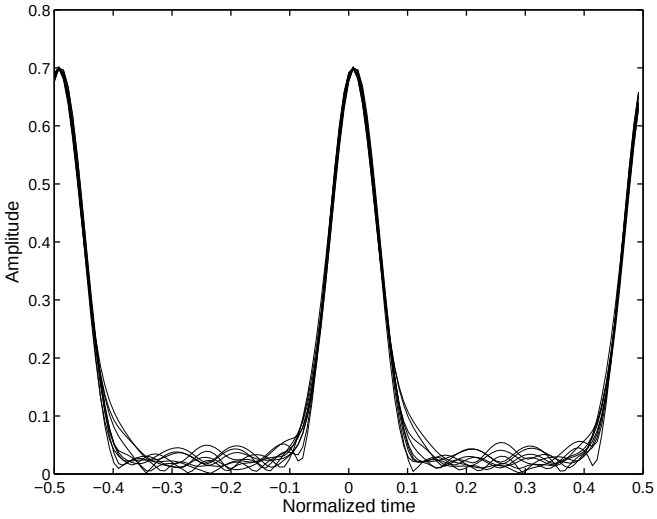

Figure 2.13: *Superposition of ten sequences of output pulses in a unit interval in the fractional Talbot device characterized by the index* $\gamma/\alpha = 1/2$*, leading to a* $2\times$ *repetition rate. The pulses are unchirped and their rms width is* $t_p = 0.040$*. The standard deviation of random timing jitter is* $\sigma_j = 0.007$*.*

analyze this feature, let us consider a general Talbot device characterized by an index γ/α. The repetition-rate series correspond to the fractional Talbot series $\gamma/\alpha = 1/N$. From Eq. (2.41) the power of the mean detected train $\langle a(t,\xi)a(t,\xi)^*\rangle$ is composed of the constant variance $V(t,\xi) = g_0$ plus the squared mean train $\langle a(t,\xi)\rangle\langle a(t,\xi)^*\rangle$, which vanishes between pulses. In turn, the peak value of the output pulses in a general Talbot device is damped [2,15] in amplitude by a factor of $1/\sqrt{\alpha}$ with respect to the original train, Eq. (2.38). Then, for Gaussian pulses the ratio between the peak amplitude of the detected train (A_{peak}) to the value between pulses ($\sigma_\xi^2 = g_0$) is

$$\begin{aligned}\frac{A_{peak}}{\sigma_\xi} &= \frac{1}{\sigma_\xi}\left[\frac{t_p^2}{\alpha\bar{t}\sqrt{2}\eta_2(0)} + \sigma_\xi^2\right]^{1/2} \cong \frac{t_p}{2^{1/4}\sqrt{\bar{t}\alpha\eta_2(0)}} \\ &\cong \frac{\sqrt{2}}{\pi^{1/4}}\frac{1}{\sqrt{\alpha}}\left(\frac{t_p}{t_0}\right)^{1/2}\frac{t_0}{\sigma_j(1+C^2)^{1/2}},\end{aligned} \tag{2.55}$$

where in the last approximation we have retained the leading order in the ratio σ_j/t_p from Eq. (2.49). Therefore, for a given amount of jitter the pedestal increases as $\sqrt{\alpha} = \sqrt{N}$. The chirp of the pulse increases the pedestal equivalently to an increase of the timing jitter by the factor $(1 + C^2)^{1/2}$. Moreover, the ratio decreases when the input pulses are wider. For the simulation in Fig. 2.13, this ratio is 21.2, with $A_{peak} = 0.70$ and $\sigma_\xi = 0.033$.

2.3.2 Intensity spectrum

In this section we approach the problem of a mistiming train from a spectral point of view, by analyzing the power spectral density of the detected jittery train before and after a Talbot device. Here, and in contrast to the previous time-domain study, in which independent pulse-to-pulse jitter variations were assumed, now arbitrary pulse-to-pulse timing jitter correlation is allowed. We will consider that correlation between pulses are stationary, and described by the function R, defined as $R(k) = R(-k) = \langle a_m a_{m\pm k}\rangle$. As in the previous section the jitter variables are assumed to have zero mean and standard deviation σ_j. Furthermore we will also assume that $\sigma_j\sigma_\omega \ll 1$. The approximate formulas for the power spectrum that we derive are based on a second-order expansion of $\sigma_j\sigma_\omega$ or equivalently, on a small-signal approximation in the variables a_k.

For deriving the expression of the power spectral density of the detected train, Eq. (2.6), we follow the same steps than in section 2.2.1, where the intensity spectrum of a random distributed pulse train was calculated. Let us assume that the correlator of the Fourier transformed detected train can be factorized as:

$$\begin{aligned}\langle I(\omega_1,\xi)I(\omega_2,\xi)^*\rangle =& \langle I(\omega_1,\xi)\rangle\langle I(\omega_2,\xi)^*\rangle \\ &+ 2\pi K(\omega_1,\omega_2)\sum_s \delta(\omega_1-\omega_2-2\pi s/t_0).\end{aligned} \tag{2.56}$$

where the function K will be derived below. From Eq.(2.56), the power spectral density can be split into two contributions: $S(\omega,\xi) = S^{(S)}(\omega,\xi) + S^{(N)}(\omega,\xi)$. $S^{(S)}$ is the signal contribution, previously analyzed in chapter 1 and $S^{(N)}$ is the noise one. Using Eqs. (2.6) and (2.7), we can straightforwardly show that the noise spectral density is the diagonal part of regular function K: $S^{(N)}(\omega,\xi) = K(\omega,\omega)$. Thus the problem of computing $S^{(N)}(\omega,\xi)$ reduces to computation of the Fourier-domain correlator and the mean Fourier intensity. Using

Eqs. (2.35) and (2.8) yields the photocurrent by Gaussian integration. Introducing the notation $\mu_m(\omega) = (\omega\rho - imt_0)\sigma_\omega^2/2$ results in

$$\begin{aligned} I(\omega,\xi) =& t_p\sqrt{\pi}\exp(-\rho\omega^2/2)\sum_{pk}\exp[-(a_p-a_k)^2\sigma_\omega^2/4] \\ &\times\exp(-i\omega kt_0+\mu_{p-k}^2/\sigma_\omega^2 - i\mu_{p-k}^* a_k - i\mu_{p-k}a_p). \end{aligned} \tag{2.57}$$

Now we substitute Eq. (2.57) into Eq. (2.56) and expand the exponentials in Eq. (2.57) to second order in jitter variables a_k, performing the expectation values according to small-signal approximation. The result is proportional to the correlations of timing jitter variables:

$$\begin{aligned} &\langle I(\omega_1,\xi)I(\omega_2,\xi)^*\rangle \cong \langle I(\omega_1,\xi)\rangle\langle I(\omega_2,\xi)^*\rangle + \pi t_p^2\exp(-\rho\omega_1^2/2-\rho^*\omega_2^2/2) \\ &\times\sum_k\exp[-i(\omega_1-\omega_2)kt_0]\sum_{rsq}\exp(-i\omega_2 qt_0)\exp[(\mu_r^2+\mu_s^{*2})/\sigma_\omega^2] \\ &\times[\mu_s^*\mu_r R(q-s+r)+\mu_s^*\mu_r^* R(q-s)+\mu_s\mu_r^* R(q)+\mu_r\mu_s R(q+r)] \end{aligned} \tag{2.58}$$

where μ_r is evaluated at ω_1 and μ_s at ω_2. From Eq. (2.58) the diagonal part of function K can be directly read:

$$\begin{aligned} t_0 S^{(N)}(\omega,\xi) \cong& \pi t_p^2\exp(-\omega^2/\sigma_\omega^2)\sum_{rsq}\exp(-i\omega qt_0)\exp[(\mu_r^2+\mu_s^{*2})/\sigma_\omega^2] \\ &\times[\mu_s^*\mu_r R(q-s+r)+\mu_s^*\mu_r^* R(q-s)+\mu_s\mu_r^* R(q)+\mu_r\mu_s R(q+r)] \end{aligned} \tag{2.59}$$

where the functions μ_r and μ_s are now evaluated at ω. Notice that in Eq. (2.59), $|\exp(\mu_r^2/\sigma_\omega^2)| = \exp(\omega^2/4\sigma_\omega^2)G_r(\omega)^{1/2}$, G_n being the passbands shown in previous section:

$$G_n(\omega) = \exp[-(\omega\xi+\omega C/\sigma_\omega^2 - nt_0)^2\sigma_\omega^2/2]. \tag{2.60}$$

The passbands have Gaussian form with peaks at $\omega \simeq t_0/|\xi|$ and rms width $1/\sigma_\omega^2|\xi|$. For Talbot lines, $|\xi| \approx t_0^2 \gg t_p^2 \approx 1/\sigma_\omega^2$, so that overlapping between passbands can be neglected. Under this conditions, $\exp[\mu_r^2(\omega)/\sigma_\omega^2] \cong \exp(\omega^2/2\sigma_\omega^2)G_r(\omega)\delta_{rs}$ and substitution into Eq. (2.59) yields

$$t_0 S^{(N)}(\omega,\xi) \cong \pi t_p^2 \exp(-\omega^2/2\sigma_\omega) \sum_n G_n(\omega) \tag{2.61}$$
$$\times \sum_q \exp(-i\omega q t_0)[2|\mu_n|^2 R(q) + \mu_n^{*2} R(q-n) + \mu_n^2 R(q+n)]$$

By reordering the sums over q, using the definition of μ_n the power spectral density can be expressed in the following more compact way:

$$t_0 S^{(N)}(\omega) \cong \omega^2 J(\omega)\Phi(\omega) \sum_n G_n(\omega) M_n(\omega) \tag{2.62}$$

where

$$\omega^2 J(\omega) = \pi t_p^2 \omega^2 \exp(-\omega^2/2\sigma_\omega^2), \tag{2.63}$$

$$\Phi(\omega) = \sum_k R(k) \exp(-i\omega k t_0) \tag{2.64}$$

and

$$M_n(\omega) = \left[\cos(\omega n t_0/2) - (\xi + C/\sigma_\omega^2 - n t_0/\omega)\sigma_\omega^2 \ \sin(\omega n t_0/2)\right]^2. \tag{2.65}$$

The power spectrum is composed of a sum of four types of contribution. The first one is a smooth broadband function, $\omega^2 J(\omega)$, which represents the envelope function of noise in the spectral domain that has bandwidth of the order of σ_ω. The second function, $\Phi(\omega)$, is the power spectrum of the timing jitter, which is the Fourier transform of the jitter correlation function. This function is manifestly Ω_0 periodic, and, in general, it is narrowband about the harmonics [75, 78]. However, in the noncorrelated timing noise limit, $R(k) = \sigma_j^2 \delta_{k,0}$, the jitter noise becomes white, i.e., $\Phi(\omega) = \sigma_j^2$.

The terms in the sum in formula (2.62), however, are dispersion dependent and jitter independent. Each term in this sum is composed of a narrowband Gaussian function $G_n(\omega)$, to which we refer as the n passband, and an oscillatory function $M_n(\omega)$, to which we refer as the modulation function of the n passband. The functions $G_n(\omega)$ account for the portions of noise at which the previous noise contributions, $\omega^2 J(\omega)$ and $\Phi(\omega)$, are damped, thus providing the mechanism of noise filtering by multiple interference.

Firstly we analyze the noise power spectrum of the incoming train by

setting $\xi = 0$ in Eqs. (2.60) and (2.65). This is the RF noise of the intensity of the train before it enters the dispersive line, measured by direct detection of the train with a high bandwidth photodetector. From Eq. (2.60), the passbands become centred at $\omega = nt_0\sigma_\omega^2/|C|$. Because $t_0 > 1/\sigma_\omega$ and the bandwidth of the spectrum of the individual pulses is of the order of σ_ω, the peak contribution of $G_n(\omega)$ when $n \neq 0$ lies outside the pulse spectrum. Therefore we neglect the contributions of all the passband functions except that with index $n = 0$. In addition, the corresponding modulation function is unity, $M_0(\omega) = 1$, and thus the input noise spectrum reduces to

$$t_0 S^{(N)}(\omega, 0) \cong \omega^2 |F(\omega)|^2 \Phi(\omega), \tag{2.66}$$

where $|F(\omega)|^2 = \pi t_p^2 \exp(-\omega^2 t_p^2/2)$ is the spectrum of the intensity of a single pulse, $|f_0(t)|^2$. It is well known in the context of characterization of noise in fundamentally mode-locked lasers [75–78]. It corresponds to the noise spectrum of a detected jittery train $\sum_k |f_0(t - kt_0 - a_k)|^2$, where we have neglected pulse overlap in the incoming train. It shows again the fact that to neglect the contributions of G_n functions is equivalent to neglect overlapping among pulses, since G_n represents the interference among n-th neighboring pulse. Notice that Eq. (2.66), is chirp-independent owing to the fact that direct detection of original train misses phase information.

When a replica of the train is created after a Talbot dispersive line, the basic features of the noise spectrum are similar to those found in the analysis of noise induced by on-off keying of an exact train (see Eq. (2.21) in section 2.2). First, the broadband envelope of the spectrum, $\omega^2 J(\omega)$, extends along the optical linewidth of a single pulse of the train such that, if the pulses are chirped, the noise bandwidth is broader than the bandwidth of the input noise envelope $\omega^2|F(\omega)|^2$. Second, noise is filtered around the maxima of the passbands $G_n(\omega)$. These maxima are located at

$$\omega_n = \frac{nt_0}{|\xi + C/\sigma_\omega^2|} \cong \alpha\Omega_0 \frac{n}{\gamma}\left[1 - \frac{1}{2\pi} sign(\xi) C \frac{\alpha}{\gamma}\frac{\Omega_0^2}{\sigma_\omega^2}\right]. \tag{2.67}$$

According to formula (2.67), when the initial pulses are unchirped and passband function index n is a multiple of γ, these passbands are centered at the harmonics of the output train. When Talbot index γ is not unity, between two consecutive output harmonics there are $\gamma - 1$ passbands uniformly separated. When the initial pulses are chirped there exists a deviation of the maxima of the passband functions $G_n(\omega)$ that depends on the relative sign between dispersion and chirp. When dispersion is positive, $\xi > 0$, the maxima [formula (2.67)] are redshifted (blueshifted) if the chirp

is positive (negative). The passband with index n will therefore exhibit a maximum in the neighborhood of a harmonic of the output train when $n = h\gamma$, where h is the harmonic index. The noise maximum can be raised with respect to the noise value before dispersion. Nevertheless, the precise value of noise at the harmonic frequencies $h\alpha\Omega_0$ does not change. The full width of the 10-dB decay of these passbands is computed from Eq. (2.60), providing a simple estimate of the bandwidth of the resultant noise spectrum about the harmonics:

$$\Delta_W \omega = \frac{2\sqrt{2}}{\sqrt{\log e}} \frac{1}{|\xi + C/\sigma_\omega^2|} \cong \frac{4.3}{\sigma_\omega |\xi|} = \frac{4.3}{t_0 Q}. \tag{2.68}$$

This width is common to all passbands. In formula (2.68) we have defined the parameter Q:

$$Q = \frac{\gamma}{\alpha} \frac{\sigma_\omega}{\Omega_0}. \tag{2.69}$$

Because the temporal width of a pulse after a dispersive line of high dispersion ξ goes as $t_0 Q$ [5], Q is the temporal dispersion-induced spread of an individual pulse with respect to the pulse separation and represents the number of basic time periods of the original train that occupies a pulse after dispersion.

Finally, each of these passband functions, $G_n(\omega)$ is modulated by the functions $M_n(\omega)$. In this case the structure of the modulation is richer than that found in the analysis of on-off-keyed trains after Talbot devices. First, notice that on the top of the passbands that correspond to output harmonics ($n = h\gamma$) the value of $M_n(\omega)$ is unity, showing ripples as the offset from the top increases. When the passband index does not correspond to an output harmonic, however, the modulation function does not reach a local maximum on top of the passband. Then these passbands show tips on top that are due to this nonmaximal modulation. Moreover, modulation maxima are in general bigger than unity, so noise can rise above the broadband envelope [Eq. (2.63)]. We present an example of this property in next subsection below. Noise vanishes when modulation reaches zero, $M_n(\omega) = 0$; near the n passband that corresponds to the h harmonic, the equation $M_n(\omega) = 0$ can be represented by means of a variable x that accounts for the offset from the value of the harmonic, $\omega(x) = \Omega_0(h\alpha + x)$. Then the zeros of the modulation are the solutions of

$$\cot(\pi h \gamma x) = \text{sign}(\xi) C + 2\pi Q^2 \frac{\alpha}{\gamma} \frac{x}{x + h\alpha}. \tag{2.70}$$

A graphic analysis of this function shows that there exist two different sets of solutions, which correspond to equal numbers of positive and negative values of x. There exists a zero in each incremental offset of width Ω_0/n on the left and the right sides of the harmonics that correspond to the branches of the cotangent function. The location of the zeros is not exactly symmetric with respect to the harmonic, even in the absence of chirp. Therefore, noise skirts around harmonics will always be asymmetric. Because of the decreasing character of the branches of the cotangent function, when both chirp and dispersion have different sign the zeros of modulation are located at lower values of the offset than those with unchirped pulses. If chirp and dispersion have the same signs, the offset of the zeros increases. For large values of Q the two sets of left and right solutions approximate the solutions of $\tan(\pi h\gamma x) = 0$. These properties are also exemplified and analyzed in the next subsection.

To present examples of the power spectrum it is necessary to introduce a concrete model for the correlation between pulses. It is not our objective to review the possible characteristics of noise and its origin. They ultimately depend on the concrete systems that generate the trains. Here we show two simple models derived from the noise theory of mode-locked lasers [78], which permits a general illustration of the traces in the intensity spectrum by consideration of two different types of pulse-to-pulse timing jitter correlation.

2.3.2.1 Pulse-To-Pulse Partially Correlated Noise

The noise spectral density functions of fundamentally mode-locked lasers, before dispersive propagation, present identical peaks at multiples of the pulse repetition frequency [78]. This partially correlated noise can be portrayed by a recursive relation between adjacent pulses. The deviation of the center of the pulses is a fraction $\eta > 0$ of the deviation of the previous pulse, augmented by an additional term ϵ_m:

$$a_m = \eta a_{m-1} + \epsilon_m. \tag{2.71}$$

It is assumed that both quantities have zero mean, $\langle a_m \rangle = \langle \epsilon_m \rangle = 0$, and that the additional terms are mutually independent and thus uncorrelated, $\langle \epsilon_m \epsilon_n \rangle = T^2 \delta_{m,n}$. Therefore η controls the correlation between pulses and depends on the underlying mechanism of pulse generation. The jitter variations described by parameter ϵ_m , however, represent noise induced by spontaneous emission or vacuum fluctuations.

The relation of the two parameters, η and T, to the rms value of jitter is $T^2 = \sigma_j^2(1-\eta^2)$. The correlation function is $R(k) = \sigma_j^2\eta^{|k|}$. Thus jitter noise is uncorrelated and therefore white when $\eta = 0$, whereas totally correlated noise corresponds to $\eta = 1$. The timing jitters spectral density is straightforwardly computed from the correlation, resulting in a Fabry-Perot-type function:

$$\phi(\omega) = \sigma_j^2 \frac{1-\eta^2}{1-2\eta\cos(\omega t_0)+\eta^2}. \tag{2.72}$$

Notice that this function is manifestly periodic, with a period equal to the fundamental harmonic of the train, and is peaked in the harmonics. Thus the noise spectrum's density before it enters the Talbot dispersive line has symmetric noise RF sidebands or skirts around each harmonic. Expansion of Eq. (2.72) around a harmonic $h\Omega_0$ reduces the form of the skirts to a Lorentzian shape [78].

In all the examples presented the pulse-to-pulse-temporal separation is $t_0 = 100$ ps, corresponding to trains with repetition rate $\Omega_0 = 2\pi \times 10$ GHz. The temporal width of the pulses in the train is $t_p = 10$ ps, and the jitter's standard deviation is $\sigma_j = 100$ fs. The simulations presented here were generated from a string of 1024 basic periods, each with 64 sample points. The power spectrum is estimated numerically by use of the Bartlett algorithm [80], averaging 8 spectra, each obtained from a sequence of 128 time periods. The frequency separation of the points in the spectrum is therefore 78 MHz ($= 1/128 \times 100$ ps). Jitter is created numerically by use of standard pseudorandom number generators and recursive relation (2.71).

In Fig. 2.14 we represent the spectrum of a train of unchirped pulses ($C = 0$) that corresponds to the intensity of the jittery train before and after the Talbot dispersive line. Dispersion is adjusted to create the first integer Talbot image of the original train ($\gamma/\alpha = 1$), so $Q = 1.59$. The parameter that describes correlation is $\eta = 0.7$. In the lower part of Fig. 2.14 we represent by a dashed curve our analytical approximation of the noise spectral power of the detected train before it enters this dispersive device, as given by formula (2.66). By a continuous curve we plot analytical formula (2.62) of the noise spectral power of same train detected after the Talbot device. In the upper part of the figure we depict the simulation of the spectra before and after the Talbot dispersive line, normalizing the DC component to 0 dB. These spectra show peaked contributions that correspond to the harmonics of a perfect train. To help

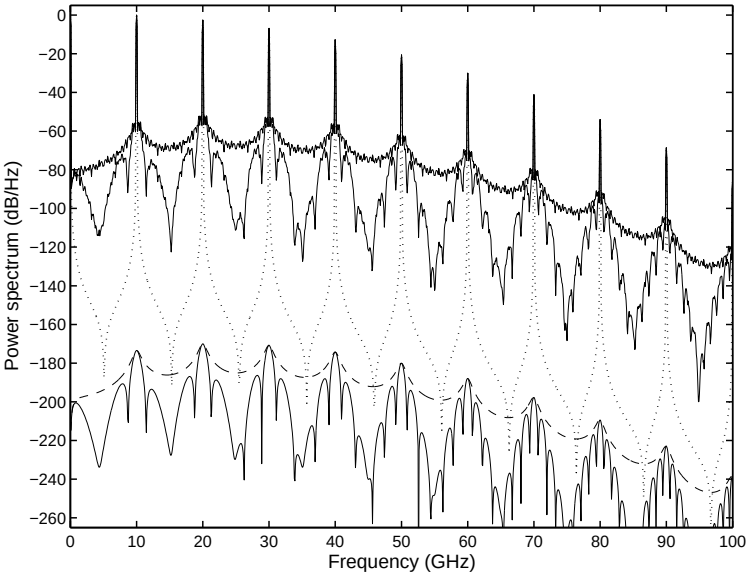

Figure 2.14: *Intensity power spectral density (PSD) of a jittery train of pulses ($\sigma_j = 100$ fs, $\eta = 0.7$) before and after a temporal Talbot device with index $\gamma/\alpha = 1$. Pulse width, $t_p = 10$ps; chirp, $C = 0$; repetition rate, 10 GHz; Q=1.59. Above, numerical power spectral densities for the input and output trains (continuous curves) and numerical power spectral density of the mean signal (dotted curve). Below, analytical noise power spectral densities for the input (dashed curve) and output (continuous curve) trains.*

in visualizing the contributions of noise we represent the spectrum of the mean signal by using a dotted curve. The agreement between simulations and analytical formulas is excellent.

To appreciate the different contributions to the RF noise skirts around the harmonics, we plot in Fig. 2.15 the contributions to noise in the right-hand offset near 50 GHz. The offset runs up to 5 GHz, the midpoint between harmonics. At the left in Fig. 2.15, and normalizing the power spectrum to 0 dB at zero offset, we represent jitter power spectrum $\Phi(\omega)$ by using a dashed curve, modulation function $M_{n=5}(\omega)$ by using a continuous curve, and passband function $G_{n=5}(\omega)$ with a dotted curve. The different contributions to the total power spectrum are clearly observed. The jitter power spectrum has a 10-dB half-width of 1.71 GHz; the 10-dB decay half-width of passband function $G_{n=5}(\omega)$ is 2.15 GHz.

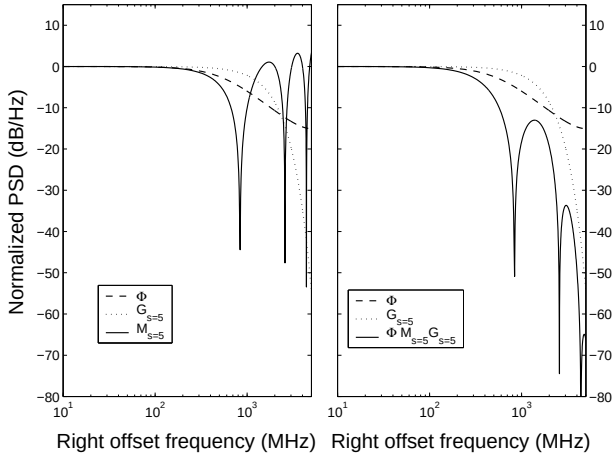

Figure 2.15: *Contribution to the right-hand offset noise spectrum of the train in Fig. 2.14 near the fifth harmonic ($n = h = 5$). Left, dashed curve, jitter power spectrum $\Phi(\omega)$; dotted curve, pass band $G_{n=5}(\omega)$; continuous curve, modulation function $M_{n=5}(\omega)$. Right, dashed curve, jitter power spectrum $\Phi(\omega)$; dotted curve, band pass function $G_{n=5}(\omega)$; continuous curve, product $\Phi(\omega)G_{n=5}(\omega)M_{n=5}(\omega)$. PSD, power spectral density.*

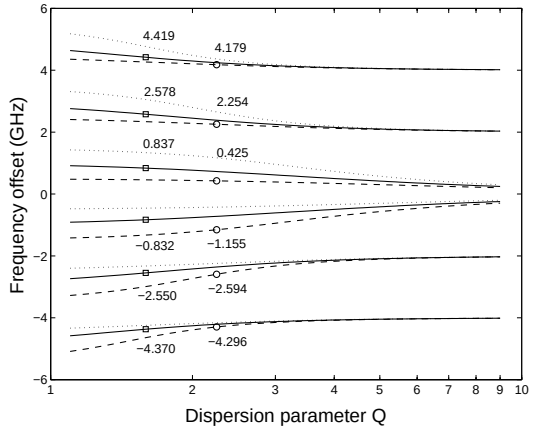

Figure 2.16: *Frequency offsets corresponding to the location of the zeros of the modulation function for the fifth harmonic ($h = 5$) and the first integer Talbot replica ($\gamma/\alpha = 1$). Chirp: $C = 0$, continuous curves; $C = 1$, dashed curves; $C = -1$, dotted curves.*

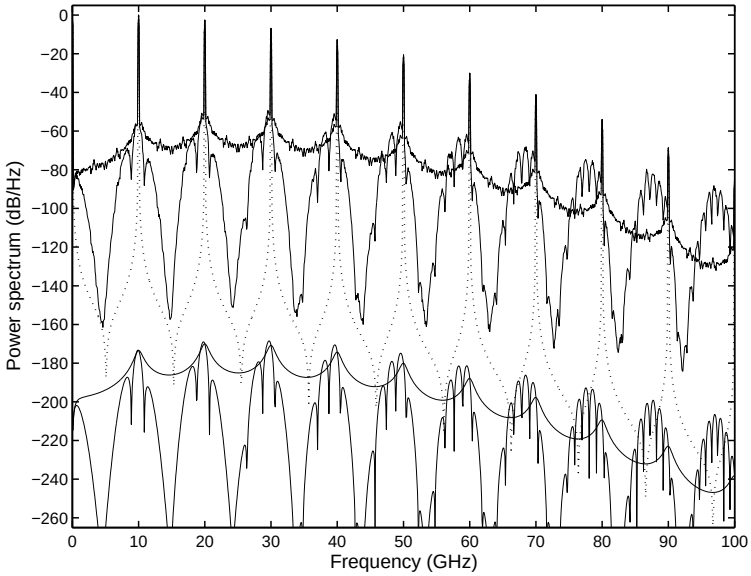

Figure 2.17: *Intensity power spectral density (PSD) of a jittery train of pulses ($\sigma_j = 100$ fs, $\eta = 0.7$) before and after a temporal Talbot device with index $\gamma/\alpha = 1$. Pulse width, $t_p = 10$ps; chirp, $C = 1$; repetition rate, 10 GHz; Q=2.25. Above, numerical power spectral densities for the input and output trains (continuous curves) and numerical power spectral density of the mean signal (dotted curve). Below, analytical noise power spectral densities for the input (dahsed curve) and output (continuous curve) trains.*

Modulation function $M_{n=5}(\omega)$ provides an additional structure to the resultant right-hand noise skirt. The product of these contributions is depicted at the right in Fig. 2.15 by continuous curve, together with the contributions of the passband function and the jitter power spectrum for comparison. Notice that the global 10-dB decay half-width has been reduced to less than 600 MHz.

The locations of the zeros of the modulation in Fig. 2.15 were obtained by numerical integration of Eq. (2.70). In Fig. 2.16 we present the positions of the offset that correspond to the zeros as a function of parameter Q for the fifth harmonic ($h = 5$), and the first integer Talbot device ($\gamma/\alpha = 1$), for three values of the pulse chirp: $C = 0$ (continuous curves), $C = 1$ rad (dashed curves), and $C = -1$ rad (dotted curves). There are six zeros in the offset range from -6 to 6 GHz, three on each

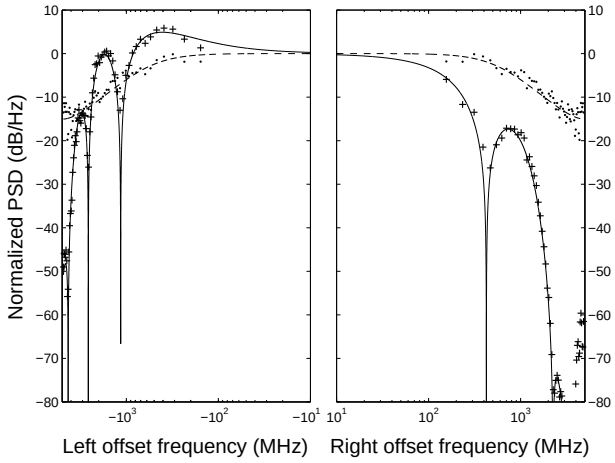

Figure 2.18: *Left and right offset noise power spectra of the train of Fig. 2.17 around the fifth harmonic ($n = h = 5$). Dashed curves, analytical input noise power spectral density (PSD). Continuous curves, analytical output noise power spectral density. Numerical data extracted from Fig. 2.17 superimposed: dots, input noise; crosses, output noise.*

side, and each in an incremental offset of 2 GHz. As dispersion is positive, positive chirp lowers the offset, whereas negative chirp raises it. Notice also that the zeros of the modulation tend to the roots of the tangent for high values of Q, as anticipated from the structure of Eq. (2.70). In Figs. 2.14 and 2.15 the value of parameter Q is 1.59. The corresponding zeros and their offset values are marked by open squares in Fig. 2.16, in agreement with our simulation of Fig. 2.14.

In Fig. 2.17 we present, following the same conventions as above, a 10-GHz train composed of Gaussian pulses, also with width $t_p = 10$ ps and $\eta = 0.7$ but now chirped with $C = 1$ rad ($Q = 2.25$). The centers of the passbands are redshifted owing to chirp. This asymmetry, together with the modulation, result in a globally asymmetric noise pattern. Moreover, after the fifth harmonic the noise after the Talbot device is greater than noise before the Talbot device in the left-hand offset region. To illustrate the noise sidebands of the fifth harmonic, we plot in Fig. 2.18 the left and right noise skirts up to offsets of ± 5 GHz, where the asymmetry of the output noise is apparent. With a dashed curve we present the jitters power spectral density $\Phi(\omega)$ [Eq. (2.72)]. The output-noise approximation

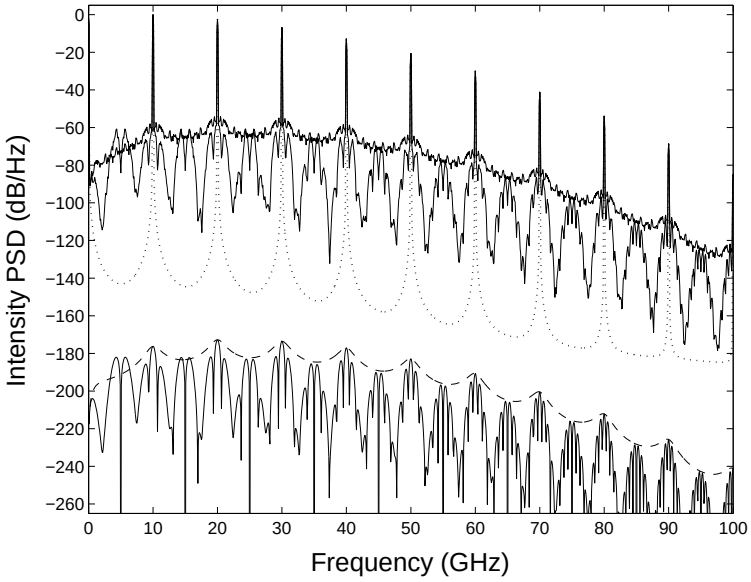

Figure 2.19: *Intensity power spectral density (PSD) of a jittery train of pulses ($\sigma_j = 100$ fs, $\eta = 0.5$) before and after a temporal Talbot device with index $\gamma/\alpha = 2$. Pulse width $t_p = 10$ ps; chirp, $C = 0$; repetition rate, 10 GHz; $Q = 3.18$. Above, numerical power-spectral densities for the input and output trains (continuous curves), and numerical power spectral density of the mean signal (dotted curve). Below, analytical noise power spectral densities for the input (dashed curve) and output (continuous curve) trains.*

[formula (2.62)], is represented by a continuous curve. We subtracted from this last spectrum the input noise envelope $\pi t_p^2 \omega^2 \exp(-\omega^2 t_p^2/2)$, such that the represented function coincides with the product $\Phi(\omega) G_{n=5}(\omega) M_{n=5}(\omega)$. Dots for the input and crosses for the output are superimposed upon the numerical data taken from Fig. 2.17. We have avoided the use of points with offsets below 100 MHz because they overlap the peaks that represent the harmonics. The zeros of the output noise as well as their numerical values were depicted previously by circles in Fig. 2.16.

Finally, in Figs. 2.19 and 2.20 we present a new example of a power spectrum that corresponds to the replica of a 10- GHz train in the second integer Talbot dispersive device, $\gamma/\alpha = 2$, composed of unchirped pulses $C = 0$ of width $t_p = 10$ ps, such that $Q = 3.18$. Timing jitter is added, with $\eta = 0.5$. In Fig. 2.19 we show the overall form of the spectrum,

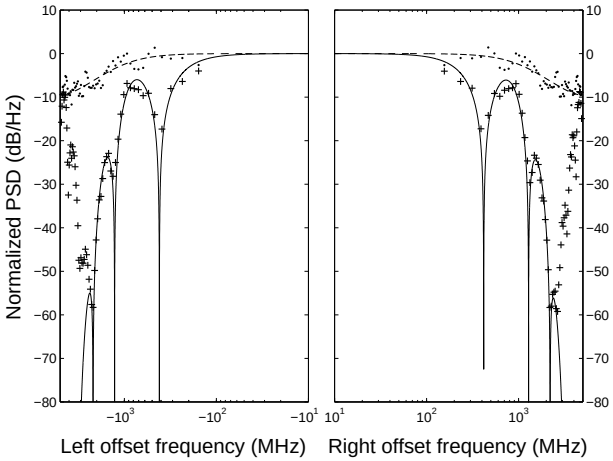

Figure 2.20: *Left and right offset noise power spectra of the train of Fig. 2.19 around the fifth harmonic ($n = h = 5$). Dashed curves, analytical input noise power spectral density (PSD). Continuous curves, analytical output noise power spectral density. Numerical data extracted from Fig. 2.19 superimposed: dots, input noise; crosses, output noise.*

which presents new passbands between consecutive harmonics. Notice the elevation above the broadband noise envelope of the first passband at 5 GHz that is due to the modulation. Fig. 2.20 corresponds to a double logarithmic plot of the noise skirts around the fifth harmonic (tenth passband). We plotted the analytical continuous curve by taking into account only the tenth passbands. Therefore, at the left and right sides of this plot, below -2.5 GHz and above 2.5 GHz, the numerical data of the output noise correspond to portions of the ninth and eleventh passbands, which are centered at 45 and 55 GHz, respectively. Using Eq. (2.70), we computed the zeros of the modulation of the central passband; the values of the offsets are 2204, 1286, 418, 2417, 21278, and 22191 MHz, in agreement with the locations in Fig. 2.20.

2.3.2.2 Pulse-To-N^{th}-Pulse Partially Correlated Noise

Different noise patterns arise when the partial pulse-to-pulse jitter correlation have more general functional forms. In some cases, jitter is uncorrelated between adjacent pulses, but is correlated between one pulse

and its N-th neighbor. This is the case in the noise spectral density of harmonically mode-locked lasers, and it is manifested as noise peaks at multiples of the cavity round-tip frequency, in addition to those at multipes of the pulse repetition frequency. This noise is commonly referred to as supermode noise [78]. Thus they show $N-1$ equidistant noise peaks between two harmonics of the signal, N being the number of pulses that coexist in the cavity at the same time. They can be modeled by means of a recursive relation of the type [78]:

$$a_{m+N} = \eta a_m + \epsilon_m. \tag{2.73}$$

As in the previous example it is assumed that $\langle a_m \rangle = \langle \epsilon_m \rangle = 0$ and the variables ϵ_m are uncorrelated $\langle \epsilon_m \epsilon_n \rangle = T^2 \delta_{mn}$. With this considerations and following the same steps than in the previous section we straightforwardly achieve the power spectral density of the timing jitter:

$$\Phi(\omega) = \sigma_j^2 \frac{1-\eta^2}{1-2\eta\cos(\omega N t_0)+\eta^2}. \tag{2.74}$$

As expected, Eq.(2.74) is a peaked function with period N times the period of the train. Note that in the derivation of the noise power spectral density [formula (2.62)] leading to (2.74), we have considered that pulses in the train are coherent and therefore carried by the same optical frequency. However this is not generally true when we treat with harmonically mode-locked laser, since different time interleaved trains can be carried by different central frequencies. A general analysis of this fact will not be studied here. However, oscillation on the same carrier (as well as timing jitter correlation) can be forced by placing a Fabry-Perot etalon in the cavity [81].

In figures. 2.21 and 2.22 the power spectral density of a 10-GHz train of unchirped pulses ($C = 0$) before and after a Talbot device, is presented following the same conventions as the previous examples. We represent the analytical noise power spectrum density in the upper part while in the lower part the power spectrum density resulting from the simulation is plotted. In this case, the timing jitter is created numerically by use of standard pseudorandom number generators and recursive relation (2.73) setting $N = 2$. The parameters of the train and the jitter are: $t_p = 10$ ps, $\sigma_j = 100$ fs and $\eta = 0.7$. The spectra show high peaks due to the harmonics of the signal that have been depicted by dotted curve. From both figures the noise power spectral density of the input signal shows apart from peaks at harmonics of the train, a supermode peak between two

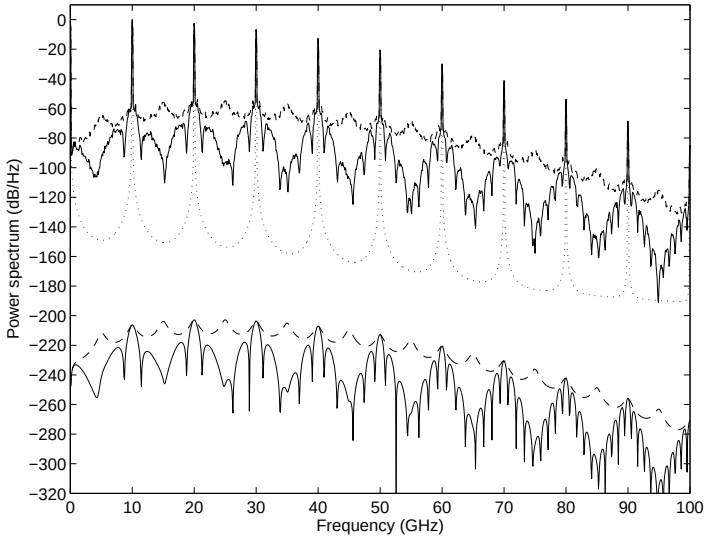

Figure 2.21: *The same as in Figure 2.14.*

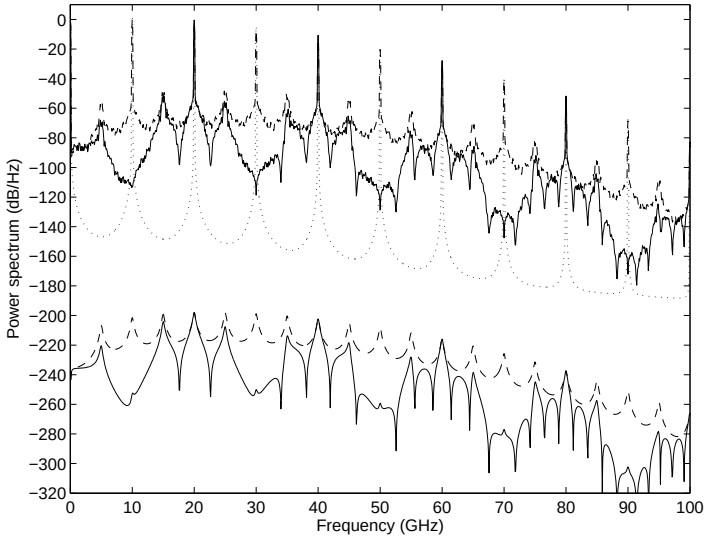

Figure 2.22: *The same as in Figure 2.14 but* $\gamma/\alpha = 1/2$ *which leads* $Q = 0.80$.

consecutive harmonics.

In Figure 2.21 the Talbot index is chosen to be $\gamma/\alpha = 1$. The passbands functions are centered around the harmonics of the signal. However the supermode noise peaks are located at midpoint between two passbands, so that they are completely filtered by the Talbot device. It is worth to compare this figure with figure 2.14. The parameters of both figures are the same, except the jitter spectral noise of the incoming train. We can see the appearance of noise supernoise peaks due to lack of correlation between the timing jitter of consecutive pulses. Figure 2.22 shows the results of the noise spectrum after a fractional Talbot device with index $\gamma/\alpha = 1/2$. The passband functions describing dispersion are now centered at the even harmonics, so that the odd harmonics are filtered and the multiplication rate of the signal is doubled. In this case the supermode noise peaks located between harmonics, are damped but not completely filtered by Talbot devices. This fact is due to the broadening of the passbands with respect to the previous case ($\gamma/\alpha = 1$) weakening the supermode noise filtering. Notice that the damping of these peaks is more efficient for high frequencies, since the modulation helps in narrowing the passbands.

2.3.3 Jitter Smoothing

The integration of the RF noise skirts in a symmetric domain of bandwidth Ω_0 about the hth harmonic is one of the standard operational tools used to obtain experimentally the rms value of the timing jitter of a train from noise analysis of the intensity before it passes through a dispersive line [75]. Since after a fractional Talbot device the spectrum is composed of harmonics multiples of α, we will compute the timing jitter around the $h\alpha$-harmonic of the original train, which enables to compare the jitter before and after the dispersion line. The procedure that permits a simple determination of jitter is to approximate the broadband noise envelope in formula (2.66) by its value in the harmonic and to integrate along a passband of width Ω_0 about the harmonic. This renders the total integrated noise proportional both to squared harmonic index $\alpha^2 h^2$ and to standard deviation σ_j^2 of the

rms jitter:

$$\int_{(\alpha h-1/2)\Omega_0}^{(\alpha h+1/2)\Omega_0} d\omega\ S^{(N)}(\omega,0) \cong \tag{2.75}$$

$$\cong t_0^{-1}\Omega_0^2 h^2\alpha^2|F(h\alpha\Omega_0)|^2 \int_{(\alpha h-1/2)\Omega_0}^{(\alpha h+1/2)\Omega_0} d\omega\ \Phi(\omega)$$

$$= t_0^{-1}\Omega_0^3\alpha^2 h^2|F(\alpha h\Omega_0)|^2\sigma_j^2.$$

Then, from a comparative measurement of different integrated RF noise sidebands, the value of rms jitter is experimentally determined.

As we illustrated in previous sections, the RF noise skirts after a Talbot dispersive line change as a result of to the presence of the passband and the modulation functions. Thus total noise, measured as the result of integration of the noise skirt spectrum along a passband around the harmonics, can get smoothed. Notice that, because of the structure of the noise skirts after the Talbot dispersive line, the output noise cannot be ascribed purely to the timing jitter but a combination of both amplitude and timing jitters in the pulses of the output train. The interpretation of output noise as a specific combination of both amplitude and timing jitters in the pulses of the output train will not be addressed here.

The integrated noise along bandwidth Ω_0 about the hth harmonic of the output signal $(\alpha h\Omega_0)$ after the Talbot dispersive line is expressed as

$$\int_{(\alpha h-1/2)\Omega_0}^{(\alpha h+1/2)\Omega_0} d\omega\ S^{(N)}(\omega,\xi) \tag{2.76}$$

$$\cong t_0^{-1}\Omega_0^2\alpha^2 h^2 J(\alpha h\Omega_0) \int_{(\alpha h-1/2)\Omega_0}^{(\alpha h+1/2)\Omega_0} d\omega\Phi(\omega)G_{n=h\gamma}(\omega)M_{n=h\gamma}(\omega).$$

In formula (2.76) we have also approximated the broadband envelope by its value in the harmonic and have retained in the sum only the passband function that corresponds to the harmonic $\alpha h\Omega_0$, that is, $n = h\gamma$. According to the examples presented in previous sections, this is a good approximation when the dispersive line in adjusted to the first Talbot image, $\gamma = 1$, because no new passbands between harmonics appear in the spectrum. The extension of the integration to a bigger number of passband functions is nevertheless straightforward.

Then the ratio $\rho^{(\alpha h)}$ of the integrated RF noise power after dispersion [formula (2.76)] to that before dispersion [formula (2.75)] is expressed, from formulas (2.62)-(2.66) and (2.60), as

$$\rho^{(\alpha h)} \cong \exp\left(n^2C^2/2Q^2\right) L_{n=h\gamma}(\eta, Q, C), \tag{2.77}$$

where the first term accounts for the different noise envelopes and

$$L_{n=h\gamma}(\eta, Q, C) = \int_{-1/2}^{1/2} dx\ \overline{\Phi}(x)\overline{G}_{n=h\gamma}(x)\overline{M}_{n=h\gamma}(x). \tag{2.78}$$

In Eq. (2.78) we perform the integration by again using the variable $\omega(x) = \Omega_0(\alpha h + x)$ and with the notation $\overline{\Phi}(x) \equiv \Phi[\omega(x)]/\sigma_j^2$, $\overline{G}_{n=h\gamma}(x) \equiv G_{n=h\gamma}[\omega(x)]$, and $\overline{M}_{n=h\gamma}(x) \equiv M_{n=h\gamma}[\omega(x)]$.

From the structure of formula (2.77) the following consequences are derived: First, the ratio in formula (2.77) depends on correlation, not on the precise value of σ_j^2. Second, if pulses are unchirped, noise is essentially symmetric about the harmonic, and the resultant ratio is always less than unity because of the presence of the passband functions. The reduction increases as the width of the passband narrows, so smoothing increases with Q and also as $\eta \rightarrow 0$, because the input noise is white in a bigger band. Finally, when the pulses are chirped the value of the ratio is raised through the exponential factor in formula (2.77) that accounts for the different noise envelopes. This increase becomes bigger at high harmonics.

In Fig. 2.23 we plot the ratio $\rho^{(\alpha h)}$ of the fifth harmonic ($h = 5$) of the first integer Talbot dispersive device ($\gamma/\alpha = 1$) to correlation parameter η and for three values of Q. The values of the ratio [formula (2.77)] were obtained by numerical integration of Eq. (2.78). First, notice that, owing to the quadratic dependence of the integrated noise power formula (2.75)] on the jitters standard deviation σ_j , a reduction of 10 dB in the ratio $\rho^{(\alpha h)}$ amounts to a reduction of σ_j by a factor of 3, whereas a 6-dB decay is associated with a reduction of σ_j by a factor of 2. In Fig. 2.23(a) the ratio is computed for an initial train composed of unchirped pulses, whereas in Fig. 2.23(b) the pulses are slighted chirped ($C = 0.5$ rad). As the correlation parameter controls the white-noise bandwidth of the RF noise skirts of the harmonic, this is one of the most determinant parameters of the smoothing; see Fig. 2.23(a). For high values of η, noise is correlated, the noise skirts are narrow, and consequently the noise reduction induced by the presence of passbands is small. However, when the correlation is low, the presence of the passbands induces a significant decrease in the RF noise skirts, which increases with parameter Q. Chirp is the most deleterious factor for this smoothing. From Figs. 2.17 and 2.18, when pulses are chirped the noise skirts are asymmetric and the peak values are raised above the initial noise level, leading to the increase in the ratio in

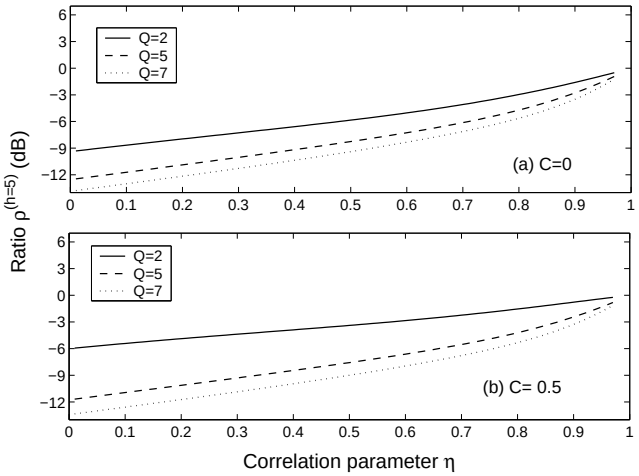

Figure 2.23: *Ratio $\rho^{(h)}$ for the fifth harmonic $h = 5$ (fifth passband, $n = 5$) and for the first integer Talbot replica $\gamma/\alpha = 1$ as a function of correlation parameter η for three values of dispersion parameter Q: continuous curves, $Q = 2$; dashed curves, $Q = 5$; dotted curves $Q = 7$.*

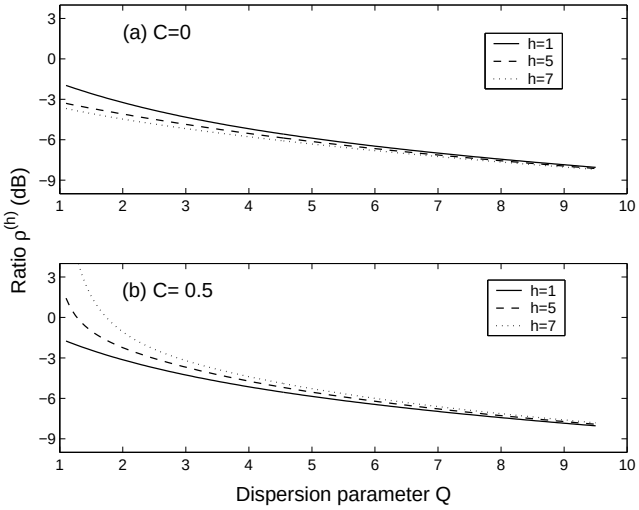

Figure 2.24: *Ratio $\rho^{(h)}$ for the first integer Talbot replica $\gamma/\alpha = 1$ and for jittery trains with correlation parameter $\eta = 0.7$ as a function of dispersion parameter Q for three harmonics h: continuous curves, $h = 1$; dashed curves, $h = 5$; dotted curves $h = 7$.*

formula (2.77) illustrated in Fig. 2.23(b). However, even in the presence of chirp, the combined effect of high Q and low correlation can lead to a significant decrease in the ratio $\rho^{(\alpha h)}$.

To visualize its dependence on the Q factor, and also its small variations within harmonic index h, in Fig. 2.24 we represent again the ratio for the first integer Talbot replica, $\gamma/\alpha = 1$, for jittery trains with correlation parameter $\eta = 0.7$ as a function of Q for different harmonics h and for the same two values of chirp, $C = 0$ and $C = 0.5$ rad. Both the decrease in the ratio $\rho^{(\alpha h)}$ with Q and its small dependence on the harmonic are observed. Again, small chirps in Fig. 2.24(b) spoil the noise reduction. This effect is more pronounced for high harmonics, because the passband shift and the subsequent increase in the noise peak value are proportional to the harmonic frequency. But notice that this increase in ratio $\rho^{(\alpha h)}$ for chirped pulses can be compensated for by means of an increase in Q.

In Figs. 2.25 and 2.26 we represent the ratio $\rho^{(\alpha h)}$ in the second Talbot device, $\gamma/\alpha = 2$. The presence of new passbands between harmonics has been taken into account in the numeral evaluation of integral equation (2.78). In Fig. 2.25 we plot ratio $\rho^{(\alpha h)}$ for the fifth output harmonic, $h = 5$, with respect to the correlation parameter for different values of C and Q. When $C = 0$ rad, the curves in Fig. 2.25(a) are similar to those in Fig. 2.23(a), proving that the ratio depends basically on the value of Q through the width of the passbands located in the harmonic. The presence of new passbands adds a subsidiary contribution to ratio $\rho^{(\alpha h)}$. Therefore the increase in Talbot order produces an increase in the reduction of smoothing. However, when the chirp is nonzero, the subsequent change in the passband position always increases the value of the ratio. In Fig. 2.25(b) the ratio becomes bigger than unity for low values of Q, but, again, increasing the value of Q compensates for the increase in the ratio.

Finally, in Fig. 2.26 we depict the evolution of ratio $\rho^{(\alpha h)}$ for the second integer Talbot replica, $\gamma/\alpha = 2$, for jittery trains with correlation parameter $\eta = 0.7$, as a function of Q for three harmonics h. In Fig. 2.26(a), unchirped pulses are considered. These curves are similar to those of Fig. 2.24(a) except for the first harmonic, $h = 1$, whose values of the reduction are worse because of the presence of the new passband at 5 GHz; Fig. 2.19. In Fig. 2.26(b) we consider pulses with chirp, $C = 0.5$ rad. Again, ratio $\rho^{(\alpha h)}$ increases owing to a shift in the passband maximum and can be compensated for by use of high values of Q.

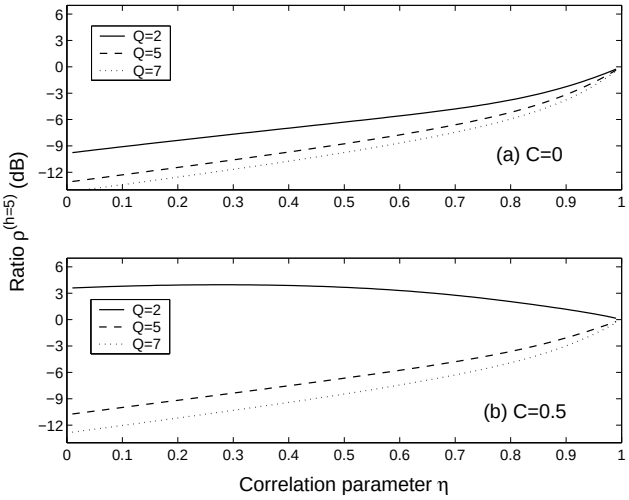

Figure 2.25: *Ratio $\rho^{(h)}$ for the fifth harmonic $h = 5$ (tenth passband, $n = 5$) and for the first integer Talbot replica $\gamma/\alpha = 2$ as a function of correlation parameter η for three values of dispersion parameter Q: continuous curves, $Q = 2$; dashed curves, $Q = 5$; dotted curves $Q = 7$.*

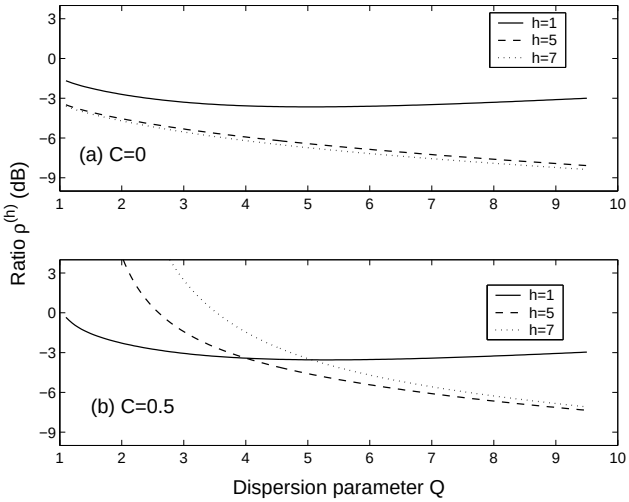

Figure 2.26: *Ratio $\rho^{(h)}$ for the first integer Talbot replica $\gamma/\alpha = 2$ and for jittery trains with correlation parameter $\eta = 0.7$ as a function of dispersion parameter Q for three harmonics h: continuous curves, $h = 1$; dashed curves, $h = 5$; dotted curves $h = 7$.*

2.4 Conclusions

In this chapter we have analyzed the behavior of Talbot lines when they are fed with non-ideal coherent train of linearly chirped Gaussian pulses. We have assumed an ideal Talbot filter, i. e., a pure first-order dispersion medium without attenuation and non linear effects. Furthermore, we considered the bandwidth of Talbot line is large enough to cope with the optical bandwidth of the incoming train.

In section 2.2 we have analyzed the power spectral density of a on-off-keyed train after passing a Talbot filter. We have assumed that the variables describing the presence or absence of pulses in the train are uncorrelated. As a consequence of the coherent interference of dispersed pulses, the microwave spectrum after the detection of the train has a broadband noise envelope that follows the linewidth spectrum of an individual pulse, i.e., the microwave envelope bandwidth is enhanced by the value of the chirp. The basic feature of the spectrum is the presence of passbands filtering this broadband noise, whose centers are shifted with respect to the harmonics due to the chirp of the incident pulses. Measurement of the relative deviation of these centers with respect to passband width allows a determination of the chirps sign and magnitude. The width of the passbands is narrower as the dispersion of the device decreases, the pulse width is shorter, and the chirp is larger. The peak value of these passbands depends on the relative amount of pulses in the train. For small dispersion devices, high passbands, and wide pulses, the passbands show a cosine-squared modulation. The width of this modulation is a fraction of the input harmonic value, being independent of the relative amount of pulses in the train or of the properties of the pulses in the train.

In short, our analysis shows that the parameters describing the pulse train have a neat influence in the resulting microwave spectrum, allowing the indirect characterization of pulse trains through the random Talbot effect. In experimental situations, however, the random Talbot effect has to coexist with other types of broadband and narrowband noise due to the sources or modulators used, such as amplitude noise or timing jitter. For instance, as is well known, the spectrum of detected pulse trains from mode-locked lasers show typical noise skirts around output harmonics, whose width depends on the correlation properties of noise [76–78]. Moreover, deviations of the ideal behavior of the Talbot filter will also affect the characteristics of the spectrum. Although it seems unlikely that the random Talbot effect of pulse trains shows all the fine spectral

details contained in Eq. (2.18) or (2.21), the overall features should be still present. Anyway the noise features of Talbot devices can be enlarged when required by concrete experimental circumstances.

In the section 2.3, we have studied the influence of random jitter of a linearly chirped Gaussian pulses in Talbot devices. The analysis has been performed in the both temporal and spectral domain. In the temporal analysis we have assumed the jitter to be uncorrelated. We have shown that the variance of the train is flattened by use of dispersion after passing a Talbot device. This is due to the dispersion of the individual pulses that form the train, as their variance is spread on neighboring intervals. We have also given approximate formulas for the input and output variances and discussed the validity of these approximations. For integer Talbot devices, the value of the variance is constant irrespective of the value of the dispersion. For fractional Talbot devices with $\gamma/\alpha < 1$, a modulation of the constant value of the variance may be present, depending on the ratio between the pulse width and the period of the original train. Nevertheless, for Talbot devices leading to $N\times$ repetition rates, the variance still is, to a good approximation, constant. The presence of pulse pedestal in these devices has also been analyzed.

From the spectral point of view we report on a wider analysis. Now an arbitrary correlation among jitter variables is allowed. The basic feature of the resultant spectrum is, like in the case of on-off-keyed trains, the presence of a broadband noise-filtering mechanism by multiple interference at the scales of a fraction of the trains repetition rate, which provides a reduction of the integrated noise power around the harmonics as measured in the RF regime. The influence of chirp and optical linewidth of the individual pulses in the train was also analyzed. We have used the results derived to explore the noise reduction of different coherent Talbot-imagined trains under different propagation conditions. The smoothing of jitter noise by Talbot interference depends basically on the chirp of the pulses of the train, on the correlation between adjacent pulses in the train, and on the accumulated dispersion of the line but not on the absolute value of the timing jitters standard deviation. Chirp has been shown to be the most deleterious factor because it induces a shift of the peak noise level with respect to the position of the harmonic that causes an increase in the total noise power. However, careful design of the dispersive line can easily compensate for it [43, 82] and compress the pulses simultaneously, as has been shown in first chapter.

As correlation controls the jitter noise bandwidth before the jitter noise

enters the dispersive line and because jitter smoothing is more pronounced at scales of the order of the repetition rate (typically less than 1 GHz for the 10 GHz trains), the initial noise must be broadband to produce significant jitter reduction. This fact limits the possible application of this procedure to trains composed of slightly correlated pulses. Ultimately, this application depends on the mechanisms that produce the trains. For instance, the use of a Talbot dispersive line cannot be successfully applied in fundamentally mode-locked lasers that have noise offsets up to 100 MHz; see, e.g., Ref. [77]. In this case the active locking in the cavity of the laser produces highly correlated timing jitter. However, even in these cases the Talbot replica of a mode-locked laser output can in principle help to reduce other types of non-narrowband noise, such as the supermode noise [81] in harmonically mode locked lasers, for which both phase noise and timing jitter are uncorrelated between adjacent pulses. [77, 78].

The noise reduction depends on the accumulated dispersion of the line through the order of the Talbot replica. Basically, high Talbot orders imply the appearance of new noise windows between harmonics and the narrowing of the passband widths, which provides the bandwidth of the smoothed spectrum about the harmonics. Except for the first harmonic, the presence of new windows is a subsidiary effect when one is computing the decrease in noise ratio $\rho^{(h)}$. The narrowing of the passbands is controlled by dispersion parameter Q, which accounts for the width of the dispersed pulses relative to the repetition rate of the train. High Q values imply that the resultant pulses in a Talbot replica are formed from contributions of a high number of dispersed pulses, thus providing a coherently averaged output. The same smoothing mechanism has been found in the time domain.

Chapter 3

Partially coherent Temporal Talbot effect

3.1 Introduction

Periodic trains of pulses can be generated by external modulation onto an optical carrier, by the built-in output of a pulsed laser source, or by use of a combination of both procedures. Mode-locked lasers are the preferred sources in the experimental realizations of Talbot devices [23], due to their high coherence and pulse stability, although examples of integer Talbot devices based on phase-modulated cw sources have also been indirectly demonstrated [83]. In either case, the Talbot effect takes place due to the combination of periodicity and coherence in dispersive line.

This chapter deals with the description of the temporal Talbot effect under partial coherence. The authors of Ref. [84] have already addressed this topic, but restricted to integer Talbot propagation and real modulation. Our point of view is more general. The formalism used here describes the effect of dispersive propagation in the average intensity of modulated waves. In particular, it describes Talbot devices with arbitrary pulsed modulation. The description of the influence of partial coherence relies on its identification with a low pass filter acting over the average intensity, allowing an easy identification of the properties of the resulting average intensity patterns.

We also report on a matrix and entropic investigation of the problem. Matrix representations have been extensively used in the coherence theory of scalar monochromatic or polychromatic lightwaves [85, 86]. This representation is particularly suitable in the treatment of self-imaging

effect since first-order dispersive propagation of partially-coherent pulse trains at Talbot distances entails the discretization of the complex degree of coherence. Moreover, the matrix representation permits a simple identification of the number of degrees of freedom that influence the intensity output. The intensity patterns at Talbot distances depend not only on the intrinsic coherence of the carrier wave, but also on the spectral content of the pulsed modulation. These two features are naturally described in matrix form: the first, by a coherence matrix, and the second, by the dimension of the matrix problem. Its diagonalization leads to an interpretation of the average intensity after a Talbot device as an incoherent sum of intensity patterns, whose number and significance is determined by the degree of coherence of the system. The overall degree of coherence of the Talbot device is measured by means of the informational entropy associated to the matrix problem [87, 88]. Furthermore, the entropy is used to evaluate the effective number of uncorrelated random variables that describe the properties of the output pulses under arbitrary partial coherence [89].

The organization of this paper is the following. Section 3.2 is devoted to the introduction of partial coherence in the formalism. The results derived here make use of the classical formalism for treating partially coherent modulated waves in guided linear media [90]. However, we have discussed the coherence properties directly over the electric filed envelope. This point of view provides simpler formulas and makes clear the connection with the natural representation of the space-time analogy [3]. In particular, we introduce in this section the mutual coherence function and derive from it the average intensity of general modulated fields under dispersive propagation, particularizing its form to first-order dispersive systems and identifying the intensity filter representing partial coherence. This representation permits the analysis of the impact of partial coherence over the average intensity in any effect based in the propagation of modulated light after lowest-order dispersion. Section 3.3 is devoted to the study of the temporal Talbot effect under partially coherence, by means of the specialization of the previous formulas to pulse trains. Here we also establish general linewidth requirements for feasible Talbot reconstruction, make connection with the Collett-Wolf theorem, and generalize the results to several incoherent lines. In section 3.4 we introduce the matrix formalism. The entropy of the system as a measure of the degree of coherence of the system as well as the effective number of degrees of freedom of the system are also assessed. All these results are exemplified

with a modulated source with Lorentzian spectrum. Analytical expressions for the entropy, number of degrees of freedom and eigenvalues are also reported in section 3.5. These formulas are valid when the dimension of the matrix problem is sufficiently large. The range of validity of derived expressions is also discussed. Finally, we end in section 3.6 with our conclusions.

3.2 Partially Coherent Light in Dispersive Lines

Let $\psi(t)$ be the analytic signal describing the amplitude of a partially coherent stationary source that emits around a central frequency ν_0. For sake of convenience, we separate the rapid monochromatic oscillation at the carrier frequency $\exp(i2\pi\nu_0 t)$ from the slower amplitude and phase fluctuations of the source $\epsilon(t)$, and represent $\psi(t)$ as:

$$\psi(t) = \epsilon(t)\exp(i2\pi\nu_0 t). \tag{3.1}$$

The second order properties of the stationary filed of the carrier wave are described by the temporal coherence function [3, 91]

$$\langle \epsilon(t)^* \epsilon(t+\tau)\rangle = G(\tau) = I_0 g(\tau), \tag{3.2}$$

where $g(\tau) = g(-\tau)^*$ is the complex degree of temporal coherence, and $I_0 = G(0)$ is the average intensity of the carrier. The power spectral density of the carrier is, using the Wiener-Khinchin theorem, the Fourier transform of the temporal coherence function:

$$S(f) = I_0 \int d\tau g(\tau)\exp(-i2\pi f\tau). \tag{3.3}$$

Notice that, with our definitions, the spectrum of carrier fluctuations at the optical frequency $\nu_0 + f$ is described by the baseband function $S(f)$. The range in integral (3.3) goes form $-\infty$ to $+\infty$, as will be assumed in all sums and integrals along the chapter unless otherwise is stated.

Let $m(t)$ be the function describing the external modulation over $\psi(t)$. Then, the analytic signal $e(t,0)$, that represents the electric field after modulation is given by

$$e(t,0) = m(t)\epsilon(t)\exp(i2\pi\nu_0 t) = a(t,0)\exp(i2\pi\nu_0 t), \tag{3.4}$$

We have introduced the slowly varying optical envelope, $a(t,0)$, which denotes the analytic signal of the electric field at baseband. This form

of introducing the optical envelope is well suited for architectures where cw light from a single mode diode laser is modulated externally. In this case, function $\epsilon(t)$ stands for the phase noise of the cw source [92]. However, (3.4) also describes the output of mode-locked lasers: in this case $\epsilon(t)$ represents global phase noise over the deterministic pulse train $m(t)$ [93].

Let us consider that the electric field (3.4) is propagated along z direction in a linear time-invariant system. Then, after covering a distance z the field will be given by

$$e(t,z) = a(t,z)\exp(i2\pi\nu_0 t - i\beta_0 z), \tag{3.5}$$

where β_0 is the propagation constant evaluated at the central frequency ν_0. Then, the mutual coherence function associated to the electric filed $e(t,z)$ is:

$$\begin{aligned}\Gamma(z,t;z',t') =& \langle e(t,z)^* e(t',z')\rangle \\ &= \langle a(t,z)^* a(t',z')\rangle \exp(i2\pi\nu_0(t'-t) - i\beta_0(z'-z)),\end{aligned} \tag{3.6}$$

and therefore its computation reduces to the calculus of the expected value of envelopes. If the transfer function of the linear system is denoted by $H(f,z)$, it can be shown by direct integration and using Eqs. (3.2)-(3.4), that this factor is a spectrally-weighted superposition of monochromatic modulated fields after dispersive propagation:

$$\langle a(t,z)^* a(t',z')\rangle = \int df\ S(f)\overline{a}(f,t,z,)^*\overline{a}(f,t',z'), \tag{3.7}$$

where:

$$\overline{a}(f,t,z) = \int d\overline{f}\ H(\overline{f},z)M(\overline{f}-f)\exp(i2\pi\overline{f}t) \tag{3.8}$$

is the envelope of the light wave at time t resulting after linear propagation $H(f,z)$ of the initial envelope $a(t,0) = m(t)$ when carried by a monochromatic carrier at frequency $\nu_0 + f$ and with unit amplitude. In this formula, $M(f)$ is the Fourier transform of the modulation function $m(t)$. The mutual coherence function (3.6) can be exactly solved for gaussian single-pulse and pulse-train modulation with gaussian linewidths under lowest-order dispersive propagation and other types of quadratic propagation, see [94–97].

The average intensity of the dispersed wave is recovered from (3.6) by setting $z = z'$ and $t = t'$ [84, 98, 99]:

$$\langle I(t,z)\rangle = \int df\ S(f)|\overline{a}(f,t,z)|^2. \tag{3.9}$$

The average intensity can be further simplified when the linear propagation only involves first-order dispersion, see Eq. (1.19). The modulated envelopes at different frequencies $v_0 + f$ can be expressed in terms of the propagated envelope at $f = 0$, delayed by a quantity $2\pi\beta_2 zf$ proportional to the frequency shift:

$$\overline{a}(f,t,z) = H(f,z)\overline{a}(0,t-2\pi\beta_2 zf,z)\exp(-i2\pi ft). \tag{3.10}$$

Since the transfer function $H(f,z)$ is phase-only, the average intensity (3.9) can be reexpressed as:

$$\langle I(t,z)\rangle = \int df\ S(f)|\overline{a}(0,t-2\pi\beta_2 zf,z)|^2. \tag{3.11}$$

In this formula, $|\overline{a}(0,t-2\pi\beta_2 f,z)|^2$ is the delayed intensity associated to the propagation of the modulated field carried by a monochromatic wave with unit amplitude, $I_u(t-2\pi\beta_2 zf,z)$. Then, Eq. (3.11) can be rewritten as a convolution:

$$\langle I(t,z)\rangle = \int df\ S(f)I_u(t-2\pi\beta_2 zf,z) = s_z(t)\otimes I_u(t,z), \tag{3.12}$$

where the function $s_z(t)$ is the power spectral density of the carrier, scaled by dispersion time domain:

$$s_z(t) = \frac{1}{2\pi|\beta_2|z}S(t/2\pi\beta_2 z). \tag{3.13}$$

Since the optical spectrum of the carrier $S(f)$ is peaked at $f = 0$ (or at $\nu = \nu_0$ in optical frequencies), function $s_z(t)$ in (3.12) acts as a low pass filter that smoothes the average intensity of dispersed modulated light, according to the linewidth of the carrier and the amount of first-order dispersion. If $\Delta\nu$ is a measure of the spectral width of $S(f)$, the average intensity is smoothed in scales $\Delta t = 2\pi|\beta_2|z\Delta\nu$. The coherent limit can be recovered if the spectrum of amplitude and phase variations of the carrier is purely monochromatic, $S(f) = I_0\delta(f)$, so that $s_z(t) = I_0\delta(t)$ and independent of z.

Alternatively, and after (3.13), the transfer function of the low pass filter $s_z(t)$ is:

$$H_S(f) = I_0 g(-2\pi\beta_2 z f) = G(-2\pi\beta_2 z f). \tag{3.14}$$

Let us recall the definitions of the filter's equivalent bandwidth B_{eq} and the carrier's coherence time τ_c:

$$B_{eq} = \frac{1}{|H_S(0)|^2}\int_0^{+\infty} df\ |H_S(f)|^2 \tag{3.15}$$

and

$$\tau_c = \int_{-\infty}^{+\infty} d\tau\ |g(\tau)|^2, \tag{3.16}$$

then, it follows this scaling law:

$$4\pi B_{eq}|\beta_2|z = \tau_c, \tag{3.17}$$

which states that the bandwidth of the low pass intensity filter is directly proportional to the carrier's coherence time and inversely proportional to the accumulated dispersion. This filter can be characterized by spectral analysis of single-tone amplitude or single-sideband modulations [100]. For instance, in the latter case the modulation function associated to a RF angular frequency Ω is:

$$m(t) = 1 + m\exp(i\Omega t), \tag{3.18}$$

where m is the modulation index. Then, the intensity after first-order dispersive propagation is:

$$I_u(t,z) = 1 + m^2 + 2m\cos(\Omega t - \beta_2 z\Omega^2/2), \tag{3.19}$$

and the two-sided Fourier spectrum of the partially coherent average intensity (3.12) is:

$$\begin{aligned} FT\left[\langle I(t,z)\rangle\right] =& I_0(1+m^2)\delta(f) \\ &+ m[\exp(-i\beta_2 z\Omega^2/2)G(-\beta_2 z\Omega)\delta(f-\Omega/2\pi) + hc], \end{aligned} \tag{3.20}$$

where hc stands for the hermitian conjugate. Then, the temporal coherence function can be read as the progressive fading of the RF tone Ω. In the following Section we will analyze the implications of this property when the modulation is pulsed and the propagation length corresponds to fractional or integer Talbot distances.

3.3 Partially Coherent Light in Talbot Lines

In this section we specialize the previous results for a Talbot line. We now consider the partial light source is modulated by a periodic function, so that the optical envelope at the input of dispersive medium, $a(t,0)$ is given by

$$a(t,0) = \epsilon(t)m(t) = \epsilon(t) \left[f(t) \otimes \sum_k \delta(t - kt_0) \right]. \tag{3.21}$$

Then, using (3.12) and (1.32), we obtain the following expression for the average intensity at the Talbot distances $z_{\gamma/\alpha}$, Eq. (1.32):

$$\langle I(t, z_{\gamma/\alpha}) \rangle = \frac{\alpha}{\gamma} \frac{1}{t_0^2} \, S\left(\frac{\alpha}{\gamma} \frac{t}{t_0^2} \right) \otimes |f(t)|^2 \otimes \frac{1}{\alpha} \sum_k \delta(t - \overline{\tau} - kt_0/\alpha). \tag{3.22}$$

This formula can be reduced to the results of [84] when dispersion is specialized to integer Talbot distances ($\alpha = 1$) and $f(t)$ is real. Notice that, according to (3.12), partial coherence results in a smoothing of the average intensity, irrespectively of the exact or approximated character of the (monochromatic) temporal Talbot effect due to pulse overlapping. If, however, the initial pulses are sufficiently narrow to avoid overlapping at the Talbot distance under consideration, the coherent intensity train is exactly periodic with period t_0/α see Eq. (1.32). Then, formula (3.22) describes the smoothing of the average intensity profile in each exact period t_0/α due to partial coherence.

Formula (3.22) also describes an example of the temporal Collett-Wolf theorem [13, 14]. This result states that two optical modulated light fields with different coherence properties may propagate in dispersive media with identical average intensity distribution. In our case, it is apparent from (3.22) that, given a Talbot distance $z_{\gamma/\alpha}$, a pulse train carried by a monochromatic wave of intensity I_0, and with single pulse profile $q(t)$ would provide the same average intensity of a train of pulses $f(t)$ carried by a partially coherent wave if:

$$\frac{\alpha}{\gamma} \frac{1}{t_0^2} \, S\left(\frac{\alpha}{\gamma} \frac{t}{t_0^2} \right) \otimes |f(t)|^2 = I_0 |q(t)|^2. \tag{3.23}$$

The dual behavior of single-pulse intensity and spectral content becomes clear through this convolution. Equivalently, partial coherence can be interpreted as defining the low pass filter (3.13). The equivalent bandwidth (3.15) of the filter at Talbot distances $z_{\gamma/\alpha}$ is:

$$B_{eq} = \frac{1}{2}\frac{\tau_c}{t_0^2}\frac{\alpha}{\gamma}, \tag{3.24}$$

Notice that the bandwidth increases with the inverse of the Talbot index γ/α. This means that, for the same type of pulses, coherence requirements are more restrictive for high values of the Talbot index γ/α and that, for a given value of the repetition rate α, the increase of γ smoothes the average intensity of the Talbot-imagined train. In the time domain, this observation can be interpreted as follows. The process of reconstruction of pulses at Talbot distances is multiple pulse-to-pulse interference due to dispersion. Partial coherence damps the interference pattern between neighboring pulses, since the underlying carrier misses progressively its own phase. This damping is more pronounced when the interfering pulses are initially more distant. Therefore, high values of the Talbot index γ/α, or, alternatively, highly dispersive devices, which require constructive interference between pulses that were initially more distant, are more sensitive to the coherence of the carrier.

Formula (3.24) can also be used to determine coherence requirements for the recovery of the Talbot train of intensities. Since this train is composed of intensity harmonics of the fundamental frequency $1/t_0$, the quantity $B_{eq}t_0$ represents the number of harmonics that are not filtered by partial coherence. The requirement of faithful reconstruction of the pulses is therefore $B_{eq}t_0 \gg 1$. For instance, a typical DFB laser has a spectral line with FWHM of 50 MHz. Its coherence time is therefore $\tau_c \sim 20$ ns. If, moreover, the repetition rate is 2.5 GHz ($t_0 = 400$ ps), and $\gamma/\alpha = 1/4$, the resulting relative bandwidth is $B_{eq}t_0 = 32$.

On the other hand, the quantity $B_{eq}t_0/\alpha$, which represents the number of intensity harmonics that constitute the output train, does not depend on the repetition-rate index α: $B_{eq}t_0/\alpha = \tau_c/2t_0$. This is a consequence of the inverse relationship between equivalent bandwidth and dispersion: lower dispersion -or, equivalently, higher repetition-rate index implies higher bandwidth or a less severe smoothing of the single-pulse intensity, see (3.24). But the increase in index α also implies the increase in the separation α/t_0 of the intensity harmonics that conform the output train, so that the total number of the output intensity harmonics is independent of α. In fact, $B_{eq}t_0/\alpha$ is a measure of the coherence time relative to the period of the train.

This conclusion can also be obtained by direct computation. Let us consider the harmonic expansion of the initial intensity train:

$$|f(t)|^2 \otimes \sum_k \delta(t - kt_0) = \sum_k C_k \exp(i2\pi kt/t_0), \tag{3.25}$$

where C_k are the harmonics of the periodic modulation function. Then, the corresponding expansion of the coherent output train with increased repetition rate only involves the harmonics multiples of α:

$$|f(t)|^2 \otimes \frac{1}{\alpha} \sum_k \delta(t - \overline{\tau} - kt_0/\alpha) = \sum_k C_{k\alpha} \exp(i2\pi k(t - \overline{\tau})\alpha/t_0). \tag{3.26}$$

If we insert this expansion in (3.22) to take into account the partial coherence of the carrier wave, we obtain:

$$\langle I(t, z_{\gamma/\alpha}) \rangle = \sum_k C_k G(-kt_0\gamma) \exp(i2\pi k(t - \overline{\tau})\alpha/t_0), \tag{3.27}$$

which shows that coherence limits the number of output intensity harmonics independently of the repetition-rate index α.

Finally, we conclude the analysis of formula (3.22) with the description of its generalization to multiple carrier wavelengths [99, 101]. Let us assume that the carrier is composed of N independent partially-coherent wavelengths. Let us also assume that the detection conditions assure that the corresponding modulated waves are mutually incoherent, so that the final average intensity is a sum of the intensities associated to different wavelengths but with the same modulation. Then, the filter in (3.22) generalizes to a sum over the different spectral lines:

$$\langle I(t, z_{\gamma/\alpha}) \rangle = \frac{\alpha}{\gamma} \frac{1}{t_0^2} \sum_{k=1}^{N} S_k \left(\frac{\alpha}{\gamma} \frac{t}{t_0^2} \right) \otimes |f(t)|^2 \otimes \frac{1}{\alpha} \sum_m \delta(t - \overline{\tau} - mt_0/\alpha). \tag{3.28}$$

and thus the spectral content of the carrier waves determines the filter's temporal response. In this sum, frequency shifts between different carriers translate into time delays. For instance, let us assume that the modulation is carried by two monochromatic waves with different intensities and frequencies ν_0 and $\nu_0 + \Delta\nu_0$, respectively. Then, the sum in Eq. (3.28) contains two terms, associated to the power spectral densities $S_1(f) = I_0\delta(f)$ and $S_2 = I_0'\delta(f - \Delta\nu_0)$. The resulting filter is:

$$\frac{\alpha}{\gamma} \frac{1}{t_0^2} \sum_{k=1}^{2} S_k \left(\frac{\alpha}{\gamma} \frac{t}{t_0^2} \right) = I_0\delta(t) + I_0'\delta(t - \frac{\gamma}{\alpha} t_0^2 \Delta\nu_0), \tag{3.29}$$

thus describing a weighted superposition of two replicas of the signal, with a mutual delay that depends on the frequency difference $\Delta\nu_0$. A mapping of this type -from the spectral content of the carrier to a delay in the modulated waveforms- finds application in the construction of microwave transversal filters [102]. In formula (3.28), however, the filter acts over pulses created as Talbot replicas of the original train. Therefore, the wavelength-dependent delay introduces a relative delay between Talbot-imagined trains, not between replicas of a dispersed train, as in (3.12). This observation represents the basis of the temporal Lau effect.

3.4 Matrix Theory and Entropy

The first objective of this section is to express the output intensity of a Talbot device in a matrix form, separating the influence of partial coherence and the spectral content of the incoming train of pulses. To this end, we observe that the harmonics $C_{\alpha k}$ of the coherent output intensity in eq. (3.26) can be expressed in terms of the amplitude α-harmonics $a_{\alpha k}$:

$$C_{\alpha k} = \alpha \sum_r a_{r\alpha} a^*_{(r-k)\alpha}. \tag{3.30}$$

This can be derived from (3.26), since the absence of pulse overlapping leads to the following equality:

$$\begin{aligned} I_u(t, z_{\gamma/\alpha}) &= \left| \frac{f(t)}{\sqrt{\alpha}} \otimes \sum_k \delta(t - \overline{\tau} - kt_0/\alpha) \right|^2 \\ &= \left| \sqrt{\alpha} \sum_s a_{\alpha s} \exp[i2\pi\alpha s(t - \overline{\tau})/t_0] \right|^2 . \end{aligned} \tag{3.31}$$

On the other hand, in Eq. (3.27) we observe that the Talbot effect involves the sampling of the complex coherence function with sampling period $t_s = \gamma t_0$. This permits the description of the influence of partial coherence in a matrix way. For this purpose, we define the coherence matrix $\mathbf{M}$ with elements:

$$M_{rs} = M^*_{sr} = g(\gamma(r - s)t_0). \tag{3.32}$$

The properties of the complex degree of coherence imply that the coherence matrix is a Hermitian Toelplitz matrix [103, 104]. We also define a time-

dependent column vector $\mathbf{A}$ whose entries are given by:

$$A_r(t) = a_{r\alpha} \exp(i2\pi\alpha r t/t_0), \tag{3.33}$$

which corresponds to the α-harmonics of the incoming optical envelope. From now on, we will assume that $N = 2n+1$ is the number of α-harmonics describing the input pulse train, so that the indices in (3.32) and (3.33) run from $-n$ to n. If the spectral content of the input pulses, $f(t)$, is contained in a band $[-W_p, W_p]$ around the optical carrier, then:

$$n = \lfloor W_p T/\alpha \rfloor, \tag{3.34}$$

and $\lfloor x \rfloor$ is the largest integer smaller or equal to x. Using these definitions, the average intensity (3.27) can be rewritten as:

$$\langle I(t, z_{\gamma/\alpha}) \rangle = I_0 \alpha \mathbf{A}^+(t-\overline{\tau}) \cdot \mathbf{M} \cdot \mathbf{A}(t-\overline{\tau}), \tag{3.35}$$

where $\mathbf{A}^+$ is the Hermitian conjugate of vector $\mathbf{A}$. Specializing this expression for $t = \overline{\tau}$ it follows that $\mathbf{M}$ is a positive-definite matrix, since in this case $\mathbf{A}$ is an arbitrary time-independent vector and the intensity is clearly a non-negative quantity.

The coherence matrix is a Hermitian operator and therefore diagonalisable by means of a transformation matrix $\mathbf{B}$:

$$diag(\lambda_1, \lambda_2, \cdots, \lambda_N) = \frac{1}{N}\, \mathbf{B} \cdot \mathbf{M} \cdot \mathbf{B}^+, \tag{3.36}$$

where λ_r represent its eigenvalues and the factor $1/N$ has been introduced in order to normalize the trace of the diagonal matrix to unity. Since the coherence matrix is positive semi-definite, its eigenvalues are nonnegative [103]. With this decomposition the average intensity is:

$$\langle I(t, z_{\gamma/\alpha}) \rangle = I_0 N \alpha \sum_{r=-n}^{n} \lambda_r |b_r(t-\overline{\tau})|^2, \tag{3.37}$$

where:

$$b_r(t) = \sum_{q=-n}^{n} B_{rq} a_{\alpha q} \exp(i2\pi\alpha q t/t_0). \tag{3.38}$$

Eq. (3.37) represents the average intensity at Talbot distances as a weighted sum of intensity patterns, $|b_r(t-\overline{\tau})|^2$, the eigenvalues λ_r being the weights of the sum. Thus, the average intensity can be reinterpreted as an incoherent sum of amplitude patterns $b_r(t-\overline{\tau})$ whose number and relative intensity is

determined by the eigenvalues λ_r [85, 86].

In the coherent limit the coherence matrix is unity $M_{rs} = 1$, $\forall r, s$, and there is a single eigenvalue different form zero, $\lambda_K = 1$ for certain index K. The corresponding eigenvector is $B_{Kq} = 1/\sqrt{N}$ $\forall q$, so that the only significant amplitude $b_K(t)$ represents the amplitude of the train of pulses with increased repetition rate under total coherence. On the other hand, the incoherent limit is represented by a coherence matrix $M_{rs} = \delta_{rs}$. In this case all eigenvalues are equal to $1/N$, and therefore all patterns in the sum (3.37) are equally weighted. The matrix of eigenvectors is $B_{rq} = \delta_{rq}$, and the intensity is constant in the incoherent limit. Therefore, the form of the amplitude patterns $b_r(t)$ is a linear combination of the α-harmonics of the train that interpolates between total coherence and incoherence conditions.

On the other hand, the number and relative magnitude of the eigenvalues enclose the influence of partial coherence in the performance of the temporal Talbot effect. In Appendix B we review several parameters that have been introduced as a measure of the partial coherence in similar matrix decompositions of partially-coherent optical effects from its eigenvalue decomposition [87, 88]. These can also be used to measure the overall impact of partial coherence in the intensity patterns arising at Talbot distances. Among them, we will focus on the informational entropy [85]:

$$H = -\sum_{k=-n}^{n} \lambda_k \ln \lambda_k. \tag{3.39}$$

The entropy ranges from its minimum value $H_{min} = H_{coh} = 0$ that represents total coherence; and its maximum, $H_{max} = H_{incoh} = \ln N$, which corresponds to the incoherent limit.

A somewhat similar measure of the coherence is the effective number N_{eff} of uncorrelated random variables that represent a signal [89]. In our context this number is an equivalent measure of the number of significant non-zero eigenvalues that contribute to the expansion of the intensity (3.37). Since this expansion can be interpreted as the incoherent sum of the intensities associated to N different sources [86], we refer to N_{eff} as an effective number of incoherent sources.

Let us identify this expansion with an equivalent expansion associated to the intensity recorded at a certain Talbot distance with exactly $N_{eff} \leq N$ uncorrelated, equally-weighted sources, so that the entropy of this equivalent system would be $H = \ln N_{eff}$. Then, given a Talbot device operating under partial coherence with entropy H, we define the number

of effective sources as:

$$N_{eff} = \lceil \exp(H) \rceil, \tag{3.40}$$

where $\lceil x \rceil$ represents the minimum integer larger than x. The relation of this quantity with those introduced in [87–89] is also briefly reviewed in Appendix B.

In order to present examples of the use of the expansion in eigenvalues (3.37) we consider Talbot devices fed by partially-coherent trains with a Lorentzian carrier linewidth, whose complex degree of coherence is an exponential function [3]:

$$g(\tau) = \exp(-|\tau|/\tau_C), \tag{3.41}$$

where τ_C is the coherence time. Let us consider a modulation signal with period $t_0 = 1$ ns, described by 201 harmonics, which feeds a Talbot device with index $\gamma/\alpha = 1/2$. From Eqs. (3.27) and (3.30), only those harmonics multiples of $\alpha = 2$ have influence over the value of the average output intensity. Therefore, the output intensity is described by a coherence matrix with dimension $N \times N = 101 \times 101$. The ordered eigenvalues of this system ($\lambda_1 \geq \lambda_2 \geq \ldots$) are presented in figure 3.1. On its left hand side, the largest ten eigenvalues of the coherence matrix are depicted for different values of the coherence time. The eigenvalues of a partially coherent source with $\tau_C = 100$ ns are depicted by squares. Each pulse in the original train is able to interfere with the nearest $2\tau_C/t_0 = 200$ initial pulses, so that we expect that the output train is composed of faithful replicas of the initial pulses. The value of the entropy has increased from its value in the coherent limit but it is still far from its maximum value. If the temporal coherence is reduced up to 10 ns (circles) or 3 ns (triangles-down), pulses in the initial train can interfere only with the nearest 20 or 6 pulses, respectively. This leads to a progressive equalization of the magnitude of the eigenvalues. Correspondingly, the entropy is increased. Finally, for $\tau_C = 1$ ns (triangles-up) we almost reach the incoherent limit, since each pulse can interfere with only their two neighbours. The entropy is close to its maximum value and the eigenvalues almost have the same magnitude.

On the right hand side of figure 3.1, we depict the evolution of the two largest eigenvalues (λ_1, λ_2), together with the tenth (λ_{10}) and lowest (λ_{101}) eigenvalue, with respect to the coherence time. Their behavior is equivalent to the previous plot: the relative importance of the main eigenvalue decreases with the coherence time. When all eigenvalues are equally weighted with $\lambda_r \sim 1/N = 1/101 \sim 0.01$ we reach the incoherent limit. In this case, this happens for coherence times of about $\tau_C \sim 100$ ps.

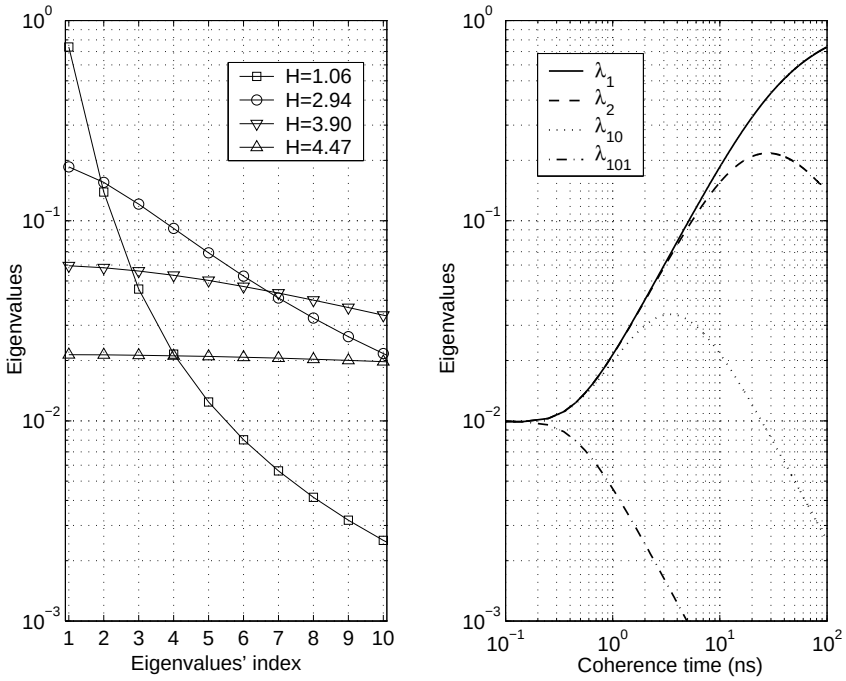

Figure 3.1: *Left hand side: the ten higher eigenvalues of coherence matrix associated to different coherence times:* $\tau_c = 100$ *ns (squares),* $\tau_c = 10$ *ns (circles),* $\tau_c = 3$ *ns (triangles-down) and* $\tau_c = 1$ *ns (triangles-up). Right hand side: evolution of the eigenvalues* λ_1*,* λ_2*,* λ_{10} *and* λ_{101} *as a function of the coherence time. The parameters of the Talbot device are* $t_0 = 1$ *ns, N=101, and* $\gamma/\alpha = 1/2$*.*

In figure 3.2 we exemplify the influence of partial coherence in the output average intensity. We also explore the effective number of sources and their ability to reconstruct the output by truncation of expansion (3.37). In this plot we represent the output average intensity that results after taking into account all eigenvalues in (3.37) (continuous line) and the truncation to N_{eff} eigenvalues (dashed line), for different values of the coherence time. The initial train is composed of Gaussian pulses of $\tau_P = 50$ ps width (measured as the half-width at $1/e$ decay in power) and period $t_0 = 1$ ns. It is propagated through a Talbot device with index $\gamma/\alpha = 1/2$. In spite of the fact that a Gaussian pulse train is composed of an infinite collection of harmonics, we will assume that the set of harmonics with

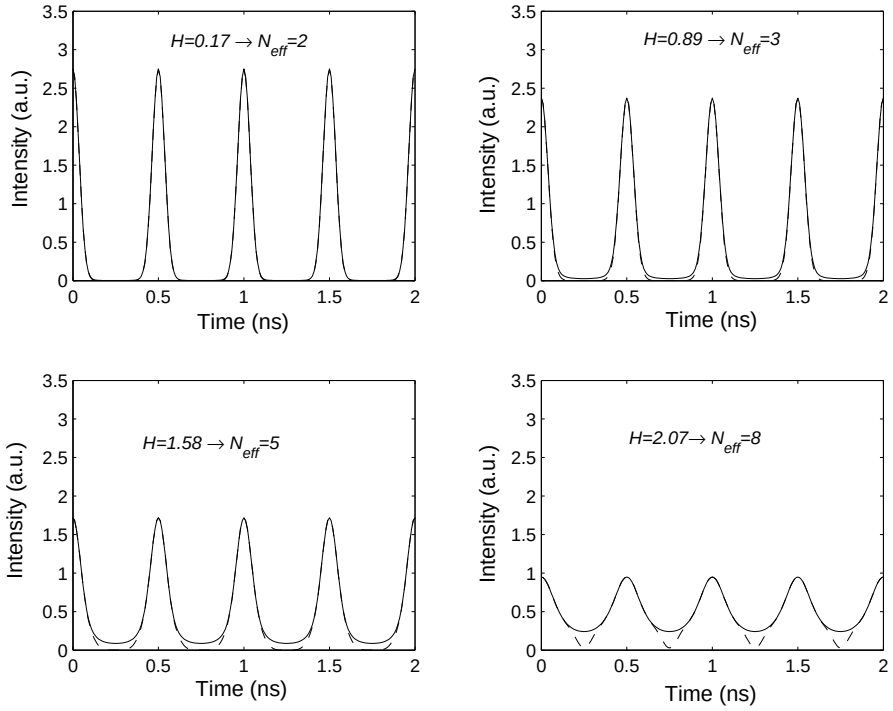

Figure 3.2: *Average intensity of a 1GHz train of 50 ps Gaussian pulses after propagation along a $\gamma/\alpha = 1/2$-Talbot device. Continuous curve: exact average intensity. Dashed curve: approximate average intensity after truncation to N_{eff} sources.*

power above -30 dB the maximum describes acceptably the train. Under this criterion and taking into account (3.34) the dimension of the matrix problem $N = 2n + 1$ is determined by

$$n = \lfloor \frac{0.419}{\tau_P} \frac{t_0}{\alpha} \rfloor, \tag{3.42}$$

which in this example leads to $N = 9$. Note that this truncation of the number of harmonics does not assure that the initial pulses are time-limited to the interval $[0, t_0/2]$, as required for exact increase of the train's repetition rate, but will be sufficient to describe the effect of partial coherence.

In figure 3.2(a) we present an example of a highly coherent carrier with $\tau_C = 100$ ns. The effective number of sources is two. The curve depicted by

considering two sources is indistinguishable form the exact intensity output. We have also checked that the intensity associated to a coherent carrier is indistinguishable from those depicted here. In figure 3.2(b) we consider a carrier with $\tau_C = 10$ ns, which is the second example in our previous figure 3.1. In the exact partially-coherent intensity pattern we observe the progressive smoothing of the intensity pattern, as expected. On the other hand, the effective number of sources is now 3, and the resulting average intensity after truncating the expansion (3.37) is still in good agreement with its numerical value.

In figures 3.2(c) and (d) the coherence time of the carrier are 3 ns and 1 ns, so that the effective number of sources increases to 5 and 8, respectively. We observe the progressive fading of the output pulse train, which tends to a constant value in the incoherent limit. We also notice that the accuracy of the truncation by N_{eff} effective incoherent sources decreases when sources become less coherent. This is due to the fact that the relative importance of the first neglected eigenvalue in the expansion, with index $k = N_{eff} + 1$, with respect to the previous one, with $k = N_{eff}$, tends to unity in the incoherent limit. Therefore, the truncation of the intensity expansion by the effective number of sources provides a good approximation of the average intensity as long as the coherence of the source is not extremely low. In general, it is necessary to use sources with high phase and amplitude stability to achieve a coherent phenomenon such as the Talbot effect, and therefore the approximation of expansion (3.37) by truncation to N_{eff} terms is valid in practice.

3.5 Entropy in the Limit of Large N

The application of the temporal Talbot effect to multiplying the repetition rate of pulse trains requires the absence of pulse overlapping in the output, or equivalently, narrow initial pulses. The description of narrow pulses requires a large number N, which is the number of α-harmonics in the train and also the dimension of the coherence matrix. Fortunately, the properties of Toeplitz matrices in the limit of large N are well understood. They are based on Szegö theorem on the distribution of eigenvalues [104], which states that:

$$\lim_{N\to\infty} \sum_{k=1}^{N} F\left(\tau_k^{(N)}\right) = \int_{-\pi}^{+\pi} \frac{d\Omega}{2\pi} F\left[P(\Omega)\right]. \tag{3.43}$$

$\tau_k^{(N)}$ stands for the eigenvalues of a $N \times N$ square or absolutely summable Hermitian Toeplitz matrix, F represents any continuous function and

$$P(\Omega) = \sum_k M_k e^{-ik\Omega} \tag{3.44}$$

is the discrete Fourier transform (DFT) of the elements of the Toeplitz matrix, $M_k = M_{r+k,r}$, for any r. In our case we apply this result to the series of coherence matrix $\mathbf{M}$ of order $N \times N$, so that $M_k = g(kt_0\gamma)$ and the normalized eigenvalues λ_k in (3.36) are related to those in (3.43) by $\lambda_k = \tau_k^{(N)}/N$. The most common coherence functions $g(\tau)$ (lorentzian, gaussian or rectangular) yield square and absolutely summable matrices, thus justifying the application of the result.

The application of (3.43) to the coherence matrix also provides an interpretation for function $P(\Omega)$. The elements in the DFT (3.44) are the samples of the coherence function $g(\tau)$ with sampling period $t_s = \gamma t_0$. If, moreover, this function is bandlimited to W_C and the sampling frequency is larger than the Nyquist rate, $1/\gamma t_0 \geq 2W_C$, according to the sampling theorem the DFT (3.44) is a rescaled version of the Fourier transform $g(t)$, which is $S(f)/I_0$:

$$P(\Omega) = \frac{1}{I_0 \gamma t_0} S(\Omega/2\pi\gamma t_0). \tag{3.45}$$

On the other hand, the study of Toeplitz matrices, and, in particular, Szegö theorem (3.43) is derived from the asymptotical equivalence of Toeplitz matrices and the (technically simpler) circulant matrices [104]. For instance, there is a closed formula for the eigenvalues of circulant matrices in terms of $P(\Omega)$, which will be used here as an approximation of the eigenvalues λ_k:

$$\lambda_k \cong \frac{1}{N} P(2\pi k/N) = \frac{1}{I_0 \gamma t_0 N} S(k/\gamma t_0 N) \tag{3.46}$$

for $k = -n, \ldots, n$, and where the second equality follows from (3.45).

Let us apply these results to the study of Talbot devices operated with partially-coherent pulsed sources with Lorentzian linewidth. In this case the spectrum $S(f)$ is not bandlimited, so that (3.45) does not hold. However, function $P(\Omega)$ can be computed from its definition (3.44), the result being:

$$P(\Omega) = \frac{1 - a^2}{1 + a^2 - 2a\cos(\Omega)}, \tag{3.47}$$

where $a = \exp(-\gamma t_0/\tau_C)$. The result that would be obtained from (3.45) is equivalent to the Lorentzian approximation to (3.47) in the limit of large

τ_C, which in this case stands for the limit of finite spectral width. According to (3.46), the eigenvalues can be approximated by:

$$\lambda_k = \frac{1}{N}\frac{1-a^2}{1+a^2-2a\cos(2\pi k/N)}, \tag{3.48}$$

Note that with this notation the eigenvalues are not arranged in decreasing order. Since the eigenvalues have to be between zero and unity, N must be higher than $(1+a)/(1-a)$ for the analytical expression (3.48) to be valid, so that the condition $N \gg (1+a)/(1-a) = \coth(\gamma t_0/2\tau_C)$ determines the limit of large N. This limit can be interpreted from definition (3.34) and the fact that the spectral width of the pulses is inversely proportional to the pulse width, $\tau_P \sim 1/W_P$. Then, the large N limit represents a limit over the pulse's temporal width:

$$\tau_P \ll \frac{t_0}{\alpha}\tanh\frac{\gamma t_0}{2\tau_C}. \tag{3.49}$$

In the incoherent limit, this condition requires that $\tau_P \ll t_0\alpha$, which is simply the condition of absence of pulse overlapping. On the other hand, the limit of high coherence $\tau_C \gg \gamma t_0/2$ implies a more stringent bound, $\tau_P \ll \gamma t_0^2/2\alpha\tau_C \ll t_0/\alpha$.

Szegö theorem also provides an approximate expression for the entropy (3.39). By setting $F(x) = x\ln(x)$ and using the relation $\lambda_k = \tau_k^{(N)}/N$, eq. (3.43) yields:

$$\lim_{N\to\infty}\left[H_N - \ln N\right] = \int_{-\pi}^{\pi}\frac{d\Omega}{2\pi}P(\Omega)\ln[P(\Omega)]. \tag{3.50}$$

In this formula the approximation to the value of the entropy H_N is measured with respect to the entropy of an incoherent source. After direct integration we get:

$$H_N \cong \ln\left[N(1-a^2)\right] \tag{3.51}$$

and

$$N_{eff} = \lceil N(1-a^2)\rceil \tag{3.52}$$

The values of entropy in the limit of large N are within the range $[0, \ln N]$, tallying with the results of the previous section. The analytical and numerical values of the eigenvalues, as well as the reconstruction of the average intensity are compared in figure 3.3. Let us consider a laser source whose spectral density is described by the Lorentzian model with coherence time of 10 ns. The modulation function is a 1 GHz-train of Gaussian pulses

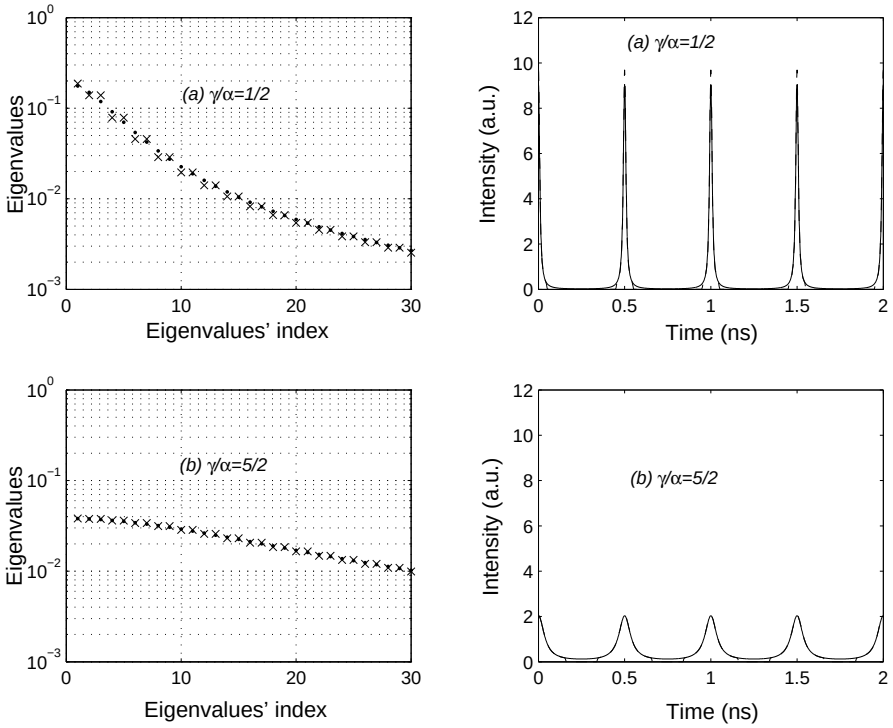

Figure 3.3: *The eigenvalues (left) and the average intensity (right) of a* 1 *GHz-train of Gaussian pulses,* 4 *ps-width after a Talbot device with index (a)* $\gamma/\alpha = 1/2$*, and (b)* $\gamma/\alpha = 5/2$*. The other parameters of the system are* $\tau_C = 10$ *ns, and* $N = 107$*.*

whose half-width at 1/e decay in power is 4 ps. Figure 3.3(a) represents the results for a 1/2-Talbot device whereas figure 3.3(b) refers to a 5/2-Talbot device. The analytical form of the eigenvalues (3.48) is only valid in the limit of large N, which in this cases requires $\tau_P \ll 83$ ps ($N \gg 7$) for the 1/2-Talbot device and $\tau_P \ll 231$ ps ($N \gg 3$) for the 5/2-Talbot device. From eq. (3.42) the dimension of the matrix problem is in both examples $N = 2n+1 = 107$, laying within the range in which above derived expressions are valid.

On the left side of figure 3.3 we present the eigenvalues obtained by the analytical expression (3.48) (crosses) and by diagonalizing the coherence matrix (dots). The values of the entropy from eq. (3.51) are 2.97 (1/2 Talbot) and 4.21 (5/2 Talbot), and are in quite good agreement with the

numerical results, 3.00 and 4.22 respectively. Notice that the entropy of the system increases with the index γ. Thus, the coherence requirements for the incoming signal are more exacting for Talbot devices operating with $\gamma > 1$. This can be observed by comparison of the figures on the right hand side. In these figures the average intensity after the Talbot device, taking into account all numerical eigenvalues is represented using a continuous curve, whereas the dashed curve is the intensity computed with N_{eff} eigenvalues: $N_{eff} = 21$ and 68 for the 1/2-Talbot and 5/2-Talbot devices, respectively. The figure makes clear the validity of the analytical expression in the limit of large N and the approximation of the average intensity profile to N_{eff} sources.

3.6 Conclusions

We have presented the formulas that describe the average intensity of the dispersive propagation of a partially coherent and modulated guided wave. The result, when specialized to lowest-order dispersive media, admit a representation as a convolution. The partial coherent carrier of the modulated wave is thus a low pass filter acting over the average intensity associated to a monochromatic carrier. We have subsequently applied this point of view to the characterization of the partially coherent temporal Talbot effect, where the modulated waves are pulse trains. The analysis shows that coherence limitations are more restrictive when the device requires high dispersion, since the carrier needs more coherence time to produce faithful pulse-to-pulse interference. Increasing dispersion, or decreasing the coherence time, results in a progressive decrease of the filter's bandwidth and, therefore, in a loss of the low-time-scale details when compared with the intensity obtained with a monochromatic carrier. Generalizations of the theory to several spectral lines, and its relation with the Collett-Wolf theorem have also been presented.

A matrix analysis of the Talbot effect under partial coherence has also been presented. The self-imaging effect entails the discretization of the complex degree of coherence associated to amplitude and phase variations of the deterministic modulated lightwave. The matrix problem representing the average intensity at Talbot distances has been diagonalized, so that it can be interpreted as an incoherent sum of intensity patterns. From this representation we have computed the informational entropy and the number of effective sources as measures of the overall performance of the temporal Talbot effect under partial coherence. The truncation of the incoherent sum

to the number of effective sources provides simpler but accurate formulas for the determination of the average intensity. Furthermore, analytical expressions for entropy and eigenvalues have been presented in the limit of large N, by use of the Szegö theorem.

Conclusions

From the spectral point of view, a Talbot line is a multiple bandpass filter, where each passband represents the interference between dispersed pulses separated a certain number of time slots. Thus, fractional Talbot lines, act filtering the intensity harmonics of the input train which do not belong to the output, leading to an increase of the repetition rate of the train. The rejection is exact only for transform-limited pulses and semi-integer Talbot devices with negligible second-order dispersion. Talbot filters are not static but depend on the dispersive characteristics of the line as well as the bandwidth of the input train. In the particular case of linearly chirped Gaussian pulse train, we have derived the conditions which guarantee that the Talbot device provides an output train with negligible intensity fluctuations, even in presence of second order dispersion. However, in this case, the output train may suffer from single pulse distortion.

The stability and the tolerance of Talbot filters under timing and length variations have been studied. If input trains have large bandwidth, small dispersion variations lead to notable broadening of pulses, worsening the performance of Talbot line by pulse-to-pulse interference. Nevertheless, when spectral width is moderate, dispersion instabilities deteriorate the rejection capability of the filter. Input Trains with a bandwidth measured as FWHM equals to twice the the repetition-rate of the output train yields to the optimal stability. The tolerance length are expected to be about 10% divided by the repetition-rate factor.

We also have explored Talbot devices as smoothers of imperfections of the input signal. In particular, we have first studied randomly on-off keying of the pulses in the train, and then timing jittery trains before and after passing through a Talbot line. We have assumed pulses to be linearly chirped Gaussian. In both cases the basic feature of the spectrum is the presence of passbands which filter the broadband noise. If pulse are unchirped the passbands are centered in the harmonics of the perfect train, otherwise their centers are slightly shifted. Measurement of the

relative deviation of this centers with respect to the passband width allows a determination of the chirp's sign and magnitude. Passbands present a modulation, which increases in frequency along the RF spectrum.

The timing jittery noise reduction has been analyzed from the variance and by the integration of the RF noise skirt about the harmonics. When jitter variables are uncorrelated, the variance of the train after passing Talbot device is flattened, becoming time-independent. It leads to the smoothing of the timing jitter but also to the appearance of pulse pedestal. The same result is achieved by means of RF noise integration. However when pulse jitter is correlated, the noise reduction is less significative. It is easy understood from the RF spectrum. In this case, jitter noise is narrowband around the harmonics and consequently the noise reduction induced by the presence of passbands is smaller. Chirp has been shown to be the most deleterious factor because it induces a shift of the peak noise level with respect to the position of the harmonic that causes an increase in the total noise power.

The influence of the source coherence in Talbot devices has been analyzed. The partial coherent carrier of the modulated wave after propagation along a lowest-order dispersion medium is as a low pass filter acting over the average intensity associated to a monochromatic carrier. Under Talbot conditions, the coherence limitations are more restrictive for high dispersive lines, i.e, high Talbot index, since longer coherence time is need to produce faithfull pulse-to-pulse interference. Increasing dispersion or decreasing the coherence time results in a progressive decrease of the filter's bandwidth and therefore, in loss of the low-time scale details when compared with the intensity obtained with a monochromatic carrier. We also approach the Talbot effect under partial coherence from a matrix point of view. The diagonalization of the matrix problem representing the average intensity after Talbot device yields to the interpretation of the average intensity as an incoherent sum of intensity patterns. In this context, we have computed the informational entropy and the number of effective sources as measures of the overall performance of the Talbot device.

Appendix A

Let be define the functions $f_1(t)$ and $f_2(t)$, from the arbitrary function $f(t)$ as:

$$f_1(t) = f(t)\exp(2\pi ist/t_0) \otimes \sum_m \delta(t - mt_0/\alpha) \tag{A.1}$$

$$f_2(t) = f(t)\exp(2\pi i(s-q)t/t_0) \otimes \sum_m \delta(t - mt_0/\alpha) \tag{A.2}$$

If $f(t)$ is confined into $[-t_0/2\alpha, t_0/2\alpha]$, the product $f_1(t)f_2(t)^*$ can be expressed as follows

$$f_1(t)f_2(t)^* = |f(t)|^2 \exp(2\pi iqt/t_0) \otimes \sum_m \delta(t - mt_0/\alpha) \tag{A.3}$$

which does not depend on the variable s. By using the Fourier expansion of $f_1(t)f_2(t)^*$ and carrying out the multiplication among harmonics we obtain

$$FT[f_1(t)f_2(t)^*](\omega) = 2\pi\alpha^2 \sum_p \delta(\omega - 2\pi p\alpha/t_0) \sum_r a_{r\alpha+s} a^*_{r\alpha+s-p\alpha-q} \tag{A.4}$$

From (A.3) and (A.4), it follows that the sum

$$\sum_r a_{r\alpha+s} a^*_{r\alpha+s-p\alpha-q} \tag{A.5}$$

does not depend on s, so the proof is complete.

Appendix B

Several parameters have been introduced for measuring the overall degree of coherence of the matrix representation of a partially-coherent spatial system. In the context of a study of the effect of partial coherence in the Wigner representation of a paraxial optical system [87, 88], Bastiaans introduced a set of quantities μ_m ($m > 1$) as a measure of partial coherence. The parameters μ_m are based on the N_e eigenvalues λ_k of the matrix representing the impact of partial coherence in the system's performance:

$$\mu_m = \left(\sum_{k=1}^{N_e} \lambda_k^m \right)^{\frac{1}{m-1}} . \tag{B.1}$$

Parameter μ_1 is defined as the limit $\mu_1 = \lim_{m\to\infty} \mu_m$. It can be shown that parameters μ_m are bounded by 0 and 1:$\mu_m = 0$ corresponds to the totally incoherent case whereas $\mu_m = 1$ represents the coherent limit. The value of parameters μ_m is a nondecreasing function of the index m, and therefore μ_1 is the smallest of the set μ_m and thus the most conservative measure of the degree of coherence.

For $m \to \infty$, μ_∞ represents the maximum eigenvalue. The original definition of the effective number of uncorrelated random variables representing the optical signal is precisely its inverse, $1/\mu_\infty$ [89]. The special case μ_1 can be expressed as a function of the entropy:

$$\mu_1 = \exp\left(\sum_{k=1}^{N_e} \lambda_k \ln \lambda_k \right) = \exp(-H). \tag{B.2}$$

Then, parameter μ_1 is the inverse of the effective number of sources as introduced in the text, $N_{eff} = 1/\mu_1$, and represents the largest measure of the number of effective sources when considering the complete series μ_m.

Acknowledgments

Esta tesis representa la culminación del trabajo realizado en los últimos cuatro años. Durante estos años han sido muchas las personas con las que me he cruzado y quienes, bien a nivel académico, bien a nivel personal han contribuido a que este trabajo llegase a buen puerto. A todos ellos quisiera mostrar aquí mi más sincero agradecimiento. Espero no dejarme a nadie en el tintero, pero por si eso ocurriera pido disculpas de antemano.

En primer lugar, y como no podría ser de otra manera, quisiera agradecier a mis directores de tesis Carlos Gómez Reino y Carlos R. Fernández-Pousa, el haberme dado la oportunidad de incorporame a su grupo de investigación, su continua atención y seguimiento, así como las inumerables palabras de apoyo, afecto y animo, que me han brindado a lo largo de estos años. Sin su ayuda la presentación hoy de esta tesis no hubiera sido posible. Quisiera además hacer extensivo mi agradecimiento a todos los miembros del grupo de Óptica GRIN, Mariví, Carmen, Maite, Antonio, Dani y Miguel, por la ayuda prestada y por el distendido y agradable ambiente de trabajo que entre todos generan.

Por supuesto no me olvido de mis compañeros de despacho, tanto de los que ya no están, en especial Jorge y Justo (¡os echamos de menos!) como de los que se han ido incorporando, Paula y la "recién" llegada Bea. Con ellos he compartido mucho más que horas de trabajo entre las mismas cuatro paredes, y si bien, en los últimos meses de redacción de la tesis hubiese pagado por un tranquilo y silencioso despacho para mi solita, nada hubiese sido lo mismo sin ellos.

I also would like to thank to Hans Peter Herzig for giving me the opportunity to join the Applied Optics group of the IMT in Neuchatel. Thanks to Omar Manzardo for supervising my work and for all beers shared, and in general all the members of the Applied Optics group. Voglio ringraziare Piero, per tutto l'aiuto che mi ha dato nel lavoro svolto in laboratorio, ma soprattutto perchè grazie a lui conservo uno splendido ricordo dei mesi trascorsi a Neuchâtel. Un sentito ringraziamento anche

a tutti i suoi amici che fin dal primo giorno mi hanno accolto benissimo.

También quisera recordar aquí a toda la gente estupenda que he tenido la suerte de conocer durante estos años. En especial quisiera nombrar a Lucía, Javi, Xoel, Sara e Iria quienes, a nivel personal, han sido para mi un gran apoyo, y con quienes he compartido tan buenos momentos.

Por último y no por ello menos importante tengo que agradecer a mis padres todo el cariño, la confianza, el apoyo me han mostrado simpre, especialmente en mis momentos más bajos. !Gracias!

Publications

Papers

- L. Chantada, C.R. Fernández-Pousa, M.T. Flores-Arias, C. Bao, M.V. Pérez and C. Gómez-Reino, "Stochastic description of timing jitter in temporal Talbot effect: variance and spectral power", *Óptica pura y aplicada*, **37**, 11-16 (2004).

- C.R. Fernández-Pousa, F. Mateos, L. Chantada, M.T. Flores-Arias, C. Bao, M. V. Pérez and C. Gómez-Reino, "Broadband noise filtering in random sequences of coherent pulses using Temporal Talbot effect", *J. Opt. Soc. Am. B* **21**, 914-922 (2004).
  This article has been selected for the May 2004 issue of Virtual Journal of Ultrafast Science.(http://www.vjultrafast.org.)

- C.R. Fernández-Pousa, F. Mateos, L. Chantada, M.T. Flores-Arias, C. Bao, M.V. Pérez and Carlos Gómez-Reino, "Timing jitter smoothing by Talbot effect. I Variance", *J. Opt. Soc. Am. B* **21**, 1170-1177 (2004).
  This article has been selected for the June 2004 issue of Virtual Journal of Ultrafast Science (http://www.vjultrafast.org.)

- C.R. Fernández-Pousa, F. Mateos, L. Chantada, M.T. Flores-Arias, C. Bao, M.V. Pérez and C. Gómez-Reino, "Timing jitter smoothing by Talbot effect. II Intensity Spectrum", *J. Opt. Soc. Am. B* **22**, 753-763 (2005).
  This article has been selected for the May 2005 issue of Virtual Journal of Ultrafast Science (http://www.vjultrafast.org.).

- L. Chantada, C.R. Fernández-Pousa and C. Gómez-Reino, "Spectral analysis of temporal self-imaging in fiber dispersive lines", *J.*

Lightwave Technol. **24**, 2015-2025 (2006).

- L. Chantada, C.R. Fernández-Pousa and C. Gómez-Reino, "Theory of the partially coherent temporal Talbot effect", *Opt. Commun.* in press (2006).
- L. Chantada, C.R. Fernández-Pousa and C. Gómez-Reino, "Matrix theory and entropy of the partially coherent temporal Talbot effect", submitted to *J. Mod. Opt.* in press (2006)

Congress Contributions

- L. Chantada, C.R. Fernández-Pousa, M.T. Flores-Arias, C. Bao, M.V. Pérez , "Descripción estocástica del efecto Talbot temporal: Varianza y Potencia espectral", 7^{th} *National meeting on Optics*, Santander, Spain, September 8-11 (2003), page 64.
- L. Chantada, C.R. Fernández-Pousa, M.T. Flores-Arias, C. Bao and C. Gómez-Reino, "Broadband noise filtering in random sequences of coherent pulses using the temporal Talbot effect", *MOC'04*, Jena, Germany, September 1-3, (2004) page 54.
- L. Chantada, C.R. Fernández-Pousa and C. Gómez-Reino, "Exact RF intensity Spectrum of OOK trains of coherent pulses after linear propagation under first and second GVD" *Optical architectures for RF signal processing and signal mixing*, Panticosa, Spain, September 27-29, (2004).
- L. Chantada, C.R. Fernández-Pousa and C. Gómez-Reino, " Intensity spectral analysis of the temporal Talbot effect in a second-order dispersive line", 4^{th} *Spanish meeting on optoelectronics* 13-15 july (2005), Elche (Spain), TFO4-195-200.
- L. Chantada, C.R. Fernández-Pousa and C. Gómez-Reino, "Intensity spectrum analysis of a jittery train after temporal Talbot dispersive line with second order dispersion" *SPIE international congress on Optics and Optoelectronics*, Warsaw, Poland, 28 August-2 September, (2005). Proc SPIE **5952**, 1-9, 2005
- L. Chantada, C.R. Fernández-Pousa and C. Gómez-Reino, "Influencia de la cohernecia parcial en el efecto Talbot temporal" 8^{th} *National meeting on Optics*, Alicante, Spain, 18-22 september, (2006)

Bibliography

[1] A. Papoulis, "Pulse compression, fiber communications and diffraction: a unified approach", *J. Opt. Soc. Am. A* **11**, 3-13 (1994).

[2] B.H. Kolner "Space-time duality and the theory of temporal imaging", *IEEE J. Quantum Electron.* **30**, 1951-1963 (1994).

[3] B.E.A. Saleh and M.C. Teich, *Fundamentals of Photonics*, John Wiley & Sons, New York, 1991.

[4] E.B. Treacy "Optical pulse compressing with diffrection gratings", *IEEE Journal of Quantum Electron.*, **QE-5**, 454-458 (1969).

[5] G. P. Agrawal, *Nonlinear Fiber Optics*, 3rd ed. (Academic, Boston, 2001).

[6] B.H. Kolner and M. Nazarathy "Temporal imaging with a time lens", *Opt. Lett.*, **14**, 630-632 (1989).

[7] C.V. Bennett and B.H. Kolner, "Upconversion time microscope demonstrating 103× magnification of femtosecond waveforms", *Opt. Lett.* **24**, 783-785 (1999).

[8] A.W. Lohmann and D. Mendiovic "Temporal filtering with time lenses", *Appl. Opt.*, **31**, 6212-6219 (1992).

[9] T. Jannson, "Real-time Fourier transformation in dispersive optical fibers", *Opt. Lett.* **8**, 232-234 (1983).

[10] J. Azaña, L.R. Chen, M.A. Muriel, and P.W.E. Smith, "Experimental demonstration of real-time Fourier transformation using linearly chirped fibre Bragg gratings", *Electron. Lett.* **35** 2223-2224 (1999).

[11] M. A. Muriel, J. Azaña, and A. Carballar, "Real-time Fourier transformer based on fiber gratings", *Opt. Lett.*, **24**, 1-3 (1999).

[12] C. Dorrer, "Temporal van Cittert-Zernike theorem and its application to the measurement of chromatic dispersion" *J. Opt. Soc. Am. B*, **21** 1417-1423 (2004).

[13] E. Collett and E. Wolf, "Is complete spatial coherence necessary for the generation of highly directional light beams?" *Opt. Lett.*, **2**, 27-29 (1978).

[14] B.E.A. Saleh and M.I. Irshid, "Collett-Wolf equivalence theorem and propagation of a pulse in a single-mode optical fiber" *Opt. Lett.*, **7**, 342-343, (1982).

[15] F.J. Marinho and L.M. Bernardo "Graded-index time-lens implementation", *Opt. Lett.*, **31**, 1723-1725 (2006)

[16] L. A. Jiang, M. E. Grein, H. A. Haus, E. P. Ippen, and H. Yokoyama, "Timing jitter eater for optical pulse trains", *Opt. Lett.* **28**, 78-80 (2003).

[17] Y.C. Tong, L.Y. Chan, and H.K. Tsang, "Fibre dispersion or pulse spectrum measurement using a sampling oscilloscope" *Electron. Lett.*, **33**, 983-985 (1997).

[18] M.T. Kauffman, W.C. Banyai, A.A. Godil, and D.M. Bloom, "Time-to-frequency converter for measuring picosecond optical pulses", *Appl. Phys. Lett.*, **64** 270-272 (1994).

[19] T. Jannson and J. Jannson, "Temporal self-imaging in single-mode fibers" *J. Opt. Soc. Am.* **71**, 1373-1376 (1981).

[20] J. Azaña and M. A. Muriel, "Temporal self-imaging effects: theory and application for multiplying pulse repetition rates", *IEEE J. Sel. Top. Quantum Electron.* **7**, 728-744 (2001).

[21] K. Patorski, "The self-imaging phenomenon and its applications", in *Progress in Optics, Vol. XXVII*, E. Wolf, ed. (Elsevier, Amsterdam, 1989), pp. 1-108.

[22] M. V. Berry and S. Klein, "Integer, fractional, and fractal Talbot effects", *J. Mod. Opt.* **43**, 2139-2164 (1996).

[23] P.A. Andrekson, "Linear propagation of optical picosecond pulse trains over oceanic distances", *Opt. Lett.* **18**, 1621-1623 (1993).

[24] S. Arahira, S. Kutsuzawa, Y. Matsui, D. Kunimatsu, and Y. Ogawa, "Generation of synchronized subterahertz optical pulse trains by repetition-frequency multiplication of subharmonic synchronous mode-locked semiconductor laser diode using fiber dispersion", *IEEE Photon. Technol. Lett.* **10**, 209-211 (1998).

[25] S. Arahira, S. Kutsuzawa, Y. Matsui, D. Kunimatsu, and Y. Ogawa, "Repetition-frequency multiplication of mode-locked pulses using fiber dispersion", *J. Lightwave Technol.* **16**, 405-410 (1998).

[26] I. Shake, H. Takara, S. Kawanishi, and M. Saruwatari, "High-repetition-rate optical pulse generation by using chirped optical pulses", *Electron. Lett.* **34**, 792-793 (1998).

[27] J. Azaña and M. A. Muriel, "Technique for multiplying the repetition rates of periodic trains of pulses by means of a temporal self-imaging effect in chirped fiber gratings", *Opt. Lett.* **24**, 1672-1674 (1999).

[28] S. Longhi, M. Marano, P. Laporta, O. Svelto, M. Belmonte, B. Agogliati, L. Arcangeli, V. Prunei, M. N. Zervas, and M. Ibsen, "40-GHz pulse-train generation at 1.5 μm with a chirped fiber grating as a frequency multiplier", *Opt. Lett.* **25**, 1481-1483 (2000).

[29] V. P. Minkovich, A. N. Starodumov, V. I. Borisov, V. I. Ledebev, and S. N. Perepechko, "Temporal interference of coherent laser pulses in optical fibers", *Opt. Commun.* **192**, 231-235 (2001).

[30] C. B. Huang and Y. Lai, "Loss-less pulse intensity repetition-rate multiplication using optical all-pass filtering", *IEEE Photon. Technol. Lett.*, **12**, 167-169 (2000).

[31] J. Azaña, P. Kockaert, R. Slavik, L. R. Chen, and S. LaRochelle, "Generation of a 100-GHz optical pulses train by pulse repetition-rate multiplication using superimposed fiber Bragg gratings", *IEEE Photon. Technol. Lett.* **15**, 413-415 (2003).

[32] J. Azaña, N.K. Berger, B. Levit, V. Smulakovsky, and B. Fischer, "Frequency shifting of microwave signals by use of a general temporal self-imaging (Talbot) effect in optical fibers", *Opt. Lett.* **29**, 2849-2851 (2005).

[33] J. Azaña, C. Wang and L. R. Chen, "Spectral self-imaging phenomena in sampled Bragg gratings", *J. Opt. Soc. Am. B*, **22**, 1829-1841 (2005)

[34] J. Azaña and M.A. Muriel, "Technique of simultaneously multiplying the repetition rate of multiwavelength optical pulse train", *IEEE Photon. Technol. Lett.* **13**, 1358-1360 (2001).

[35] J. Azaña and M.A. Muriel, "Synchronized multiplication of repetition rates in multiwavelength optical pulse trains", *Optics and Photonics News*, **12** 47-47 (2001).

[36] A. M. Weiner and D. E. Leaird, "Generation of terahertz-rate trains of femtosecond pulses by phase-only filtering", *Opt. Lett.*, **15**, 51-53 (1990).

[37] A. M Weiner, S. Oudin, D. E. Leaird, and D. H. Reitze, "Shaping of femtosecond pulses using phase-only filters designed by simulated annealing", *J. Opt. Soc. Am. A*, **10**, 1112-1120 (1993).

[38] K. Tai, A. Tomita, J. L. Jewell, and A. Hasegawa, "Generation of sub-picosecond soliton-like optical pulses at 0.3 THz repetition-rate by induced modulation instability", *Appl. Phys. Lett.*, **49**, 236-238 (1986).

[39] P. Petropoulos, M. Ibsen, M. N. Zervas, and D. J. Richardson, "Generation of 40-GHz pulse stream by pulse multiplication with a sampled fiber Bragg grating", *Opt. Lett.*, **25**, 521-523 (2000).

[40] G. Meloni, G. Berrettini, M. Scaffardi, A. Bogoni, L. Potì and M. Guglielmucci, "250-times repetition frequency multiplication for 2.5 THz clock signal generation", *Electron. Lett.*, **41**, 1294-1295 (2005).

[41] B. Fischer, B. Vodonos, S. Atkins, and A. Bekker, "Dispersion-mode pulsed laser", *Opt. Lett.* **25**, 728-730 (2000).

[42] S. Atkins, B. Vodonos, A. Bekker, and B. Fischer, "Fractional dispersion modes in a pulsed fiber laser", *Opt. Commun.* **222**, 393-397 (2003).

[43] N. K. Berger, B. Vodonos, S. Atkins, V. Smulakovsky, A. Bekker, and B. Fischer, "Compression of periodic light pulses using all-optical repetition rate multiplication", *Opt. Commun.* **217**, 343-349 (2003).

[44] N.K. Berger, B. Levit, A. Bekker and B. Fischer, "Compression of periodic optical pulses using temporal fractional Talbot effect", *IEEE Photon. Technol. Lett.*, **16**, 1855-1857 (2004)

[45] M. Marano, S. Longhi, P. Laporta, M. Belmonte, and B. Agogliati, "All-optical square-pulse generation and multiplication at 1.5 γm by use a novel class of fiber Bragg gratings", *Opt. Lett.* **26**, 1615-1617 (2001).

[46] J.H. Lee, Y.M. Chang, Y-G. Han, S.H. Kim, and S.B. Lee, "2$\sim$5 times tunable repetition-rate multiplication of a 10 GHz pulse source using a linearly tunable, chirped fiber Bragg grating", *Opt. Express* **12**, 3900-3905 (2004).

[47] J.A. Bogler, P. Hu, J.T. Mok, J.L. Blows, and B.J. Eggleton, "Talbot self-imaging and cross-phase modulation for generation of tunable high repetition rate pulse trains", *Opt. Commun.* **249**, 431-439 (2005).

[48] C.J.S. de Matos and J.R. Taylor, "Tunable repetition-rate multiplication of a 10 GHz pulse train using linear and nonlinear fiber propagation", *Appl. Phys. Lett.* **83**, 5356-5358 (2003).

[49] D. A. Chestnut, C. J. S. de Matos, and J. R. Taylor, "4$\times$ repetition-rate multiplication and Raman compression of pulses in the same optical fiber" *Opt. Lett.* **27**, 1262-1264 (2002).

[50] M. T. Flores-Arias, C. Bao, M. V. Pérez, and C. R. Fernández-Pousa, "Fractional Talbot effect in a Selfoc gradient-index lens", *Opt. Lett.* **27**, 2064-2066 (2002).

[51] C. Gómez-Reino, M. V. Pérez, and C. Bao, *Gradient-Index Optics: Fundamentals and Applications* (Springer-Verlag, Berlin, 2002), Chap. 7.

[52] R. Ulrich, "Image formation by phase coincidences in optical waveguides", *Opt. Commun.* **13**, 259-264 (1975).

[53] F. Mitschke and U. Morgner "Temporal Talbot effect", *Opt. Photon. News*, **9**, 45-47 (1998).

[54] J. Azaña and M. A. Muriel, "Temporal Talbot effect in fiber gratings and its applications", *Appl. Opt.* **38**, 6700-6704 (1999).

[55] J. Azaña and M. A. Muriel, "Technique for multiplying the repetition rates of periodic trains of pulses by means of a temporal self-imaging effect in chirped fiber gratings", *Opt. Lett.*, **24**, 1672-1674 (1999).

[56] S. Atkins and B. Fischer, "All-optical pulse rate multiplication using fractional Talbot effect and field-to-intensity conversion with cross-gain modulation", *IEEE Photonics Technol. Lett.* **15**, 132-134 (2003).

[57] R. Kashiap, *Fiber Bragg Gratings*, London, U.K.: Academic, 1999.

[58] F. Ouellette, "Dispersion cancellation using lineraly chirped Bragg grating filters in optical waveguides", *Opt. Lett.*, **12**, 847-849 (1987).

[59] F. Ouellette, J.F. Cliche and S. Gagnon "All-fiber devices for chromatic dispersion compensation based on chirped distributed resonant coupling", *J. Lightwave Technol.*, **12**, 1728-1738 (1994).

[60] J. T. Mok and B. J. Eggleton, "Impact of group delay ripple on repetition-rate multiplication through Talbot self-imaging effect", *Opt. Commun.* **232**, 167-178 (2004).

[61] M.J. Erro, M.A.G. Laso, D. Benito, M.J. Garde, M.A. Muriel, "Third-order dispersion in linearly chirped Bragg gratngs and its compensation", *Fiber and Integrated Optics* **19**, 367-382 (2000)

[62] K. Jürgensen, "Transmission of gaussian pulses through monomode dielectric optical waveguides", *Appl. Opt.* **16**, 22-23 (1977).

[63] K. Jürgensen, "Gaussian pulse transmission through monomode fibers, accounting for source linewidth", *Appl. Opt.* **17**, 2412-2415 (1978).

[64] B.E.A. Saleh and M.I. Irshid, "Transmission of pulse sequences through monomode fibers", *Appl. Opt.* **21**, 4219-4222 (1982).

[65] B.E.A. Saleh and M.I. Irshid, "Coherence and intersymbol interference in digital fiber optics communication systems", *IEEE J. Quantum Electron.* **QE-18**, 944-951 (1982).

[66] M.A. Muriel and J. Capmany, "Optical pulse sequence transmission through monomode fibres under second and third-order dispersion", *Electron. Lett.* **24**, 1252-1253 (1988).

[67] J. Capmany and M.A. Muriel, "Optical pulse sequence transmission through single-mode fibers: interference signal analysis", *J. Lightwave Technol.* **9**, 27-36 (1991).

[68] C. Dorrer and D.N. Maywar, "RF spectrum analysis of optical signals using nonlinear optics", *J. Lightwave Technol.* **22**, 266-274 (2004).

[69] J. Fatome, S. Pitois, and G. Millot, "Influence of third-order dispersion on the temporal Talbot effect", *Opt. Commun.* **234**, 29-34 (2004).

[70] J. Azaña, "Pulse repetition rate multiplication using phase-only filtering", *Electron. Lett.* **40**, 449-451 (2004).

[71] H. Schmuck, "Comparison of optical millimeter-wave systems with regard to chromatic dispersion", *Electron. Lett.* **31**, 1848-1849 (1995).

[72] G. H. Hardy and E.M. Wright, *An introduction to the theory of numbers*, 5th ed., Clarendon, Oxford, 1995, chap 2, pp 21-26.

[73] A. Kalestynski and B. Smolinska, "Self-restoration of the autoidolon of defective periodic objects", *Opt. Acta* **25**, 125-134 (1978).

[74] J. Azaña, "Temporal self-imaging effects for periodic optical pulse sequences of finite duration", *J. Opt. Soc. Am. B* **20**, 83-90 (2003).

[75] D. von der Linde, "Characterization of the noise in continuously operating mode-locked lasers", *Appl. Phys. B: Photophys. Laser Chem.* **39**, 201-217 (1986).

[76] R. P. Scott, C. Langrock, and B. H. Kolner, "High dynamic range laser amplitude and phase noise measurement techniques", *IEEE J. Sel. Top. Quantum Electron.* **7**, 641-655 (2001).

[77] T. Yilmaz, C. M. Depriest, A. Braun, J. H. Abeles, and P. J. Delfyett, "Noise in fundamental and harmonic mode-locked semiconductor lasers: experiments and simulations", *IEEE J. Quantum Electron.* **39**, 838-849 (2003).

[78] F. Rana, H. L. T. Lee, R. J. Ram, M. E. Grein, L. A. Jiang, E. P. Ippen, and H. A. Haus, "Characterization of the noise and correlations in harmonically mode-locked lasers", *J. Opt. Soc. Am. B* **19**, 2609-2621 (2002).

[79] A. Papoulis, *Probability, Random Variables and Stochastic Processes*, 2nd ed. (McGraw-Hill, New York, 1984)

[80] J. G. Proakis and D. G. Manolakis, *Digital Signal Processing*, 3rd ed. (Prentice-Hall, Upper Saddle River, N.J., 1996).

[81] T. Yilmaz, C. M. DePriest, P. J. Defyett, S. Etemad, A. Braun, and J. H. Abeles, "Supermode suppression to below 2130 dBc/Hz in a 10

GHz harmonically mode-locked external sigma cavity semiconductor laser", *Opt. Express* **11**, 1090-1095 (2003).

[82] A. S. Hou, R. S. Tucker, and G. Eisentein, "Pulse compression of an actively mode-locked diode laser using linear dispersion in fiber", *IEEE Photon. Technol. Lett.* **2**, 322-324 1990).

[83] W.K. Marshall and A. Yariv, "Spectrum of the intensity of modulated noisy light after propagation in disspersive fiber", *IEEE Photon. Technol. Lett.*, **12**, 302-304 (2000).

[84] A.M. Vengsarkar and I.M. Besieris,"Regenerative periodic pulse trains in linear dispersive, single-mode optical fibers: effect of finite source linewidths" *IEEE Photon. Technol. Lett.*, **3**, 33 (1991).

[85] H. Gamo, *Matix treatment of partial coherence*, in Progress in Optics, E. Wolf, ed.(North-Holland, Amsterdam, 1963), vol. 3, p.187.

[86] E.L. O'Neill, *Introduction to stitstical optics* (Addison-Wesley, Reading, Mass, 1963), chap 8.

[87] M.J. Bastiaans, *Application of the Wigner distribution function to partially coherent light*, *J. Opt. Soc. Am. A***3**, 1227-1238 (1986).

[88] M.J. Bastiaans, *Application of the Wigner distribution function in optics: Theory and Applications in Signal Processing*, W. Mecklenbräuker, and F. Hlawatsch, eds. (Elsevier, Amsterdam, 1997), p. 375.

[89] A. Starikov, "Effective number of degrees of freedom of partially coherent sources", *J. Opt. Soc. Am.* **72**, 1538-1544 (1982).

[90] J. Capmany, D. Pastor, S. Sales, and M.A. Muriel, "Pulse distortion in optical fibers and waveguides with arbitrary chromatic dispersion", *J. Opt. Soc. Am. B* **20**, 2523-2533 (2003).

[91] M. Born and W. Wolf, *Principles of Optics*, 6*th* ed. (Pergamon, Oxford, 1980).

[92] C.H. Henry, "Theory of the linewidth of semiconductor lasers", *IEEE J. Quantum Electron.*, **18**, 259-264 (1982).

[93] P.T Ho, "Phase and amplitude fluctuations in a mode-locked laser", *IEEE J. Quantum Electron.*, **21**, 1806-1813 (1985).

[94] H. Lajunen, J. Tervo, J. Turunen, P. Vahimaa, J. Tervo and F. Wyrowski, "Spectral coherence poperties of temporally modulated stationary light sources", *Opt. Express*, **11**, 1894-1899 (2003).

[95] Q. Lin, L. Wangn and S. Zhu, "Partially coherent light pulse and its propagation", *Opt. Commun.*, **219**, 65-70 (2003).

[96] H. Lajunen, J. Turunen, P. Vahimaa, J. Tervo and F. Wyrowski, "Spectrally partially coherent pulse trains in dispersive media", *Opt. Commun.*, **255**, 12-22 (2005).

[97] J. Lancis, V. Torres-Company, E. Silvestre and P. Andrés, "Space-time analogy for partially coherent plane-wave type pulses", *Opt. Lett.*, **30** 2973-2975 (2005).

[98] D. Marcuse, "Pulse distortion in single-mode fibers" *Appl. Opt.*, **19**, 1653-1660 (1980).

[99] D. Marcuse, "Pulse distortion in single-mode fibers-II", *Appl. Opt.*, **20**, 2969-2974 (1981).

[100] G.H. Smith, H. Graham, D. Novak, Z. Ahmed, "Overcoming chromatic-dispersion effects in fiber-wireless systems incorporating external modulators" *IEEE Trans, Microwave Theory Tech.* **45** 1410-1415 (1997).

[101] Ch.-Ch. Wang, *J. Lightwave Technol.* **4** 572-579 (1983).

[102] J. Capmany, B. Ortega, D. Pastor and S. Sales, "Discrete-time optical processing of microwave signals" *J. Lightwave Technol.* **23** 702- (2005).

[103] G. Strang, *Linear Algebra and Its Applications*, 3*rd* (Harcourt Brace Jovanovitch, San Diego, Calif, 1988).

[104] R.M Gray, "Toeplitz and circulant matrices: A review", *Foundations and tends in communications and information theory*, **2**, 155 (2006).